Raman Scattering and First-Principles Analysis of Ge Nanostructures, *h*-BN and KIO_3

LIU LEI

NATIONAL UNIVERSITY OF SINGAPORE

2003

Raman Scattering and First-Principles Analysis of Ge Nanostructures, *h*-BN and KIO_3

LIU LEI
(M.Sc., Jilin Univ.)

A THESIS SUBMITTED
FOR THE DEGREE OF DOCTOR OF PHILOSOPHY
DEPARTMENT OF PHYSICS
NATIONAL UNIVERSITY OF SINGAPORE
2003

ACKNOWLEDGEMENT

I am greatly indebted to my supervisor Assoc. Prof. Shen Ze Xiang, whose invaluable guidance, stimulating suggestions and encouragement helped me in all the time during this PhD project.

Assoc. Prof. Feng Yuang Ping also has my complete gratitude, for his priceless helps, suggestions and collaboration during the work on the first-principles calculations in this project.

Dr. Teo Kie Leong, Department of Electrical and Computer Engineering, also has my full gratitude, for his precious discussions, supports and collaboration during the work on Germanium nanocrystals in this project.

I would also like to thank Dr. Yao Bin, from Jilin university in China, who has the research interests in the *t*(turbostratic)-BN and *a*(amorphous)-BN. As I read the references related to *t*-BN and *a*-BN, I found that the basic electronic and structural properties of *h*-BN could be influenced by the stacking behavior of hexagonal basal layers and carried out the theoretical investigations on *h*-BN consequently.

My gratitude is also conveyed to all my colleagues in Laser Spectroscopy Laboratory of National University of Singapore, in particular to Dr. Chen Mingsong, Dr. Qin Li and Dr. Sun Wanxin for their help during my Ph.D. study.

Finally but most importantly, I give my greatest gratitude to my family for their unfailing support and love.

TABLE OF CONTENTS

SUMMARY

This thesis presents high-pressure Raman scattering investigations and elastic analysis of the Ge nanostructures, the first-principles calculations on the structural and electronic properties of *h*-BN, and the studies on the phase transition mechanism in KIO_3 single crystals with both Raman scattering technique and the first-principles calculation.

Firstly, the Ge/SiO_2 nanosystem was investigated by Raman scattering under hydrostatic pressure. A large pressure coefficient for the Ge-Ge mode in Ge nanocrystals (nc's) as compared to its corresponding bulk value was observed and the observed effect is explained in terms of a simple elastic model, which describes the significant contribution of the interface stress when the nanosystem is subjected to applied pressure. In the $Ge/SiO_2/Si$ nanosystem, we found that the delaminating of SiO_2 film from the Si substrate occurs at ~23 kbar. The observed effect can be understood by the nonhomogeneous distribution of the elastic field in the $Ge/SiO_2/Si$ nanosystem. The previous unexplained high pressure PL results on the $Si/SiO_2/Si$ nanosystem can also be explained by the nonuniform distribution of the elastic field.

Secondly, *h*-BN structures due to stacking sequence have been investigated thoroughly using the DFT-LDA method. Five possible *h*-BN structures, i.e. structures A, B, and C with symmetry $P6_3/mmc$ in one group (I) and structures D with P3m1 and E with $P\bar{6}m2$ in another (group II) were studied. Structures A and D are found stable, structure B metastable, all with "good" stacking of BN layers. Structures C and E are unstable. These structures with "bad" stacking of BN layers have longer lattice constant *c* compared to structures with "good" stacking sequences. Real *h*-BN crystals with mixed stacking and intrinsic stacking faults can be expected which are the reasons for the large variations of electronic properties of *h*-BN. Stacking sequence disorder is

also the origin for the observed larger interlayer spacings in PBN and *t*-BN. Moreover, the electronic properties of *h*-BN were found to be strongly dependent on the stacking of the hexagonal BN layers. Based on the calculated band structures for various phases, we presented a complete explanation on the inconsistency in experimental electronic and optical properties of *h*-BN. The diverse band gap values of *h*-BN observed experimentally now can be understood based on the variation of its band structure due to stacking. The discrepancy in the band gap characteristics of *h*-BN, of being direct or indirect, can be attributed to the existence of the metastable structure B. Furthermore, structures with disordered stacking sequence such as PBN and *t*-BN were predicted to have much smaller band gap than that of a normal *h*-BN.

Finally, we present a detailed polarized Raman study on KIO_3 at variable temperature and first-principles analysis (DFPT-LDA) of the dynamical properties of KIO_3 single crystals in the rhombohedral phase I. The existence of the broad central peak in phase I and the soft modes S_1 and S_2 with great damping near the phase transitions I-II and II-III of KIO_3 is observed by Raman technique. Furthermore, a transient incommensurate (INC) phase is suggested to exist in phase I of KIO_3 near the phase transition based on the calculated phonon dispersion curves. With the appearance of INC phase in phase I, the improper ferroelectric characteristics of phase transition I-II of KIO_3 observed by the dielectric constant investigations can be understood easily.

Publications

1 L. Liu, Z. X. Shen, Y. P. Feng, "Phase Transition mechanisms in KIO_3 Single Crystals", *JOURNAL OF CHEMICAL PHYSICS* (submitted).

2 L. Liu, K. L. Teo, Z. X. Shen, J. S. Sun, E. H. Ong, A. V. Kolobov and Y. Maeda, "Raman scattering investigation of Ge/SiO_2/Si nano-system under hydrostatic pressure", *PHYSICAL REVIEW B*, 69, 125333, MAR 2004.

3 L. Liu, Y. P. Feng, Z. X. Shen, "Structural and electronic properties of *h*-BN", *PHYSICAL REVIEW B*, 68, 104102, SEP 2003.

4 L. Liu, Z. X. Shen, K. L. Teo, A. V. Kolobov and Y. Maeda, "Raman scattering of Germanium nanocrystals embedded in glass matrix under hydrostatic pressure", *JOURNAL OF APPLIED PHYSICS*, 93 (11): 9232-9234, JUN 2003.

5 B. Yao, L. Liu, W. H. Su, Z. X. Shen, L. Liu, W.X. Sun, and J. Ding, "Effects of Degree of Three Dimensional Order and Fe Impurities on Photoluminescence of Boron Nitride", *JOURNAL OF APPLIED PHYSICS*, 96 : (in press), 15 Aug 2004.

6 Y. P. Zeng, Y. F. Lu, Z. X. Shen, W. X. Sun, T. Yu, L. Liu, J. N. Zeng, B. J. Cho, C. H. Poon, "Raman spectroscopy investigation on excimer laser annealing and thickness determination of nanoscale amorphous silicon", *NANOTECHNOLOGY*, 15 (5): 658-662, MAY 2004.

7 B. Yao, Z. X. Shen, L.Liu, W. H. Su, "Strong deep-blue photoluminescence of mesographite boron nitride", *JOURNAL OF PHYSICS: CONDENSED MATTER*, 16: 2181-2186, MAR 2004.

8 X. Zhang, W. Zhang, L. Liu, Z. X. Shen, "Surface-enhanced Raman of Z-vibration mode in single-walled and multi-walled carbon nanotube", *CHEMICAL PHYSICS LETTERS*, 372 (3-4): 497-502, APR 2003.

9 L. H. Wong, C. C. Wong J. P. Liu, L. Chan, L. Liu, Z.X.Shen, "Determination of Raman strain shift coefficient in strained Silicon epilayers", *APPLIED PHYSICS LETTERS* (submitted).

10 F. Chen, L. Liu, Z. X. Shen, G. Q. Xu, T. S. A. Hor, "Formation of hydrogenated amorphous carbon films from polymer pyrolysis", *APPLIED PHYSICS A-MATERIALS SCIENCE & PROCESSING*, 74 (2): 317-319, FEB 2002.

11 S. Tang, Z. Zhong, Z. Xiong, L. Sun, L. Liu, J. Lin, Z. X. Shen, K. L. Tan, "Controlled growth of single-walled carbon nanotubes by catalytic decomposition of CH4 over Mo/Co/MgO catalysts", *CHEMICAL PHYSICS LETTERS*, 350 (1-2): 19-26, DEC 2001.

12 G. Y. Yu, Z. X. Shen, L. Liu, W. X. Sun, "Raman scattering study of a GaAsN epitaxial layer", *MATERIALS SCIENCE IN SEMICONDUCTOR PROCESSING*, 4 (6): 581-584, DEC 2001.

13 L. Liu, K. L. Teo, Z. X. Shen, A. V. Kolobov, Y. Maeda, "Raman scattering study in germanium nanocrystals under hydrostatic pressure", *Symposium H - Compound Semiconductors in Electronic & Optoelectronic Applications, ICMAT 2003 International Conference on Materials for Advanced Technologies*.

14 K. L. Teo, L. Liu, Z. X. Shen, O. G. Schmidt, "Raman scattering studies of Ge/Si islands under hydrostatic pressure", *Symposium H - Compound*

Semiconductors in Electronic & Optoelectronic Applications, ICMAT 2003 International Conference on Materials for Advanced Technologies.

15 Z. X. Shen, C. Y. Chng, L. Liu, K. L. Teo, A. H. Fu, A. P. Alivisatos, "Phase stability and optical properties of CdSe nanorods under hydrostatic pressure", *Symposium N2 - Science and Technology of Nanomaterials, ICMAT 2003 International Conference on Materials for Advanced Technologies*, *ICMAT 2003 International Conference on Materials for Advanced Technologies*.

16 L. H. Wong, C. C. Wong, K. K. Ong, J. P. Liu, L. Chan, R. Rao, L. Liu, Z. X. Shen, K. L. Pey, "Thermal Stability of Strained $Si/Si_{1-x}Ge_x$ Heterostructures for Advanced Microelectronics Devices", *Symposium L – Advances in Materials for Si Microelectronics – from Processing to Packaging, ICMAT 2003 International Conference on Materials for Advanced Technologies*.

17 B. Yao, L. Liu, Z. X. Shen, "Effect of three dimensional order on photoluminescence of boron nitrides", *International Conference of Raman Spectroscopy 2002, Aug. 25-30, Budapest, Hungary*.

18 L. Liu, Z. X. Shen, "Raman Research of KIO_3 Single Crystal at Different Temperature and Pressure", *Symposium N – Materials for Optoelectronics & High Frequency Electronics Applications, ICMAT 2001 International Conference on Materials for Advanced Technologies*.

19 G. Y. Yu, Z. X. Shen, L. Liu, W. X. Sun, "Raman Study of the GaAsN Epitaxy Layer", *Symposium N – Materials for Optoelectronics & High Frequency Electronics Applications, ICMAT 2001 International Conference on Materials for Advanced Technologies*.

20 L. Liu, Z. X. Shen, X. B. Wang, "High Pressure Raman Spectral Study of KIO_3", in *ICORS 2000 - Proceedings of the Seventeenth International Conference on Raman Spectroscopy*, edited by S. L. Zhang and B. F. Zhu, 2000, p148.

21 C. W. Tiong, M. S. Chen, L. Liu, L. Li, Z. X. Shen, "Polarized-Raman Study of Phase Transitions in Potassium Lithium Niobate Single Crystals", *ICORS 2000 - Proceedings of the Seventeenth International Conference on Raman Spectroscopy*, edited by S. L. Zhang and B. F. Zhu, p150.

Chapter 1

Introduction

The term Raman scattering is historically associated with the light scattering by optical phonons in solids and liquids. Since its discovery, especially after the invention of lasers, Raman scattering has gradually become one of the most versatile spectroscopic tools to study the low-lying excitations of condensed matter systems.[1,2] In this thesis, Chapter 2 reviews briefly the historical development of the Raman scattering studies, and introduces the basic theory of Raman effect with special emphasis on the Raman scattering by phonons.

Due to its contactless and non-destructive nature, Raman scattering is very attractive as a characterization technique of semiconductors. The typical applications of Raman spectroscopy include the determination of crystalline orientations, the measurement of temperature and stress, the characterization of doping levels, and the study of alloy semiconductors. In particular, Raman scattering is very useful in the study of the electronic and vibrational properties of semiconductor nanostructures. Raman scattering has played leading roles in understanding the vibrational properties of quantum wells and the collective excitations of electron gases, and become one of the most powerful methods to access the stress/strain information on the embedded nanocrystals. Since the stress/train effects play an important role in tailoring optical and electronic properties of the semiconductor nanostructures, the study on the stress/strain effects in semiconductor nanostructures may explore further their possible

applications, such as in integrated optoelectronic devices. Chapter 3 describes the high pressure Raman scattering investigations on the stress/strain effects of the Ge/SiO_2 and $Ge/SiO_2/Si(100)$ nanostructures.

While Raman spectroscopy is used as an important analytical technique for structure identification of solids experimentally, total-energy calculations are used generally as a predictive tool for structural properties of solids theoretically. The ground-state total energy and its derivatives are among the most important properties that can be obtained from first-principles quantum mechanical calculations when applied to solids. If the total energy of a system can be calculated, many physical properties related to the total energy, such as the equilibrium lattice constant, can be determined. So far, total-energy techniques have been successfully used to predict with accurate equilibrium lattice constants, bulk moduli, phonons, piezoelectric constants, and phase-transition pressures and temperatures.[4] In this thesis, the simplifications and approximations related to the first-principles total-energy pseudopotential calculations are briefly introduced in Chapter 4.

An example of utilizing the total-energy and electronic-structure calculations is given in Chapter 5 to investigate the electronic and structural properties of *h*-BN. *h*-BN is the most common phase and the best studied polymorph of BN, among the four different polymorphic modifications of boron nitride (BN) *i.e.* cubic *c*-BN, wurzite *w*-BN, hexagonal *h*-BN, and rhombohedral *r*-BN. However there has been no agreement on the basic electronic properties of *h*-BN to date. Widely dispersed band gap energy values ranging from 3.6 *eV* to 7.1 *eV* for *h*-BN can be found in different experimental results, in which both direct and indirect band gaps have been suggested. Moreover, few of theoretical studies can provide direct understanding of the dispersed experimental band gap values and the conflicting description of the band gap nature of

h-BN. Chapter 5 aims to provide a clear understanding of the structural and electronic properties of *h*-BN. A systematic investigation on structural and electronic properties of *h*-BN related to stacking of the basal BN layers is reported in this chapter, using the density-functional theory (DFT) and the local density approximation (LDA).

Finally, Chapter 6 demonstrates a combination of Raman scattering and the first-principles total-energy calculation to investigate the phase transition mechanisms of KIO_3 single crystals. Being a ferroelectric material, KIO_3 single crystals have the largest non-linear optical coefficient among all the iodate crystals, and have been studied extensively for many years. However, until now, there has neither agreement on the phase transition series nor clear understanding of the phase transition mechanisms of KIO_3 single crystals. Moreover, up to date, few theoretical calculations on KIO_3 single crystals have been carried out to study its phase structural properties, although intensive theoretical investigations have contributed significantly to understand the structural properties of ferroelectric crystals, such as the crossover phase transition mechanism from order-disorder to displacive of some prototype ABO_3 perovskites. Thus it would be very meaningful to carry out further research to elucidate the phase transition mechanism in KIO_3. In Chapter 6, we present our detailed Raman study on KIO_3 at variable temperature, and report our first-principles analysis of the ground-state structural and dynamical properties of KIO_3 in rhombohedral phase I, using the DFPT-LDA. It is shown that the theoretical and experimental investigations on KIO_3 benefit from each other, and the combined study contribute to provide a clear understanding of the phase transition mechanism in KIO_3 single crystals.

References

1 R. Merlin, A. Pinczuk, W. H. Weber, J. Menéndez, and D. Gammon, in *Raman scattering in materials science*, (edited by Willes H. Weber, Roberto Merlin, New York: Springer, 2000), p1, p55, p109.

2 M. Cardona, *Light scattering in solids*, edited by M. Cardona; with contributions by M.H. Brodsky, E. Burstein, M. Cardona, L. M.Falicov, M. V. Klein, R. M. Martin, A. Pinczuk, A. S. Pine, and Y. –R. Shen, (Berlin; New York: Springer-Verlag , 1975), p1.

3 S. H. Tolbert and A. P. Alivisatos, Annu. Rev. Phys. Chem. 46, 595 (1995).

4 M. C. Payne, M. P. Teter, D. C. Allan, T.A. Arias and J. D. Joannopoulos, Reviews of Modern Physics, 64, 1045(1992).

Chapter 2

Raman Spectroscopy

2.1 Introduction

In 1928 Professor Chandrasekhara Venkata Raman in India discovered that if monochromatic light passes through a transparent substance and if the scattered light is examined spectroscopically, new weak lines of different frequencies appear in the spectrum in addition to the excitation frequency. This radiation effect that bears his name gained him the 1930 Nobel Prize in Physics. This effect had been predicted in 1923 by Smekal and is sometimes referred to in the early German literature as the Smekal-Raman effect. Also in 1928, independently two Moscow physicists Leonid I. Mandelstam and Grigory S. Landsberg recorded the same effect, and in Russian literature the effect is usually referred to as "combinational scattering".[1,2]

It was soon realized that the newly discovered effect constituted an excellent tool to study excitations of molecules and molecular structures. Such studies dominated the field until about 1940, when the emphasis shifted to systematic investigations of single crystals in order to obtain information for the semi-empirical treatment of their lattice dynamics.[3] However, because of the small scattering cross sections, experiments were difficult and the field remained in the hands of relatively few groups.[3] In mid-1960s, the advent of lasers, which provide strong, coherent monochromatic light in a wide range of wavelength, revolutionized Raman spectroscopy.[4] Since then, Raman spectroscopy has been used as an important analytical technique for the identification of virtually any material.[5]

2.2 Basic definitions

The inelastic scattering of light by molecular and crystal vibrations, i.e. the Raman effect, is caused by modulation of susceptibility (or, equivalently, polarizability) of the medium by the vibrations (as well as the scattering by other excitations in solids, including plasmas, excitons, and magnons, occurs by the same mechanism).[6] If some material is irradiated by monochromatic light of frequency ν_0 (laser), then as a result of the electronic polarization induced in the material by this incident beam, the light of frequency ν_0 as well as that of frequency $\nu_0 \pm \nu_m$ is scattered as shown in Figure 2.1.

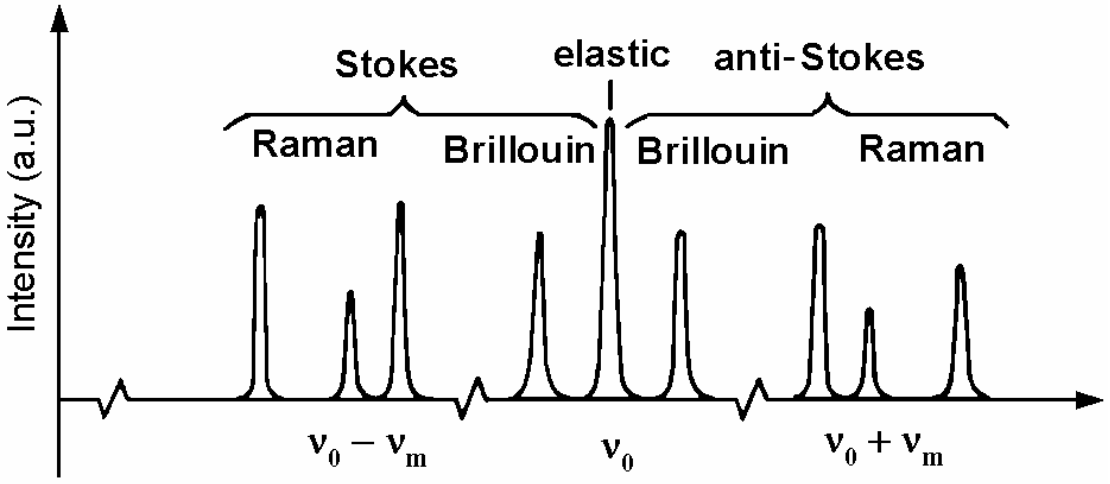

Figure 2.1 Schematic spectrum of scattered light.[6]

The peak in the center of the observed spectrum is the contribution of the incident photons that have been elastically scattered with no change in frequency ("Rayleigh scattering").[4,6] The remaining peaks of frequency $\nu_0 \pm \nu_m$, where ν_m is a vibrational frequency generally, correspond to inelastic scattering and their shifts from ν_0 normally.[6,7] The Brillouin component, resulting from scattering by sound waves,

occurs close to the frequency of the incident light; typical shifts are approximately 1 cm^{-1} or smaller. The Raman component, resulting from scattering by internal vibrations of molecules or optic vibrations in crystals, lies at higher shifts, normally larger than 10 cm^{-1} and often of order 100-1000 cm^{-1}. The basic mechanisms for Brillouin and Raman scattering are essentially the same, but the experimental techniques are different. The inelastic contributions are further subdivided; those scattered frequencies ($\nu_0 - \nu_m$) smaller than ν_0 are known as the Stokes component, while the scattered frequencies ($\nu_0 + \nu_m$) larger than ν_0 form the anti-Stokes component.[6]

2.3 Basic theory

As stated previously, Raman spectra have their origin in the electronic polarization caused by ultraviolet, visible, and near-IR light, and can be understood by an elementary classical theory as below.[4]

Consider a light of wave of frequency ν_0 with an electric field strength E. Since E fluctuates at frequency ν_0, we can write

$$E = E_0 \cos 2\pi\nu_0 t \tag{2.1}$$

where E_0 is the amplitude and t the time. If a diatomic molecule is irradiated by this light, the dipole moment P given by

$$P = \alpha E = aE_0 \cos 2\pi\nu_0 t \tag{2.2}$$

is induced.[4,7] Here α is a proportionally constant and is called the *polarizability*. If the molecule is vibrating with a frequency ν_m, the nuclear displacement q is written

$$q = q_0 \cos 2\pi\nu_m t \tag{2.3}$$

where q_0 is the vibrational amplitude. For a small amplitude of vibration, α is a linear function of q. Thus we can write

$$\alpha = \alpha_0 + \left(\frac{\partial \alpha}{\partial q}\right)_0 q_0 + \ldots \tag{2.4}$$

Here, α_0 is the polarizability at the equilibrium position, and $(\partial\alpha/\partial q)_0$ is the rate of change of α with respect to the change in q, evaluated at the equilibrium position.[7]

Combining Eqs. 2.2-2.4, we have

$$P = aE_0 \cos 2\pi\nu_0 t$$

$$= aE_0 \cos 2\pi\nu_0 t + \left(\frac{\partial \alpha}{\partial q}\right)_0 qE_0 \cos 2\pi\nu_0 t$$

$$= aE_0 \cos 2\pi\nu_0 t + \left(\frac{\partial \alpha}{\partial q}\right)_0 q_0 E_0 \cos 2\pi\nu_0 t \cos 2\pi\nu_m t$$

$$= aE_0 \cos 2\pi\nu_0 t + \frac{1}{2}\left(\frac{\partial \alpha}{\partial q}\right)_0 q_0 E_0 [\cos\{2\pi(\nu_0 + \nu_m)t\} + \cos\{2\pi(\nu_0 - \nu_m)t\}] \tag{2.5}$$

According to classical theory, the first term describes an oscillating dipole which radiates light of frequency ν_0 (Rayleigh scattering), while the second term corresponds to the Raman scattering of frequency $\nu_0 + \nu_m$ (anti-Stokes) and $\nu_0 - \nu_m$ (Stokes). If $(\partial\alpha/\partial q)_0$ is zero, the vibration is not Raman-active. Namely, to be Raman-active, the rate of change of polarizability (α) with the vibration must not be zero.[4,7]

While in actual molecules, both P and E are vectors consisting of three components in the x, y and z direction. Consequently, Eq. 2.2 must be written as

$$P_x = \alpha_{xx}E_x + \alpha_{xy}E_y + \alpha_{xz}E_z$$

$$P_y = \alpha_{yx}E_x + \alpha_{yy}E_y + \alpha_{yz}E_z$$

$$P_z = \alpha_{zx}E_x + \alpha_{zy}E_y + \alpha_{zz}E_z \tag{2.6}$$

In matrix form, this is written as

$$\begin{bmatrix} P_x \\ P_y \\ P_z \end{bmatrix} = \begin{bmatrix} \alpha_{xx} & \alpha_{xy} & \alpha_{xz} \\ \alpha_{yx} & \alpha_{yy} & \alpha_{yz} \\ \alpha_{zx} & \alpha_{zy} & \alpha_{zz} \end{bmatrix} \begin{bmatrix} E_x \\ E_y \\ E_z \end{bmatrix} \tag{2.7}$$

The first matrix on the right-hand side is called the *polarizability tensor*. In normal Raman scattering, this tensor is symmetric; $\alpha_{xy} = \alpha_{yx}$, $\alpha_{xz} = \alpha_{zx}$ and $\alpha_{yz} = \alpha_{zy}$.[4,7] Accordingly, the vibration is Raman-active if one of these components of the polarizability tensor is changed during the vibration.

Raman scattering induced by the vibrations of polyatomic molecules have been introduced classically. Other Raman scattering phenomena, particularly the rotational and electronic Raman effects, are more easily understood as quantum mechanical phenomena.[8]

As a first approximation, the energy of the molecule can be separated into three additive components associated with (1) the motion of the electrons in the molecule, (2) the vibrations of the constituent atoms, and (3) the rotation of the molecule as a whole:[4]

$$E_{total} = E_{el} + E_{vib} + E_{rot} \tag{2.8}$$

The basis for this separation lies in the fact that electronic transitions occur on a much shorter time scale, and rotational transitions occur on a much longer time scale, than vibrational transitions. The translational energy of the molecule may be ignored since it is essentially not quantized. Generally electronic spectra are very complicated because they are accompanied by vibrational as well as rotational fine structure. The vibrational fine structure of the electronic spectrum is easier to observe than the rotational fine structure and provide structural and bonding information about

molecules in electronic excited states. If the molecule is assumed to be a harmonic oscillator, the energy of the vibrational energy level is quantized:

$$E_n = h\nu(n + ½) \tag{2.9}$$

where n is the vibrational quantum number and has values of 0, 1, 2, … etc.

If a molecule is placed in an electromagnetic field (light), a transfer of energy from the filed to the molecule will occur when Bohr's frequency condition is satisfied:[4]

$$\Delta E = h\nu \tag{2.10}$$

where ΔE is the difference in energy between two quantized states, h is Planck's constant, and ν is the frequency of the light.

Suppose that

$$\Delta E = E_1 - E_0 \tag{2.11}$$

where E_1 and E_0 are the energies of the excited and ground states respectively. Then the molecule "absorbs" ΔE when it is excited from E_0 to E_1 and "emits" ΔE when it reverts from E_1 to E_0.[4]

Figure 2.2 illustrates Raman scattering in terms of a simple diatomic energy level.[7] In normal Raman spectroscopy, the excitation line (ν_0) is chosen so that its energy is far below the first electronic excited state. The dotted line indicates a "virtual state" to distinguish it from the real excited state. Generally the selection rule allows any transitions corresponding to $\Delta n = \pm 1$. However, under ordinary conditions, since the population of molecules at n = 0 is much larger than that at n = 1, only the fundamental $n = 0 \rightarrow 1$ transition in the electronic ground state can be observed and the Stokes (S) lines are stronger than the anti-Stokes (A). Since both lines give the same information, it is customary to measure only the Stokes side of the spectrum. Resonance Raman (RR) scattering occurs when the exciting line is chose to E_1 so that its energy intercepts the manifold of an electronic excited state. In the gaseous phase,

this tends to cause resonance fluorescence since the rotational-vibrational levels are discrete. However, in the liquid and solid states, vibrational levels are broadened to produce a continuum due to molecular collisions and/or intermolecular interactions.[4,7] Excitation of these continua produce RR spectra that show extremely strong enhancement of Raman bands originating in this particular electronic transition.[7]

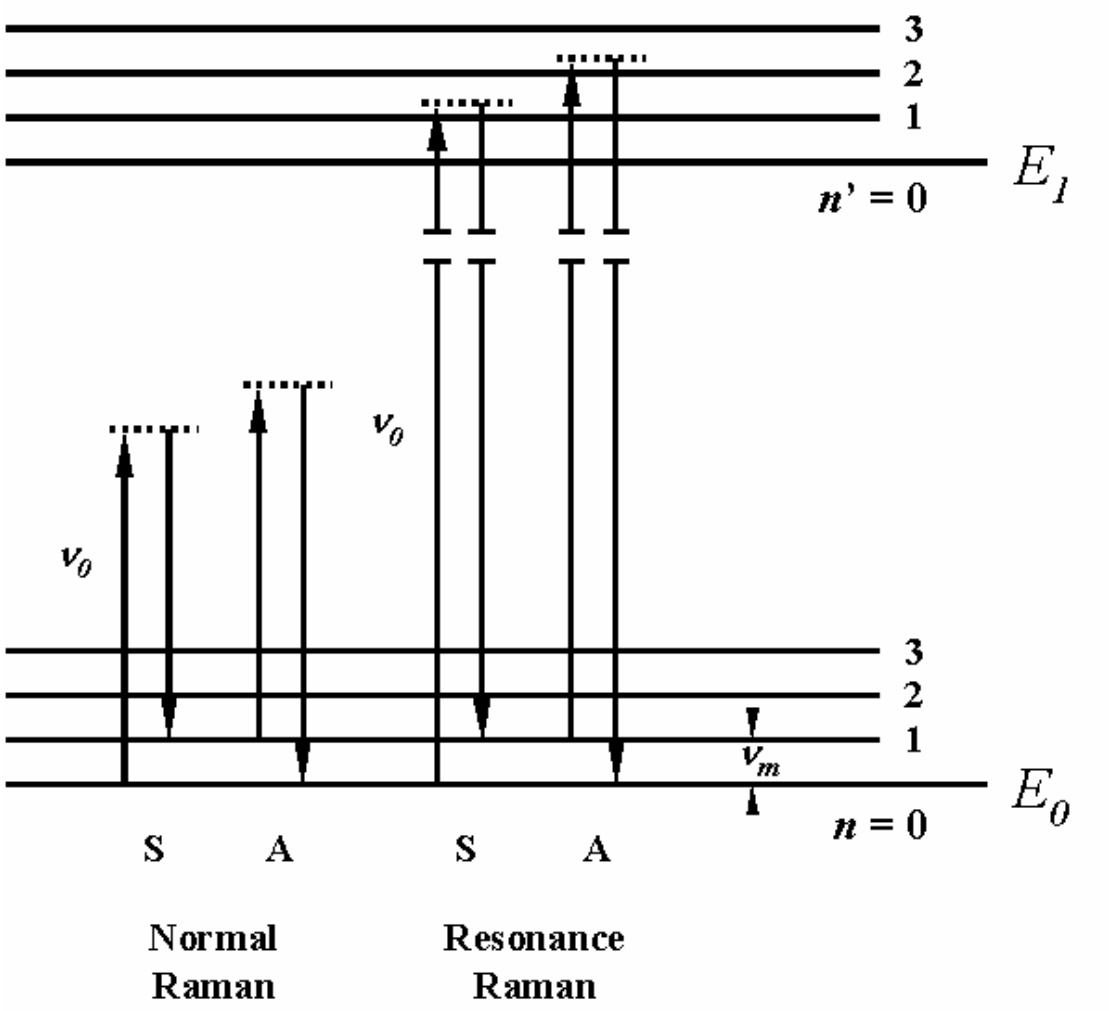

Figure 2.2 Comparison of energy levels for the normal Raman and resonance Raman.

2.4 Raman scattering by phonons

In the previous section, Raman effect associated with the scattering of light by molecular vibrations has been understood. In fact, the group of excitations that can be accessed in Raman experiments is large and is growing as different areas of condensed

matter science evolves.[9] In solid-state media, it includes phonons, magnons, and impurity vibrational modes as well as the elementary excitations of bulk and low-dimensional electronic systems. Raman scattering has become one of the most versatile spectroscopic tools to study the low-lying excitations of condensed matter systems.[9] The measurement of the Raman spectrum of a crystal is one of the main methods for obtaining information about its lattice vibration frequencies.[10]

Raman effect occurs in a crystal, when incident light of angular frequency ω_i interact with the crystal to create or destroy one or more lattice vibration quanta (phonons) and the energy $\hbar\omega$ gained or lost by the lattice is compensated by a decrease or increase in the frequency ω_s of the scattered light ($\omega_s = \omega_i \pm \omega$). The ordinary Raman effect is conveniently divided into two parts: the first-order Raman effect, in which a single phonon is created or destroyed in the scattering process, and the second-order Raman effect, in which two phonons are involved. In addition to these two processes the Raman scattering can be excited by the excitations of the crystal other than lattice vibrations, such as plasmas, spin waves, etc.[10]

Although acoustic lattice vibrations can also give rise to first-order Raman scattering, which is referred to as Brillouin scattering, general Raman researches mainly focus on the Raman scattering from optic vibrations of the lattice. Only lattice vibrations, having certain types of symmetry, give rise to Raman scattering; such vibrations are said to be Raman active, and the phonons in the first-order Raman effect have very long wavelength compared to the lattice constant.[10]

The smallness of the wave vector k of the first-order Raman-active phonons is very important in the discussion of their properties. There is an important distinction between those lattice vibrations, which do or do not produce an electric dipole moment in the lattice and are thus active or inactive respectively in the first-order infra-red

absorption. The frequencies of infra-red-inactive phonons are determined mainly by short-range forces in the lattice. The phonons with wavelength long compared to the lattice constant are not influenced by the dispersive effects of these forces and have essentially the same frequency as infinite wavelength phonons. The Raman shifts thus measure the phonon frequencies at $k = 0$, and no variation in the Raman shifts is produced by variation of the scattering angle or of the relative orientation of the light beams and the crystal axes. However, for infra-red-active phonons, the accompanying long-range electric fields lead to shifts of the frequencies of some of the Raman-active phonons away from their $k = 0$ values, to a lifting of some of the phonon branch degeneracy, and to a variation of frequency with the direction of the phonon wave vector k in non-cubic crystals. A phonon can be simultaneously Raman and infrared-active only in crystal structures, which lack a center of inversion e.g. piezoelectric crystals.[10]

The first-order Raman effect is a scattering process in which a single phonon is either created or destroyed. But in the second-order Raman effect, two phonons participate in the scattering process. They may both be created (giving a Stokes or anti-Stokes component), or finally both may be destroyed (giving an anti-Stokes component). There are two types of second-order Raman Scattering and they give rise respectively to a line spectrum and a continuous spectrum. The second-order line spectrum is due to the process in which light has suffered two successive first-order Raman scatterings. The second-order line spectrum provides no information about the phonon frequencies additional to that provided by the first-order spectrum, and the scattering efficiency for the second-order line spectrum increases with the size of crystal, since the process depends on two successive scattering events, which must both take place within the crystal volume. On the other hand, the second-order

continuum is due to a scattering process in which the light interacts with a pair of phonons in a single event. The continuous frequency distribution displayed by the scattered phonon is proportional to a weighted density of lattice states in which two phonons of equal and opposite wave vector are present. The weighting is due to the frequency and wave vector dependence of the interactions involved in the scattering process. The second-order continuous spectrum results from a single scattering event and the scattering efficiency is therefore independent of the crystal size, as in the first-order Raman effect. [10]

References

1 G. M. Begun, *Fundamental theory and techniques of Raman spectroscopy*, Oak Ridge, Tenn.: Oak Ridge National Laboratory, [1981], p1.

2 V. A. Afanasiev, G. E. Zaikov, *Physical methods in chemistry*, (edited by Vitaly A. Afanasiev and Gennady E. Zaikov, New York: Nova Science, 1992), p87.

3 M. Cardona, *Light scattering in solids*, edited by M. Cardona; with contributions by M.H. Brodsky, E. Burstein, M. Cardona, L. M.Falicov, M. V. Klein, R. M. Martin, A. Pinczuk, A. S. Pine, and Y. –R. Shen, (Berlin; New York: Springer-Verlag , 1975), p1.

4 K. Nakamoto, *Infrared and Raman Spectra of Inorganic and Coordination Compounds*. (Fifth Edition, John Wiley & Sons, Inc., New York, 1997), p1-33.

5 L. Qin, *RAMAN STUDY OF Ge/Si QDs NANO STRUCTURES UNDER HIGH HYDROSTATIC PRESSURE*, Thesis (Ph.D.)--Dept. of Physics, Faculty of Science, National University of Singapore, 2002.

6 W. Hayes, R. Loudon. *Scattering of light by crystals*, (New York: Wiley, 1978), p3-6.

7 J. R. Ferraro, K. Nakamoto, *Introductory Raman spectroscopy*, (Boston: Academic Press, 1994), p15-23.

8 T. R. Gilson, P. J. Hendra, *Laser Raman spectroscopy: a survey of interest primarily to chemists, and containing a comprehensive discussion of experiments on crystals*, (Chichester, Wiley-Interscience, 1970), p9.

9 R. Merlin, A. Pinczuk, and W. H. Weber, *Raman scattering in materials science*, (edited by Willes H. Weber, Roberto Merlin, New York: Springer, 2000), p1.

10 R. Loudon, Advances in Physics. **14**, 425(1964).

Chapter 3

High Pressure Raman Investigations of Ge Nanostructures

3.1 Background

Nanoscale materials that usually present novel properties have become an increasingly important class of materials with numerous potential applications, such as optical devices, micromechanical devices, information storage, and catalysis.[1-5] The unique characteristics of nanoparticles are mainly related to the strong modifications of the fundamental properties of the materials due to the spatial confinement in three dimensions, and the increasing relative significance of the surface-energy contributions associated with the large surface-to-volume ratio of small particles.[1,6] The effects of particle size on optical properties are more pronounced in semiconductor nanocrystals (nc's) or labeled as quantum dots (QDs), which exhibit strong size dependent shift in the band gap.[1,6-13] Semiconductor nc's have been proposed as light-emitting diodes and single-electron transistors,[1,14-17] and have potential applications in non-volatile memory, nanocrystal gate oxide, and "smart" temperature- and light-sensing devices.[1,18-20] Due to their possible applications in integrated optoelectronic devices, the semiconductor nanostructures formed commonly in different matrix, such as Ge/SiO_2 or Si/SiO_2 nanostructures,[21-24] have attracted extensive attention.

Raman scattering spectroscopy is extraordinarily useful in the study of the electronic and vibrational properties of the semiconductor nanostructures. Raman scattering is used to measure a large variety of low energy excitations of the semiconductor nanostructures, including confined and interface phonons, various elementary excitations of confined electron gases and liquids, and transitions of shallow impurities.[25] Until now, Raman scattering has played leading roles in understanding the vibrational properties of quantum wells and the collective excitations of electron gases.[25] Especially, Raman scattering has become one of the most powerful methods to access the stress/strain information on the embedded nc's. Conversely, since the stress/train effects play an important role in tailoring optical and electronic properties of the semiconductor nanostructures, it would be interesting to study the stress/strain effects in semiconductor nanostructures with Raman scattering technique.

In this chapter, the stress/strain effects on the Ge/SiO_2/quartz and Ge/SiO_2/Si(100) nanosystems are investigated by high pressure Raman scattering.

3.2 Experimental

3.2.1 Micro Raman systems

Two micro Raman systems were used in our high pressure Raman experiments described in this chapter. One is the self-assembled micro-Raman system (Fig. 3.1), which consists of a Olympus BH-2 microscope, with a viewing system (CCTV and TV monitor), a He-Ne laser, coupling optics, spectrometer (SPEX1704 czerny-turner spectrometer) and detectors (PMT and CCD).[26] This system was used to monitor the shift of the ruby R1 line for pressure measurement. The other micro-Raman system is a Jobin-Yvon T64000 Raman System, which is a triple grating

spectrograph/scanning spectrometer system (Fig. 3.2), used to record the Raman spectra. The Raman spectra were taken in the backscattering geometry at room temperature using the 488nm (2.541eV) line from a Spectra Physics Stabilite 2017 argon ion laser.

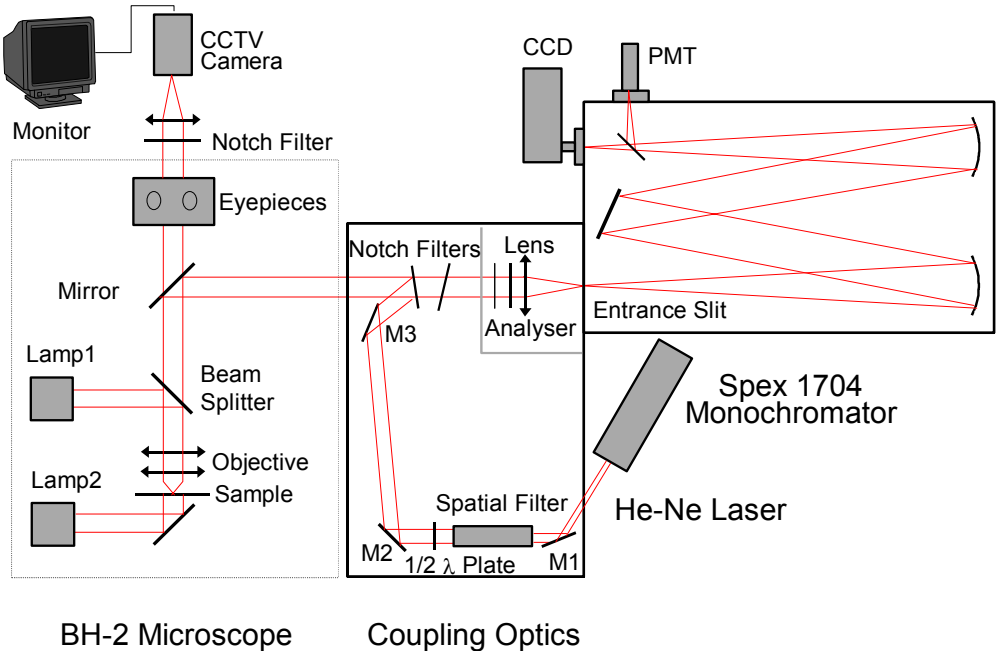

Fig. 3.1 Schematic diagram of the modified Spex micro-Raman spectrometer.[26]

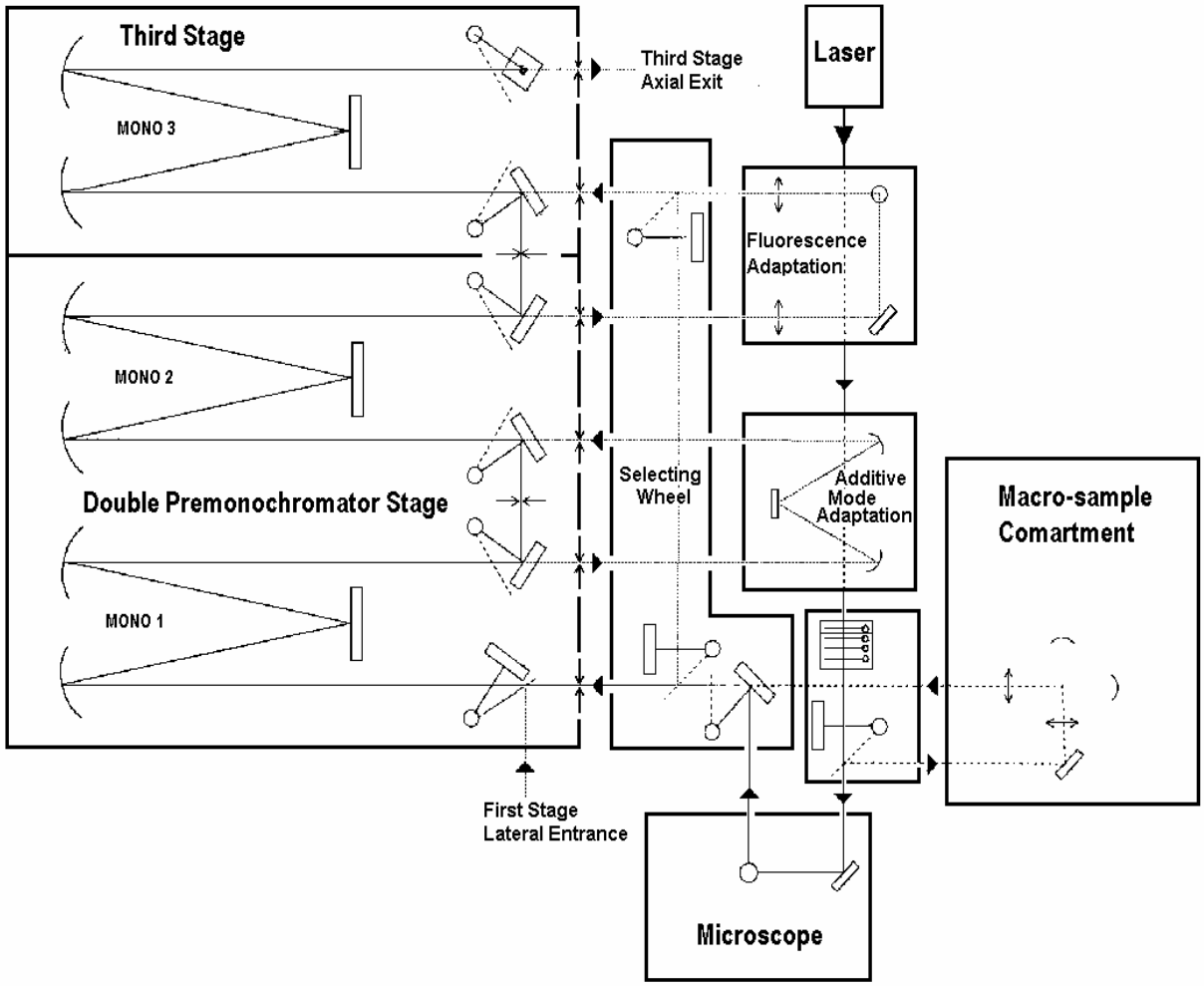

Figure 3.2 Optical Functional Diagram Jobin-Yvon T64000 Raman System (from the manual of this system).

3.2.2 Pressure measurement

Diamond anvil cells (DAC) are commonly used for the generation of very high pressures, which rely on the application of a moderate force using the mechanical advantage of a lever to squeeze a sample between the optically flat and aligned faces of two diamonds with small surface areas.[26-31] The basic principle of the DAC (Fig. 3.3) is that when a metal gasket is compressed between the small flat faces (flattened by grinding and polishing of the culet) of two brilliant cut gem quality diamonds set in

opposed anvil configuration, very high pressure is generated in the gasket hole, which is usually filled with a pressure transmitting medium, or the sample itself.[26]

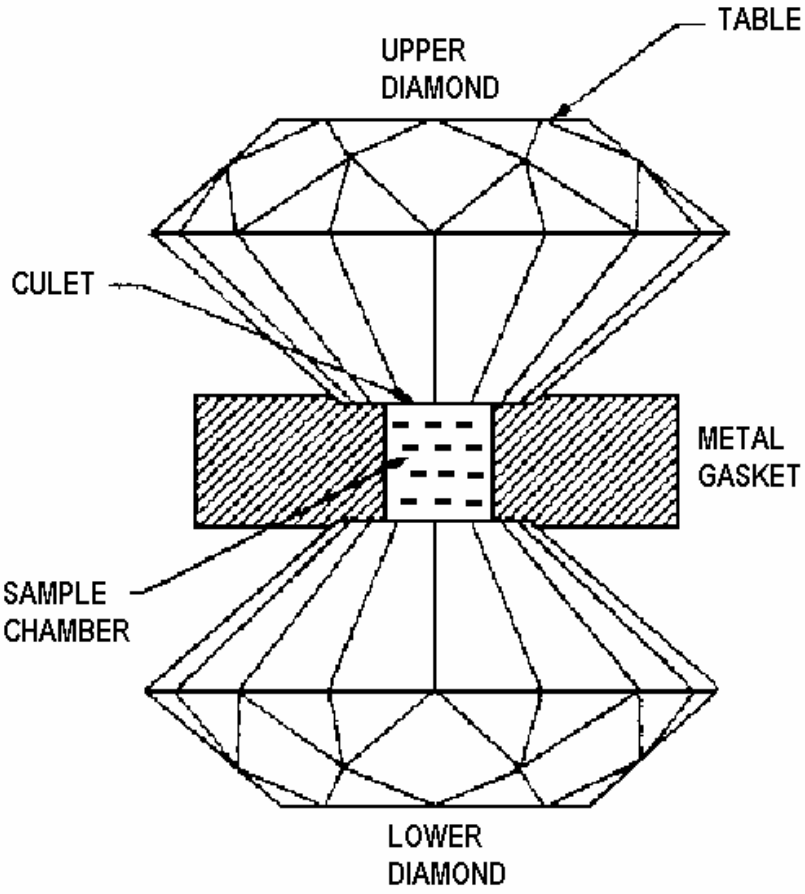

Figure 3.3 Schematic diamond anvil configuration, with a metal gasket for sample

Fig. 3.4 illustrates the compact Bassett cell used in our experiment, which has a threaded gland to apply force on the diamond anvils. The stainless-steel block comprising the main body of the DAC has suitable apertures for the stationary piston and the sliding one, and the latter is held by a key in a slot to prevent it from rotation. The rockers provide translational motion for pressing the gasket between the upper and lower diamonds.[26]

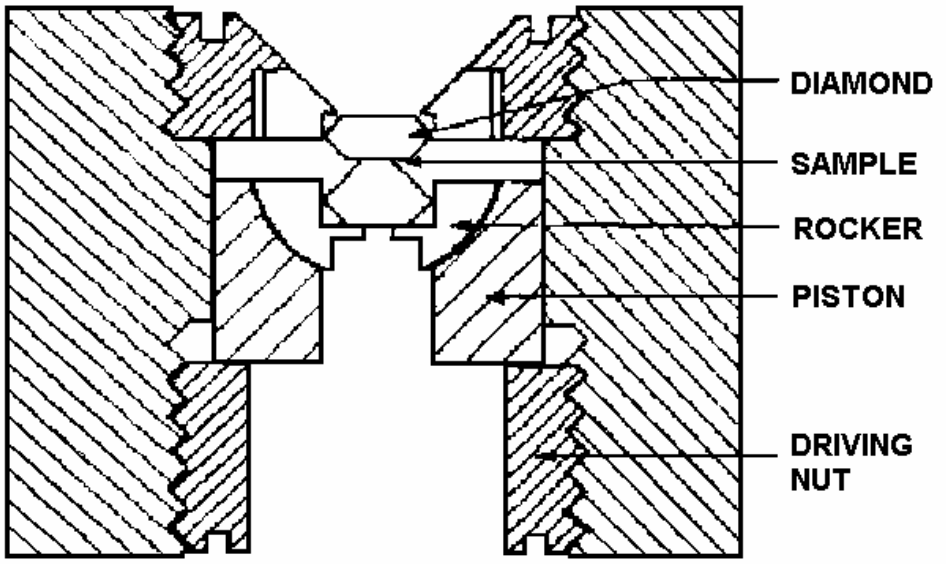

Fig. 3.4 Schematic Bassett-type cell with half-cylindrical rockers for diamond alignment

In DAC, the window material is diamond, which serves the dual purpose of transmitting the pressure and being transparent to the laser and Raman signal. Due to the fact that it is the hardest material known and transmissive throughout most of the electromagnetic region, the diamond window is by far the most valuable for high-pressure studies.

The pressure dependent measurements were carried out using a standard diamond anvil cell technique with a 4:1 mixture of methanol and ethanol as pressure-transmitting medium. A small piece of sample was polished to about 10-20 μm in thickness and cut to ~ 100 μm in linear dimension. This sample was loaded into a gasket with a hole of ~ 250 μm in diameter and of ~ 100μm in thickness. A mixture of four parts of methanol to one part of ethanol was used as pressure medium for hydrostatic experiments. Before filling the hole with the pressure medium, a small chip of ruby was loaded into the gasket hole next to the sample. The ruby fluorescence was used for pressure calibration in the diamond cell. The R lines (R1 at 694.2nm and R2

at 692.7nm) from ruby are quite strong and sharp. In our experiment the R1 line was used since it is stronger. The peak shift is almost linear up to 300 kbar as shown in Figure 3.5.[26,32-34] The pressure coefficient is 0.365 Å $kbar^{-1}$ or 0.753 $cm^{-1}kbar^{-1}$.

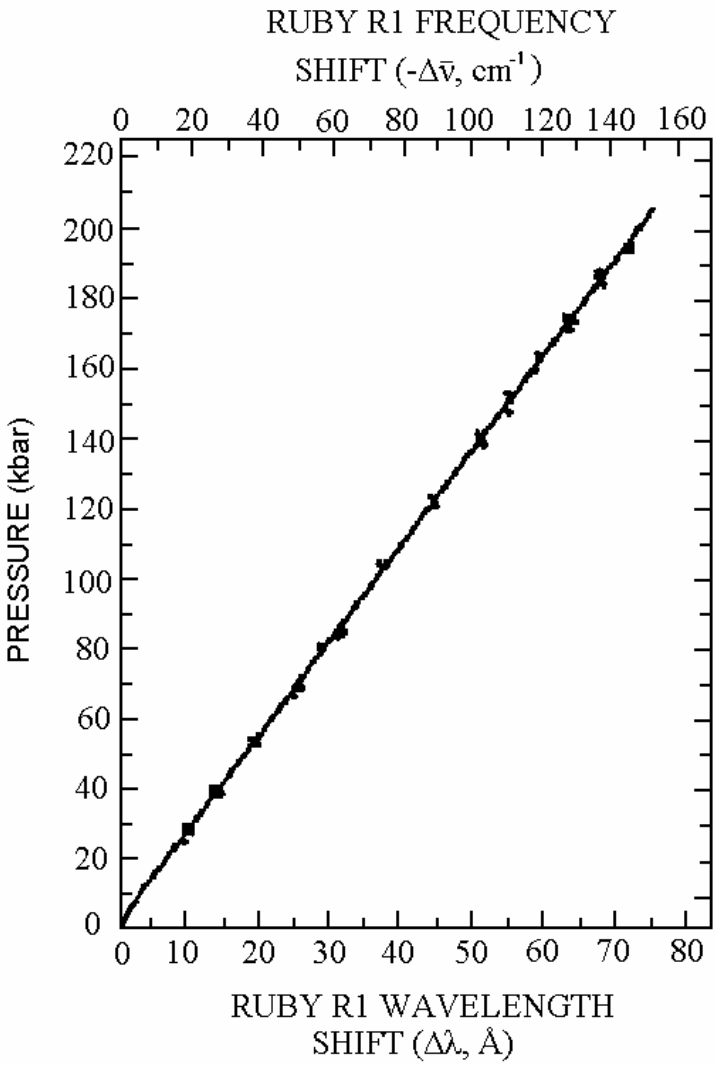

Figure 3.5 Original Calibration for the ruby secondary pressure scale. The R1 fluorescence line (6942 Å at P=0, T = 298K) shifts by 0.365 Å $kbar^{-1}$ or 0.753 $cm^{-1}kbar^{-1}$.[26,32-34]

3.3 High pressure Raman investigations on Ge nc's embedded in glass matrix

Germanium nanostructures have attracted much attention recently due to their possible applications in integrated optoelectronic devices.[35-38] One of the promising ways to fabricate Ge nanostructures is to make embedded Ge nc's in SiO_2 using techniques such as co-sputtering, and ion-implantation and subsequent annealing.[39-41] In nanocrystal-matrix systems, such as Ge/Si islands[42] or quantum dots[43], interface strain is usually observed. Considering the large interface-to-volume ratio in nanocrystal-matrix systems the interface strain plays an important role in deciding the physical and thermodynamic properties of nc's. On Si(001) surface, the nc's of epitaxial Ge were found to repel one another strongly via the strain fields that are produced in the Si substrate.[44] It has also been found that the interface strain has great effect on the growth and evolution of nanocrystalline Ge in matrices.[44-46]

With the application of pressure in Raman scattering,[42,43,47-49] strain in Ge layers is reduced due to the difference in compressibility between Si and Ge. A smaller pressure coefficient ($\alpha = d\omega / dp = 0.34 cm^{-1} kbar^{-1}$) has been observed for the Ge-Ge mode in Ge/Si islands[42] and Ge/Si dot superlattices[43] on Si substrates as compared with the corresponding bulk value ($\alpha = 0.39 cm^{-1} kbar^{-1}$). This is attributed to the fact that Ge islands are strongly constrained by the surrounding Si lattice, leading to a smaller deformation as compared to the bulk Ge when subject to the same pressure.

However, no high pressure experiments have been carried out on the Ge nc's embedded in a rather soft matrix such as SiO_2. Moreover, under pressure the evolution of the interface strain between Ge nc's and the matrix has not been fully investigated. Such information may provide an insight in understanding the formation mechanism of

nanocrystallite Ge embedded in SiO_2. In this section, the hydrostatic pressure dependence of the Ge-Ge mode for Ge nc's embedded into SiO_2 matrix on the quartz-glass substrate is discussed. The evolution mechanism of the interface strain with pressure is discussed in terms of a simple elastic model.

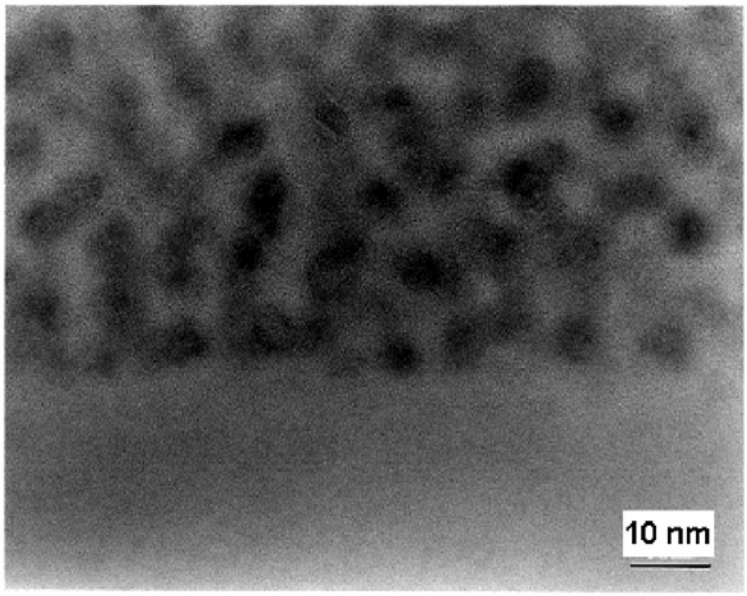

Figure 3.6 TEM image of the annealed Ge nc's.

The samples for investigation were prepared by co-deposition of Ge and SiO_2 by radio-frequency (rf) magnetron sputtering onto quartz-glass substrate. The sample thickness is ~ 1 μm and Ge concentration is ~60 mol.%. After deposition, the sample was annealed for 1 h at 800^{o}C in an argon atmosphere which produced the nc's. Fig. 3.6 shows the transmission electron microscopic (TEM) image of the annealed Ge nc's. One can see clearly that the average size of the Ge nc's is ~ 5nm and the nc's form a kind of continuous network.

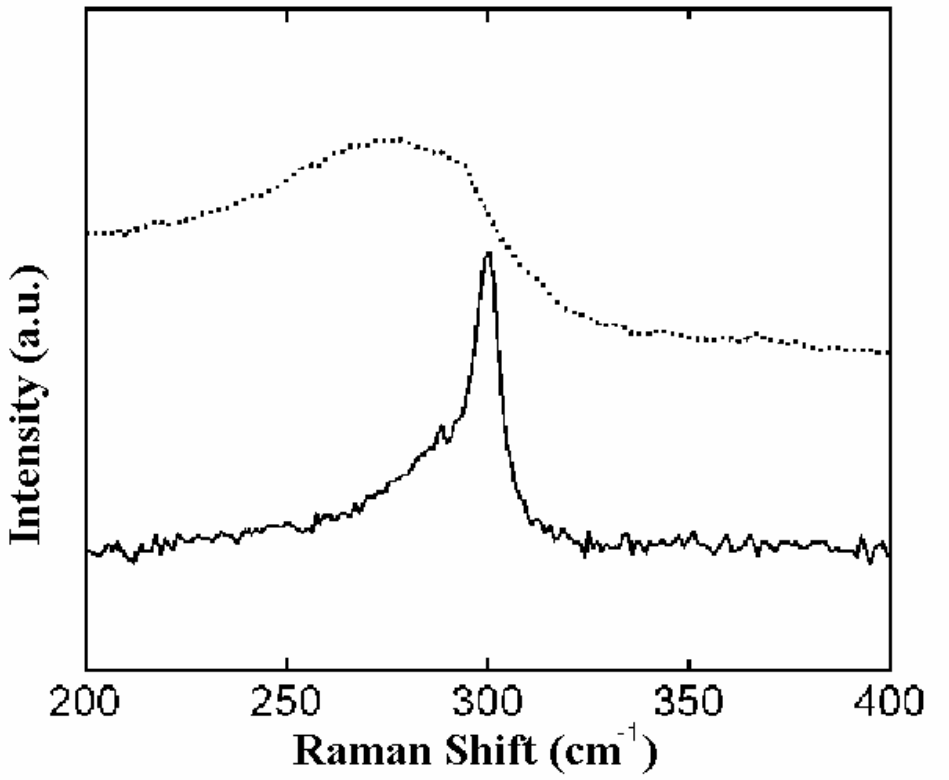

Figure 3.7 Raman spectra for as-deposited (dotted lines) and annealed (solid lines) Ge nc's.

Fig. 3.7 shows the Raman spectra for as-deposited and annealed Ge samples. The appearance of a strong and sharp peak upon annealing indicates the formation of the crystalline phase. In comparison with the bulk Ge, the peak position of the Ge nc's is at 298 cm^{-1}, with an asymmetric profile at the lower frequency. The asymmetric shape of the peak obtained is the characteristic of the small crystals. It is noteworthy that the Ge-Ge mode shifts to lower frequency as the laser intensity increases. To prevent any laser-induced heating, the laser power on the sample is kept to a minimum (~10mW).

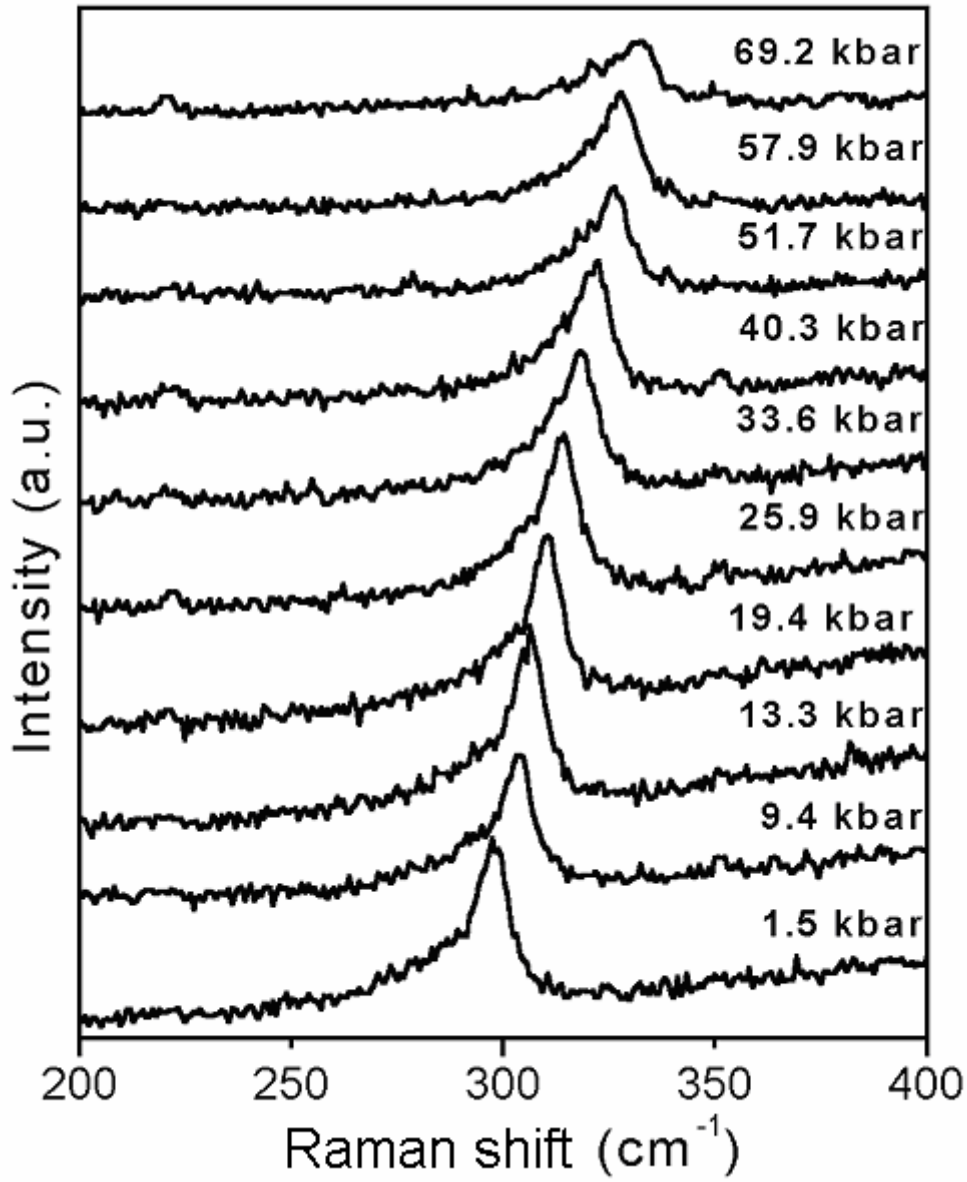

Figure 3.8 Raman spectra of Ge nc's at various pressures under the laser excitation of 488 nm.

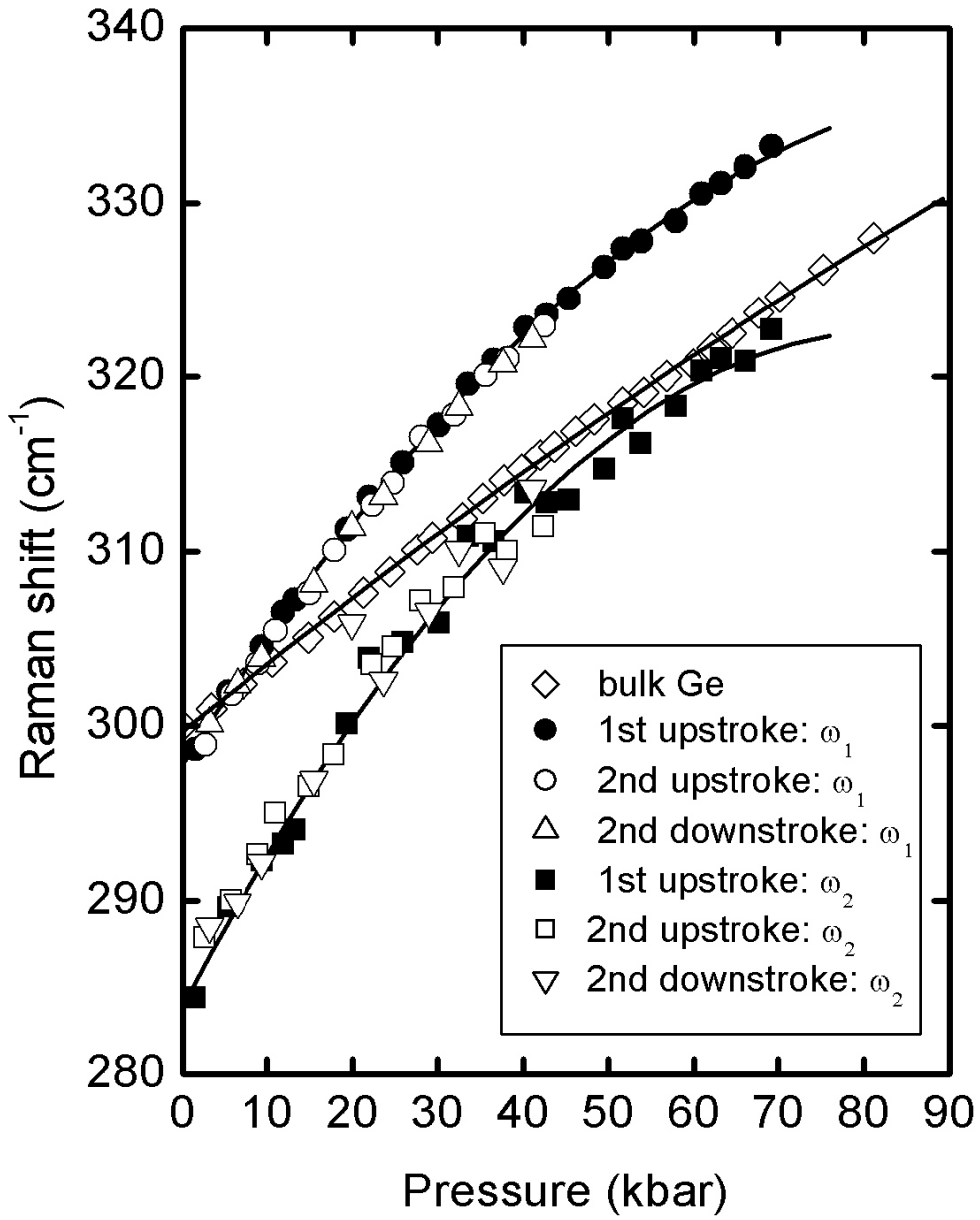

Figure 3.9 Raman shift as function of pressure P of Ge-Ge mode in bulk Ge, Ge nc's and the asymmetric part of the Ge-Ge mode in the Ge nc's

Fig. 3.8 shows the Raman spectra of Ge nc's at various pressures under the laser excitation of 488 nm. With increasing pressure the Ge-Ge mode shift to higher

frequency. The rate of frequency shift of this mode with pressure is shown in Fig. 3.9. The frequency shift of the bulk Ge mode (ω_{bulk}^{Ge}) is also shown for comparison. In order to take into account the behavior of asymmetric profile of the Ge-Ge mode of the Ge nc's, the spectrum is fitted with two Lorentzian peaks. At ambient pressure, the main peak (ω_1^{Ge}) occurs at 298 cm^{-1} with a full-width at half maximum (FWHM) of ~ 7 cm^{-1} and the lower frequency peak (ω_2^{Ge}) at 284 cm^{-1} with FWHM of ~ 20 cm^{-1}. The solid curves correspond to the least-square fits to the experimental data as given by

$$\omega_{bulk}^{Ge}(P) = (299.7 \pm 0.1) + (0.39 \pm 0.01)P \quad (3.1)$$

$$\omega_1^{Ge}(P) = (297.8 \pm 0.2) + (0.77 \pm 0.01)P - (0.004 \pm 0.001)P^2 \quad (3.2)$$

$$\omega_2^{Ge}(P) = (283.9 \pm 0.8) + (0.93 \pm 0.05)P - (0.006 \pm 0.001)P^2, \quad (3.3)$$

Comparing with the bulk Ge, we observed a large $\alpha_{nc} = \frac{d\omega}{dP}$ for the Ge-Ge mode in Ge nc's. In contrast with the previous Raman scattering observation on Ge/Si islands of different sizes grown on Si substrates (hut-cluster[42] of diameter ~ 20nm and Ge/Si dot superlattice[43] of ~ diameter 8nm), the $\alpha_{island} = \frac{d\omega}{dP}$ for the Ge-Ge mode is found to be ~ 0.34 $cm^{-1}kbar^{-1}$. Consequently, the $\frac{d\omega}{dP}$ should be independent of the size effect but related to the host matrix. The large $\frac{d\omega}{dP}$ observed for the Ge nc's in the SiO_2 matrix on Si substrate can be explained if we assume that the pressure acting on the nc's is different from the surrounding pressure from the outside pressure-transmitting medium. This effect has been observed by Haselhoff *et al*[50] for CuCl nc's in alkali-halide matrices. However, in their model the strain at the interface between the nc's and the matrix was not taken into account.

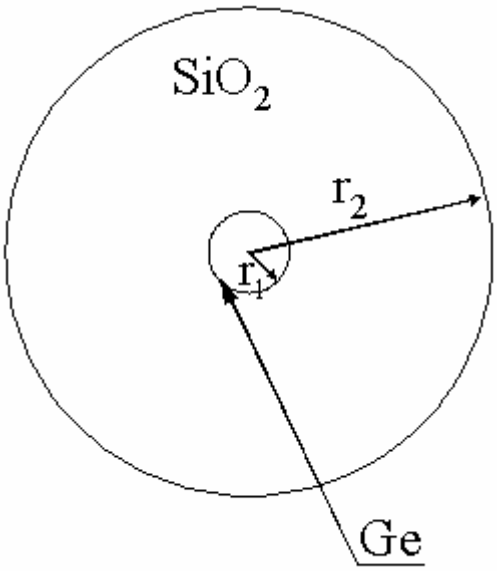

Figure 3.10 Schematic model (of the Ge/SiO_2 nanocrystal-matrix system) used in analyzing the effective pressure.

The pressure dependence of the Ge-Ge modes of nc's for one pressure cycle is shown in Fig. 3.9. There is no hysteresis observed; which confirms that the pressure-induced strain in the nc's is reversible. With this elastic behaviour of our Ge/SiO_2 nanocrystal-matrix system, we assume both nc's and the matrix as isotropic elastic continua[50] in our model as shown in Fig. 3.10. We consider the nc's as spheres of radius r_1 in a spherical matrix of radius r_2, where $r_2 >> r_1$. The system is subject to a hydrostatic pressure P. In spherical coordinates, with the origin at the center of the nc sphere, the displacement vector $\bar{u}$ is everywhere radial and can be written as $u = ar + b/r^2$. The components of the strain tensor are $u_{rr} = a - 2b/r^3$ and $u_{\theta\theta} = u_{\phi\phi} = a + b/r^3$, where the constants a and b are determined from the boundary conditions. At the interface between the nc's and the matrix, the interface strain is given as $\delta = u^1_{\theta\theta} - u^2_{\theta\theta}$, where $u^1_{\theta\theta}$ and $u^2_{\theta\theta}$ are the strain tensor of the nc's and the

matrix respectively. From the boundary conditions at $r = r_1$, the pressure P_{NC} at the nc's is given by[51]

$$P_{NC} = P\frac{9K_1(1-\sigma_2)}{2E_2 + 3(1+\sigma_2)K_1} + \delta\frac{6E_2K_1}{2E_2 + 3(1+\sigma_2)K_1} \qquad (3.4),$$

where the (E_1, σ_1, K_1) and (E_2, σ_2, K_2) are the Young's modulus, Poisson's ratio, and bulk modulus of the nc's and the matrix, respectively. From Eq. (3.4), we have

$$\frac{dP_{NC}}{dP} = \frac{9K_1(1-\sigma_2)}{2E_2 + 3(1+\sigma_2)K_1} + \frac{6E_2K_1}{2E_2 + 3(1+\sigma_2)K_1}\frac{d\delta}{dP} = k_1 + k_2\frac{d\delta}{dP} \qquad (3.5).$$

In our case for the Ge nc's, Eq. (3.5) gives $\frac{dP_{NC}}{dP} = \frac{\alpha_{nc}}{\alpha_{bulk}} = \frac{0.77}{0.39} = 1.97$. Using the elastic constants of Ge ($E_1 = 1316.6kbar$, $\sigma_1 = 0.20748$, $K_1 = 750.17kbar$),[52] and SiO_2 ($E_2 = 730kbar$, $\sigma_2 = 0.162$, $K_2 = 361kbar$),[53] we find from Eq. (3.5) that $k_1 = 1.39$ and $k_2\frac{d\delta}{dP} = 0.58$. The positive value of $\frac{d\delta}{dP}$ indicate that the accumulated strain at the interface induce a compressive stress on the nc's as pressure increases. This is possible since SiO_2 ($K_2 = 361kbar$) is much easier to compress than Ge ($K_1 = 750.17kbar$). As such, the large pressure coefficient for Ge nc's comes from the contribution of the stress at the interface evolving with pressure.

On the other hand, for the case of Ge/Si islands,[42] Eq. (3.5) gives $\frac{dP_{NC}}{dP} = \frac{\alpha_{islands}}{\alpha_{bulk}} = \frac{0.34}{0.39} = 0.87$. With the Si matrix of elastic constant values ($E_3 = 1629.1kbar$, $\sigma_3 = 0.22262$, $K_3 = 978.87kbar$),[52] we obtained $k_1 = 0.87$ and $k_2\frac{d\delta}{dP} \approx 0$. This is consistent with the fact that, the smaller compressibility of Si "isolates" the Ge islands from the external pressure, reducing $\alpha_{islands}$ for Ge islands (0.34 cm^{-1} $kbar^{-1}$) as compared to the bulk Ge value (0.39 cm-1 kbar-1).[42]

3.4 High pressure Raman investigations on Ge/SiO_2/Si nanostructures

As introduced in the previous section, generally in the nanocrystal-matrix systems the distribution of the stress and strain field plays an important role in deciding the physical and thermodynamic properties of nanostructures. The investigations on the elastic field in the nanocrystal-matrix systems would enhance our understanding on the strain mechanism of the nanostructures as well as the exploitation of their novel functions.

In Section 3.3, the pressure coefficient ($\alpha = 0.77 cm^{-1} kbar^{-1}$) of the Ge-Ge mode for Ge nc's embedded in glass matrix is observed to be almost twice as large as its corresponding bulk value. This has been explained using a simple elastic model, which describes the effective pressure transmitted from the matrix to the nanocrystals. However, the interface strain/stress effects under applied hydrostatic pressure has not been fully understood in a more complicated nanosystem, such as Ge or Si nc's embedded in SiO_2 on Si substrate. For example in the high pressure photoluminescence (PL) measurement of Si nc's in SiO_2 layers on the Si substrate by Cheong et al,[54] the observed pressure coefficients of the PL peak energy on the two Si nanocrystal samples A and B gave different values of -0.4 and -0.6 meV/kbar respectively, which were not in good quantitative agreement with an estimate based on the quantum confinement model. Both samples were formed by ion implantation of Si^+ ions into thermally oxidized Si wafers followed by thermal annealing, but with different thickness of SiO_2 layers. In addition, in the first pressure cycle on sample B (thicker one), a considerable hysteresis was observed but not in the second cycle. Cheong *et al* suggested that the initial hysteresis was due to an irreversible pressure-induced relief of built-in strains in the nanocrystals, but no explanation was given for why this particular sample has built-in strains.[54] Therefore, it is necessary to carry out

high-pressure researches further on the multi-component nanosystems, to elucidate the strain/stress effect on the nc's in the nanostructures. Moreover since desired functional characteristics of semiconductor heterostructure depend crucially on their structure and geometry which are generally influenced by the local elastic field distribution during its fabrication or application, further investigations on multi-component nanostructures, such as Ge/SiO_2/Si nanosystem, may cast an insight in exploring the formation or application of semiconductor nanostructures.

In this section, the high pressure Raman scattering investigations on Ge nc's embedded in SiO_2 matrix on Si substrate is discussed. In this nanosystem in which the Ge nc's and the Si substrate have different Raman frequency (Ge-Ge mode ~ 300 cm^{-1} and Si-Si mode ~ 521 cm^{-1}), it would be much easier to make clear the different strain effects on the nc's and the substrate than in the Si/SiO_2/Si nanosystem. It is noted that the Si acoustic peak at ~300 cm^{-1} can be effectively eliminated by using the specific polarization configuration.[42] Moreover, our experiments on 5, 8, and 20 nm nc's[42,43,55] suggested that the Raman shifts with pressure ($\alpha = d\omega / dp$) is independent of the size of the nc's, which is consistent with the common understanding[56] based on the high-pressure Raman experiments on CdS and CdSe that the potential energy as a function of unit cell volume is identical in both the harmonic and the first anharmonic term in tetrahedrally bonded bulk and nanocrystal systems. This simplifies the study of the mechanism of the elastic field evolution with the surrounding hydrostatic pressure since we can neglect the size effect of the nc's.

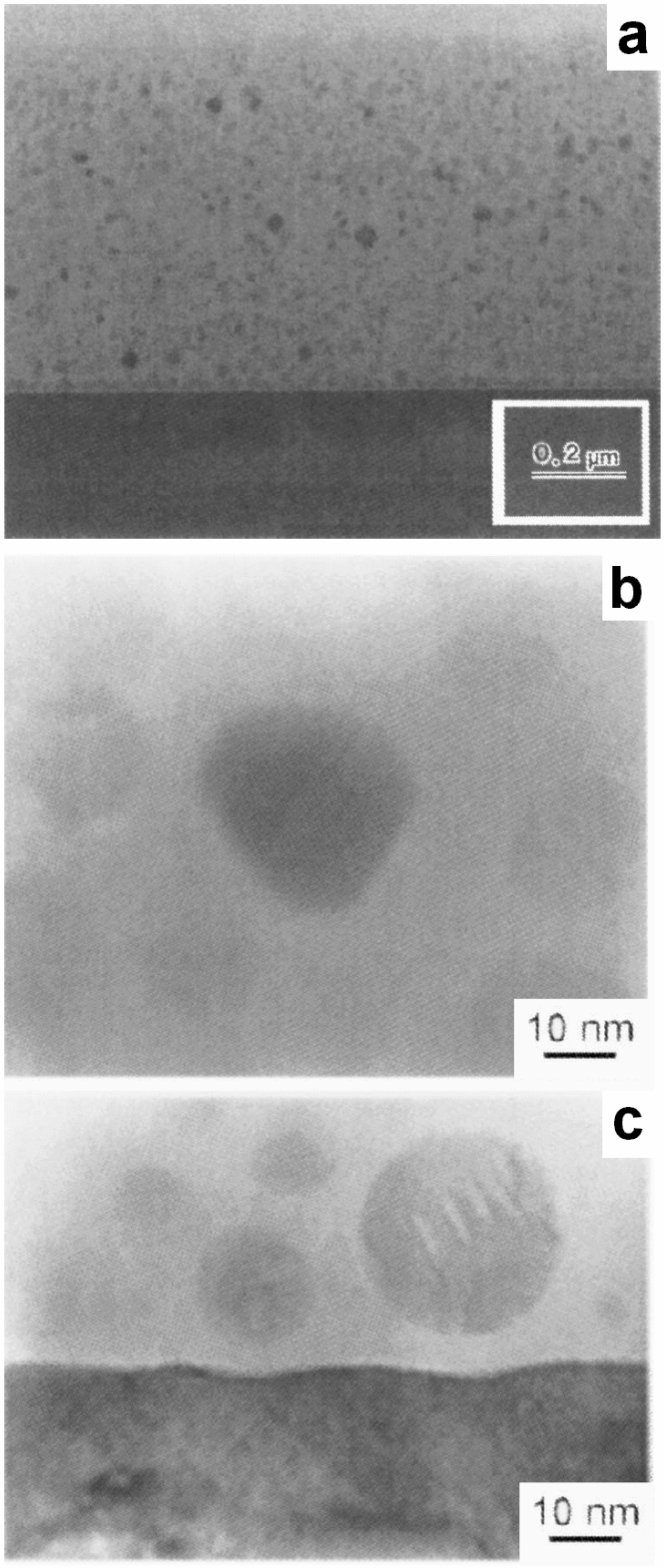

Figure 3.11(a) TEM image of $Ge/SiO_2/Si$ nc's samples; (b) HR-TEM image of $Ge/SiO_2/Si$ nc's samples with Ge nc's formed in the bulk of the sample; and (c) in the vicinity of the Si(100) interface.

The samples for investigation were prepared by co-deposition of Ge and SiO_2 by radio-frequency (rf) magnetron sputtering onto Si(100) substrate with about 3-5 nm thick native oxide. The sample thickness is ~ 1 μm and Ge concentration is ~60 mol.%. After deposition, the sample was annealed for 1 h at 800^{o}C in an argon atmosphere, which produced the nc's.

Fig. 3.11(a) shows the transmission electron microscopic (TEM) image of the annealed Ge nc's[57]. Interestingly, the nc's are preferentially formed in the area away from the sample surface, and at the interface with the silicon substrate the density of the nc's is somewhat higher. High-resolution (HR) TEM images [Fig. 3.11(b)&(c)] reveal other features of the formed nc's. The nc's formed in bulk of the sample have clearly pronounced facets and are single crystals, in very few cases with twinning defects. The nc's formed in the direct vicinity of the Si substrate, on the other hand, are spherical and the interface under these nc's no longer flat. The size of the nc's is almost the same in both regions and is ~ 20 nm.

Fig. 3.12(a) shows the Raman spectra for the Ge/SiO_2/Si sample at ambient pressure. The Ge-Ge mode occurs at ~ 300 cm^{-1} with a full width at half maximum (FWHM) of about 5 cm^{-1} while the Si-Si mode from the substrate is at ~ 521 cm^{-1} with a FWHM of about 4 cm^{-1}. The appearance of the strong and sharp peak of the Ge-Ge mode indicates the formation of the crystalline phase. Here the polarization configuration $001(100,010)00\bar{1}$ was used to minimize the Si acoustic phonon peak at ~303 cm^{-1}. It is noted that the Ge-Ge mode shifts to lower frequency as the laser intensity increases. To prevent any laser induced-heating, the laser power on the sample is kept to a minimum (~10mW).

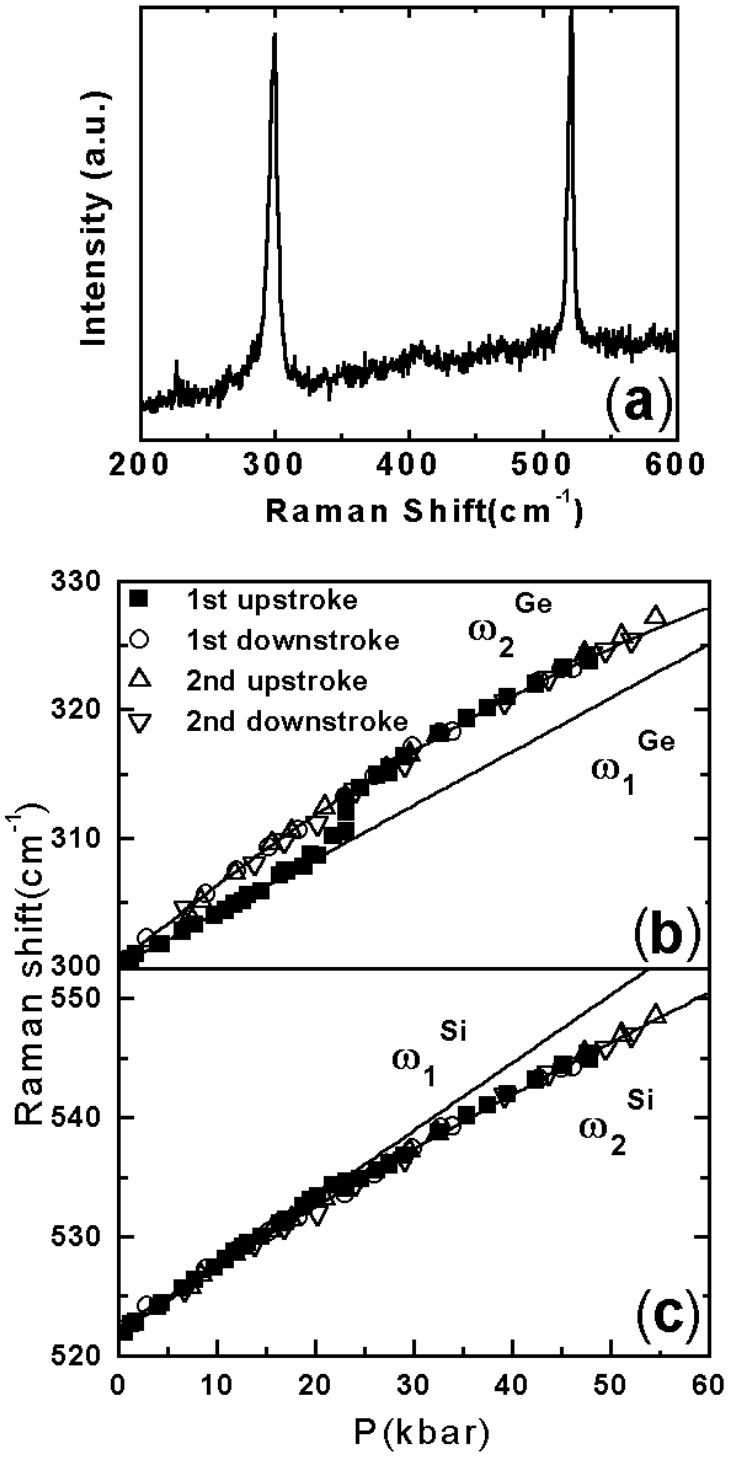

Figure 3.12 Raman spectra of $Ge/SiO_2/Si$ nc's samples at ambient pressure (a); Pressure dependence of Raman shift of the Ge-Ge mode of Ge nc's (b) and the Si-Si mode of the Si substrate(c).

The Raman shifts of the Ge-Ge mode and Si-Si mode with pressure *P* for two pressure cycles were shown in Fig. 3.12(b)&(c), where both the Ge and the Si peaks were fitted to the Lorentzian profile. During the first upstroke of the pressure cycle, the Ge-Ge mode shifts linearly with *P* and then shows a step jump up from 310.4 to 313.8 cm^{-1} at P~ 23 kbar, and subsequently shifts up with P at a higher pressure coefficient (α). On the other hand, at P~ 23 kbar, the Si-Si mode shifts down by ~ 0.3 cm^{-1}, and thereafter the Si mode shifts up at a lower pressure coefficient (α). The results show that at P~ 23 kbar in the first upstroke of pressure, there exists an irreversible transition in the strain effect of Ge/SiO_2/Si nanosystem. In the last part of the first upstroke (i.e. beyond 23 kbar) and the first downstroke, α remained unchanged. The second pressure cycle shows that both the Ge-Ge and Si modes keep the reversible Raman shift with pressure with the same α as the first downstroke of pressure cycle. It is noteworthy that although the present high pressure experiment is performed on Ge nc's of size ~ 20nm, we have also observed similar behavior in Ge nc's of size 4nm to 12 nm with the same SiO_2 layer thickness indicating the observed phenomenon is independent of nc's size.

As shown in Fig. 3.12(b)&(c), the solid curves correspond to the least-square fits to the experimental data, where the Raman modes before (ω_1) and after (ω_2) the transition at P~ 23 kbar was fitted separately:

$$\omega_1^{Ge}(P) = (300.0 \pm 0.1) + (0.42 \pm 0.01)P \tag{3.6}$$

$$\omega_2^{Ge}(P) = (300.2 \pm 0.2) + (0.64 \pm 0.02)P - (0.003 \pm 0.001)P^2 \tag{3.7}$$

$$\omega_1^{Si}(P) = (521.7 \pm 0.1) + (0.57 \pm 0.01)P \tag{3.8}$$

$$\omega_2^{Si}(P) = (522.3 \pm 0.2) + (0.53 \pm 0.01)P - (0.001 \pm 0.0002)P^2 \tag{3.9}$$

These fitting results show that after the irreversible transition at 23 kbar, α of Ge-Ge mode changes from 0.42 to 0.64 $cm^{-1}kbar^{-1}$ and α of Si-Si mode changes from 0.57 to 0.53 $cm^{-1}kbar^{-1}$. It is noteworthy that the elastic field distribution would not be uniformly homogeneous in the $Ge/SiO_2/Si$ nanosystem, especially near the interface between the SiO_2 matrix and the Si substrate. Thus, it is necessary to investigate the elastic field distribution in the $Ge/SiO_2/Si$ nanosystem to enhance the understanding in the pressure dependence of the Raman shifts of the Ge-Ge and Si modes.

Using a finite element package (ABAQUS/Standard), an axisymmetric model structure as shown in Fig. 3.13, where the Ge nc's sphere embedded along the rotation z-axis, the Si substrate and SiO_2 matrix cylindrical layers are separated by a sharp interface, was chosen to study the elastic field distribution in the nanosystem under the hydrostatic pressure of 10 kbar. For simplicity, the Ge nc's, the SiO_2 matrix and Si substrate were considered as isotropic elastic continua, with elastic constants of Ge ($E_1 = 1316.6kbar$, $\sigma_1 = 0.20748$, $K_1 = 750.17kbar$),[52] of SiO_2 ($E_2 = 730kbar$, $\sigma_2 = 0.162$, $K_2 = 361kbar$),[53] and of Si ($E_3 = 1629.1kbar$, $\sigma_3 = 0.22262$, $K_3 = 978.87kbar$)[52] separately. Here $(E_i, \sigma_i, K_i)_{i=1,2,3}$ are the Young's modulus, Poisson's ratio, and bulk modulus, respectively.

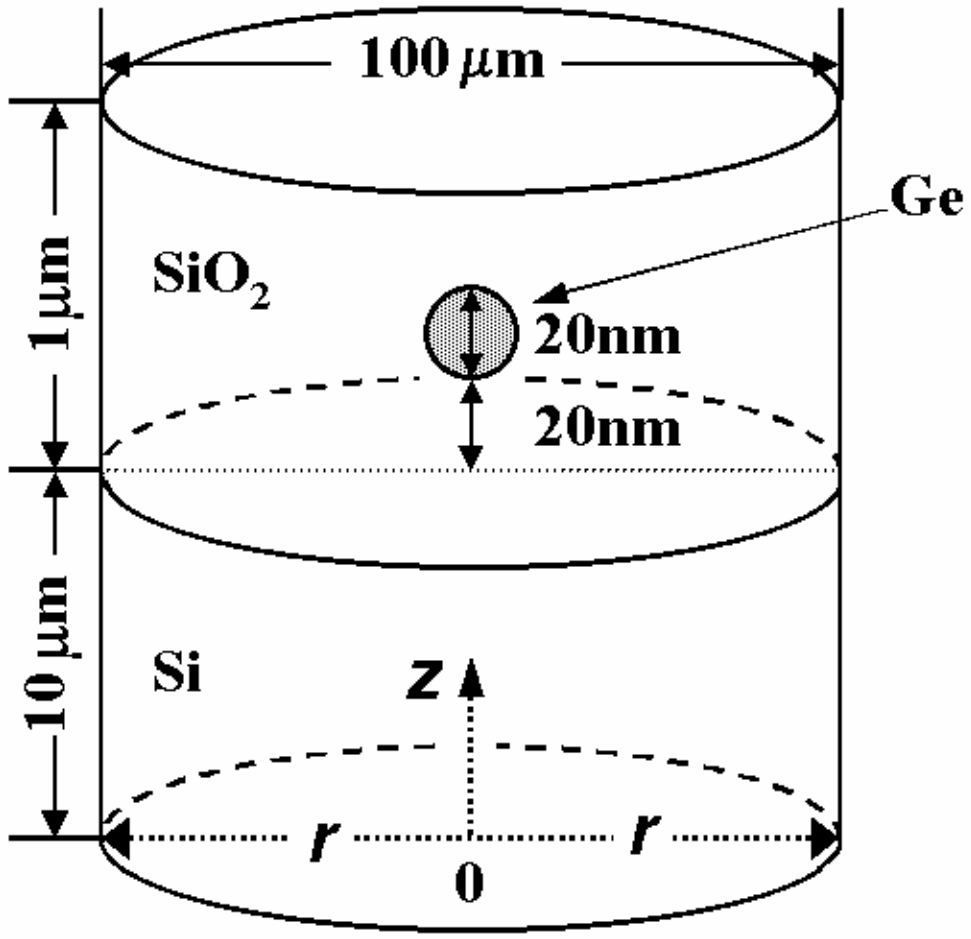

Figure 3.13 Schematic structure of $Ge/SiO_2/Si$ axis symmetrical nanostructure modeled.

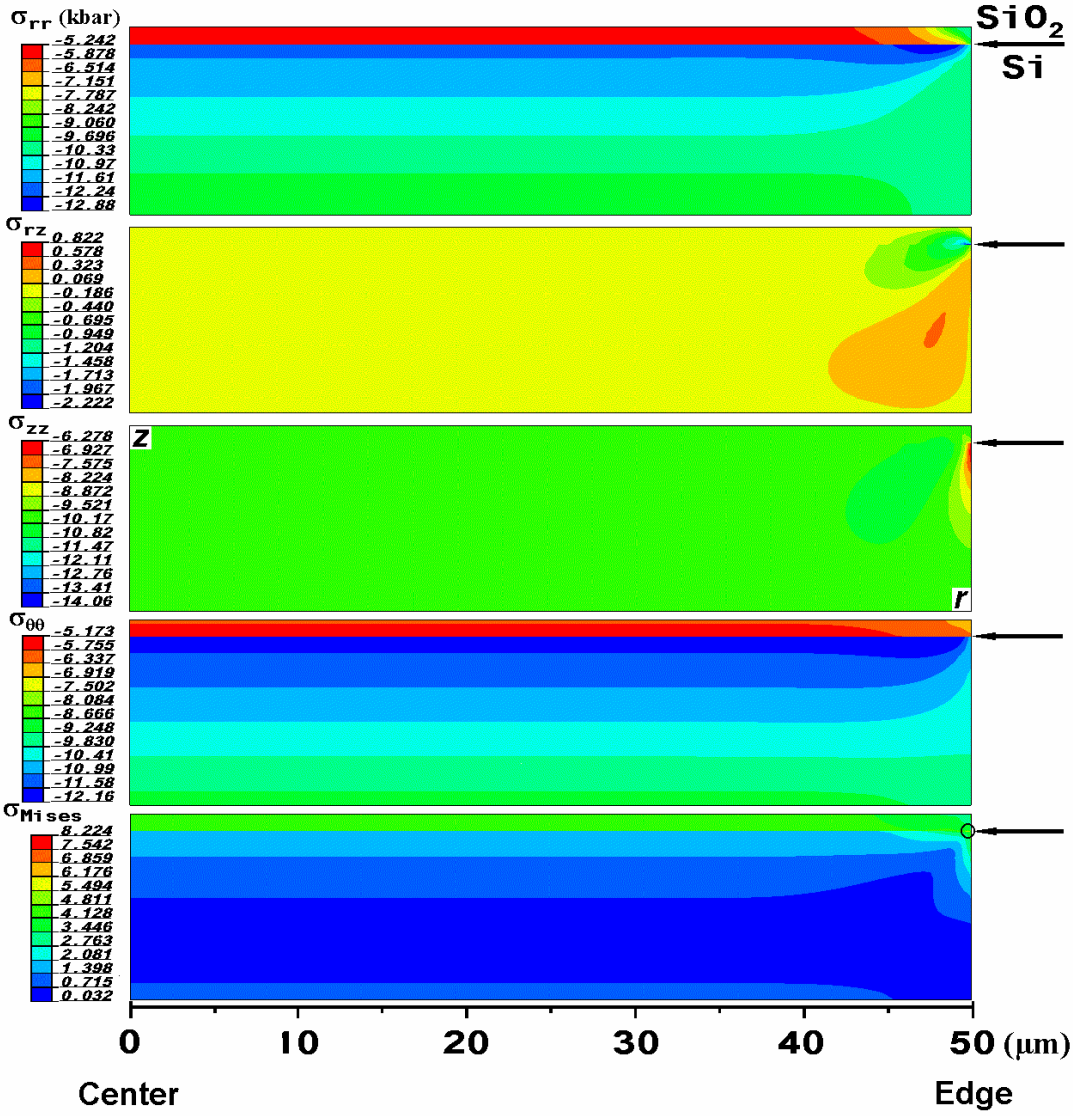

Figure 3.14. Global r - z plane stress distributions of σ_{rr}, σ_{rz}, σ_{zz}, $\sigma_{\theta\theta}$, and σ_{Mises} for the disk-shaped Ge/SiO_2/Si nanosystem, with the arrows pointed at the SiO_2/Si interface.

Fig. 3.14 shows the r - z plane stress distributions of σ_{rr}, σ_{rz}, σ_{zz}, $\sigma_{\theta\theta}$, and σ_{Mises} for the disk-shaped Ge/SiO_2/Si nanosystem, where the negative values indicate the compressive stress. All the five stress tensors distribute rather non-homogeneously around the nanosystem surface, and near the SiO_2/Si interface. However, in the most part of the SiO_2 matrix, away from the outer surface, the stress distributions of the five

stress tensors are quite homogeneous. This is consistent with the experimental results that the linewidth of Ge-Ge mode remains constant with increasing pressure indicating no significant inhomogeneous broadening.

At the SiO_2/Si interface, there is a significant discontinuity for σ_{rr} and $\sigma_{\theta\theta}$. The value of σ_{rr} jumps from -5.242 *kbar* at the SiO_2 matrix to -12.88 *kbar* at the Si substrate and the value of $\sigma_{\theta\theta}$ jumps from -5.173 kbar at the SiO_2 matrix to -12.16 kbar at the Si substrate. This can be ascribed to the fact that SiO_2 ($K_2 = 361 kbar$) is much easier to compress than Si ($K_3 = 978.87 kbar$), but both of them have to shrink together at the interface under pressure. As a result, the SiO_2 matrix experiences more tensile stress near the SiO_2/Si interface than anywhere else. On the other hand, the Si substrate has to undergo a more compressive stress. Accordingly, the values of σ_{rr} and $\sigma_{\theta\theta}$ for SiO_2 matrix become smaller from the top surface to the SiO_2/Si interface, while σ_{rr} and $\sigma_{\theta\theta}$ of Si substrate become bigger from the bottom surface to the SiO_2/Si interface. Consequently, before the transition at 23 kbar, the α of the Ge-Ge (~0.42 $cm^{-1}kbar^{-1}$) and Si modes (~0.57 $cm^{-1}kbar^{-1}$) can be due to the discontinuous distribution of σ_{rr} and $\sigma_{\theta\theta}$ in the nanosystem introduced by the SiO_2/Si interface. As a result of the concentration of the discontinuous stresses, the interface strain and interface tension would accumulate accordingly, which may induce the debonding of the SiO_2/Si interface, i.e. the delaminating of the SiO_2 matrix and Si substrate layers. The delaminating behavior at the SiO_2/Si interface could be further understood by the distribution of (Von) Mises stress[58] σ_{Mises} (Fig. 3.14). The local distribution of σ_{Mises} at the outer SiO_2/Si interface edge (the enlarged circle part in the Fig. 3.13) was magnified as shown in Fig.3.15 (a), together with the local stress distribution of σ_{Mises},

σ_{rr}, σ_{rz}, σ_{zz}, and $\sigma_{\theta\theta}$ around Ge nc's (embedded along the rotation z-axis as shown in Fig. 3.13). The distribution of σ_{Mises} concentrates strongly at the outer SiO_2/Si interface edge ($r = r_{MAX} = 50\mu m$) indicates further that the delaminating could start from the edge where the largest strain energy is accumulated and gradually move inwards. Due to this delaminating behavior, we are able to explain our experimental observation for the discontinuity at P~ 23 kbar.

From the local stress distributions around Ge nc's (Fig. 3.14), we can further understand the characteristics of the Ge/SiO_2/Si nanosystem. Due to the smaller compressibility of Ge ($K_1 = 750.17 kbar$) nc's than the SiO_2 ($K_2 = 361 kbar$) matrix, Ge nc's undergo a rather larger stresses of σ_{rr}, σ_{zz}, and $\sigma_{\theta\theta}$ than the surrounding SiO_2 matrix. Moreover, the discontinuous and nonuniform stress distribution of σ_{rr}, σ_{rz}, σ_{zz}, and $\sigma_{\theta\theta}$ can be observed around the Ge/SiO_2 interface. In the SiO_2 matrix, the existence of Ge nc's effectively modified the surrounding elastic field, of a nonuniform stress distribution with the scale comparable with the size of the nc's. Similarly, Ge nc's can also introduce nonuniform local stress during cooling or heating in the high temperature growth of the Ge/SiO_2/Si nanosystem due to different thermal expansion coefficients. The roughness of the Si/SiO_2 interface under the nc's with the local geometry corresponding to the shape of nc's, as shown in Fig. 3.11(c), could be due to the nonhomogeneous local stress distribution induced by the embedded Ge nc's during fabrication.

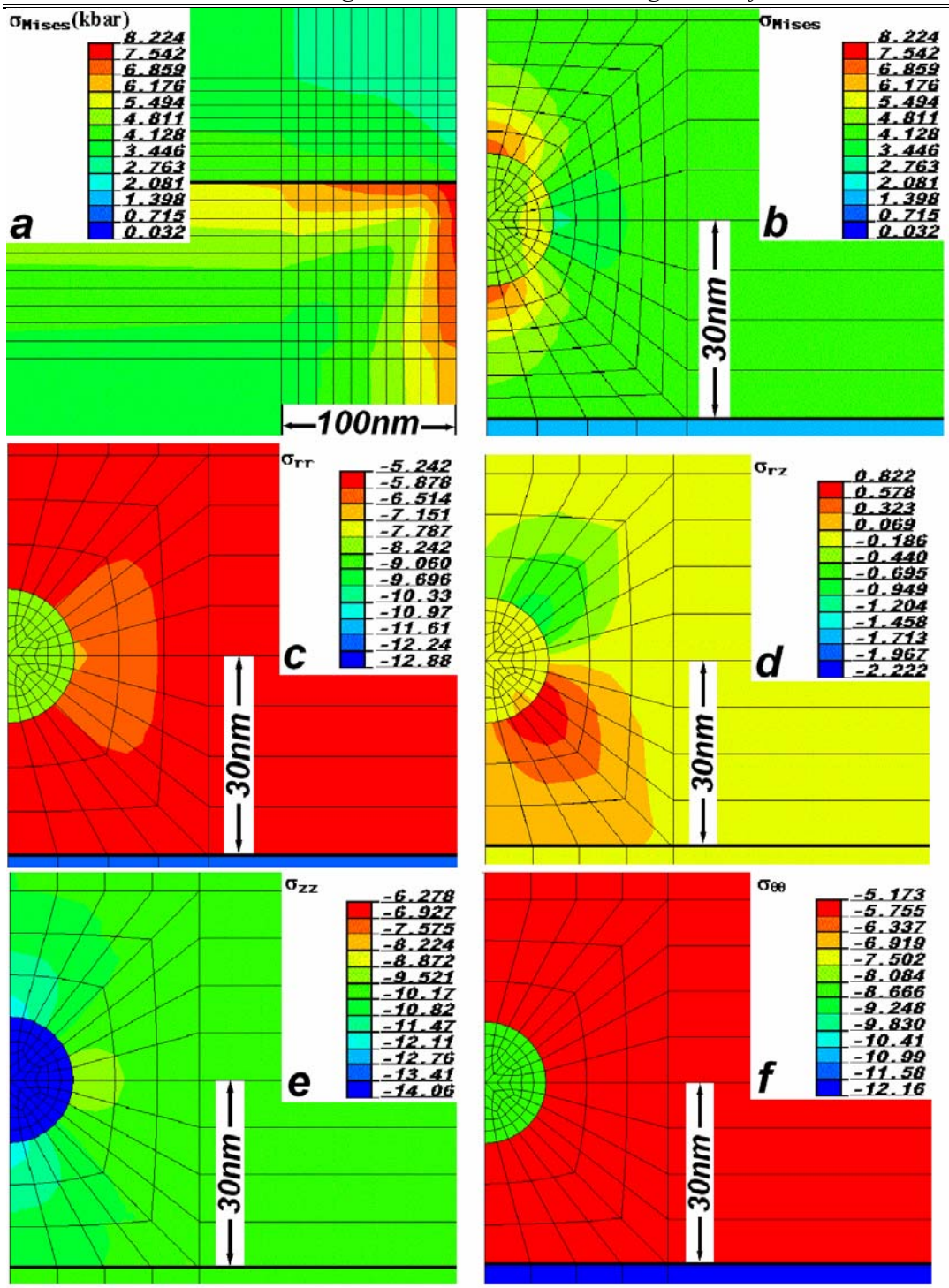

Figure 3.15. Local r - z plane stress distribution of σ_{Mises} (a) near the outer SiO_2/Si interface edge (the enlarged circle part in the Fig.3.13); and of σ_{Mises} (b), σ_{rr} (c), σ_{rz} (d), σ_{zz} (e), and $\sigma_{\theta\theta}$ (f) around a Ge nc, where the thin sold lines indicate the meshes used in the calculation while the thicker line indicates the SiO_2/Si interface.

From the above discussions, the high pressure Raman results on the $Ge/SiO_2/Si$ nanosystem can be explained by its nonhomogeneous distribution of the elastic field under pressure due to the specific geometric configuration of different parts with different elastic constants. The transition at 23 kbar can be ascribed to the delaminating of the SiO_2/Si interface as a result of the accumulated strain energy. Accordingly, the Raman shift of the Ge-Ge mode and Si-Si mode with pressure can be easily understood. Before the transition, $\alpha = 0.57 cm^{-1} kbar^{-1}$ of the Si-Si mode in the first upstroke of the pressure cycle can be ascribed to the more compressive σ_{rr} and $\sigma_{\theta\theta}$ introduced by the SiO_2/Si interface. After the delaminating, since the interface stress is released, the Si mode shifts down by 0.3 cm^{-1} and $\alpha = 0.53 cm^{-1} kbar^{-1}$ recovers to almost the bulk value[14]. On the other hand, before the transition, $\alpha = 0.42 cm^{-1} kbar^{-1}$ of Ge-Ge mode is due to more local tensile σ_{rr} and $\sigma_{\theta\theta}$ in the SiO_2 matrix introduced by the SiO_2/Si interface. After the delaminating, as the interface stress is released, without the shielding from the Si substrate, the Ge-Ge modes shifts to higher wavenumber by 3.4 cm^{-1} and α changes to $0.64 cm^{-1} kbar^{-1}$ thereafter. Since the delaminating is irreversible, the second pressure cycle (second upstroke and second downstroke) shows that both the Ge-Ge and Si modes keeping the same α as the first downstroke of pressure cycle. Moreover, due to the fact that the Ge nc's are distributed in the very thin SiO_2 matrix layer of ~ 1 μm, the stress concentration of σ_{rr}, σ_{zz}, and $\sigma_{\theta\theta}$ on the Ge nc's is relatively smaller than that on the Ge nc's embedded deep in SiO_2 matrix on quartz substrate as discussed in next paragraph, thus α $(= 0.64 cm^{-1} kbar^{-1})$ in $Ge/SiO_2/Si$ nanosystem is still smaller than that of the Ge/SiO_2/quartz nanosystem ($\alpha = 0.77 cm^{-1} kbar^{-1}$)[16].

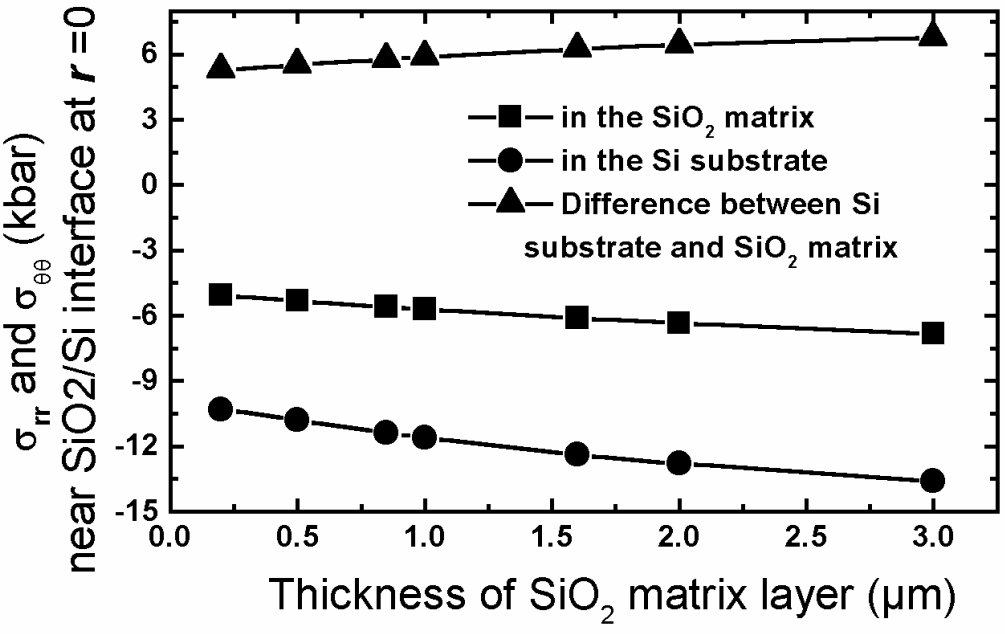

Figure 3.16. Calculated σ_{rr} and $\sigma_{\theta\theta}$ near the SiO_2/Si interface at r =0 as a function of the thickness of the SiO_2 matrix layer.

We also calculated the dependence of σ_{rr} and $\sigma_{\theta\theta}$ on the thickness of the SiO_2 matrix layer, where the axisymmetric model structure as shown in Fig. 3.13 was still used but with the thickness of the SiO_2 layer varied from 0.2 μm to 3.0 μm. The calculated σ_{rr} and $\sigma_{\theta\theta}$ near the SiO_2/Si interface around the central rotation axis, i.e. $r = 0$, as a function of the thickness of the SiO_2 matrix layer are shown in Fig. 3.16. The results indicate that as the thickness of the SiO_2 matrix layer increases, the stress concentration of σ_{rr} and $\sigma_{\theta\theta}$ in the Si substrate becomes stronger and the difference between the two sides of the SiO_2/Si interface also becomes bigger. Therefore, more strain energy would accumulate around the SiO_2/Si interface. Thus, in the nanosystem,

under the same pressure, the delaminating will occur more easily for thicker SiO_2 matrix layer as compared in the nanosystem with a thinner SiO_2 matrix.

In addition, our model can explain the seemingly confusing results for the high pressure PL measurement on the $Si/SiO_2/Si$ nanosystem in the literature[54]. In that experiment, a step change of PL peak shift with pressure around 12 kbar was observed in the first pressure cycle only on the sample B (with the SiO_2 layer thickness of 1.6 μm), but not in the sample A (with the SiO_2 layer thickness of 0.83 μm). Moreover, the observed pressure coefficient of the PL peak energy of Si nc's samples A and B, has different values of -0.4 and -0.6 meV/kbar respectively. According to our calculated results, more strain energy would accumulate at the SiO_2/Si interface in the nanosystem. Thus, under the same pressure the interface delaminating is apt to take place with the thicker SiO_2 matrix layer that with the thinner one. Hence, on the $Si/SiO_2/Si$ nanosystem, the considerable hysteresis (delaminating) around 12 kbar was observed in the first pressure cycle only on the sample B, but not in the sample A. This is also consistent with our observation of the delaminating of the SiO_2/Si interface at 23 kbar on $Ge/SiO_2/Si$ nanosystem, with the SiO_2 layer thickness of 1.0 μm. The larger pressure coefficients (-0.6 meV/kbar) of the PL peak energy observed on the sample B in the second pressure cycle than that (-0.4 meV/kbar) of sample A can be ascribed to that after the SiO_2/Si interface delaminating in the sample B since the Si nc's experience more compressive stress without the shielding of the Si substrate.

3.5 Conclusions

Ge nc's embedded in SiO_2 were investigated by Raman scattering under hydrostatic pressure. A large pressure coefficient for the Ge-Ge mode in Ge nc's as compared to its corresponding bulk value was found. The observed effect can be

explained in terms of a simple elastic model, which describes the significant contribution of the interface stress when subject to applied pressure. Thus the pressure acting on the nc's is not necessarily the same as the applied pressure. Furthermore, we also investigated the $Ge/SiO_2/Si$ nanosystem by high pressure Raman scattering. We found that the delaminating of SiO_2 film from the Si substrate occurs at ~23 kbar due to the large difference between the compressibility of the SiO_2 matrix and Si substrate. The observed effect can be understood by the nonhomogeneous distribution of the elastic field in the $Ge/SiO_2/Si$ nanosystem. Moreover, the previous unexplained high pressure PL results on the $Si/SiO_2/Si$ nanosystem can be explained by the nonuniform distribution of the elastic field. Although our investigation focuses on the $Ge/SiO_2/Si$ nanosystem, our results could provide a general understanding on the elastic properties of different multi-component nanosystems.

References

1 A. Meldrum, R. F. Haglund, Jr., L. A. Boatner, and C. W. White, Adv. Mater. 13, 1431(2001).

2 S. Sugano and H. Koizumi, in *Microcluster physics*, (2nd edn, Springer-Verlag, 1998), p.1.

3 K. H. Meiwes-Broer, in *Metal clusters at surfaces: structure, quantum properties, physical chemistry*, (New York: Springer, 2000), p.1.

4 H. J. Freund, Surf. Sci. **500**, 271(2002).

5 Z. L. Wang, J. Chem. Phys. B **104**, 1153 (2000).

6 H. -Ch. Weissker, J. Furthmller, and F. Bechstedt, Phys. Rev. B **65**, 155327 (2002).

7 A. D. Yoffe, Advances in Physics, **51**, 799(2002).

8 A. D. Yoffe, Advances in Physics, **50**, 1(2001).

9 G. P. Banfi, V. Degiorgio, D. Ricard, Advances in Physics, **47**, 447(1998).

10 W. G. van der Wiel, S. De Franceschi, J. M. Elzerman, T. Fujisawa, S. Tarucha, L. P. Kouwenhoven, Rev. Mod. Phys. **75**, 1(2003).

11 S. M. Reimann, M. Manninen, Rev. Mod. Phys. **74**, 1283(2002).

12 Z. I. Alferov, Rev. Mod. Phys. **73**, 767(2001).

13 Y. Alhassid, Rev. Mod. Phys. **72**, 895(2000).

14 V. L. Colvin, M. C. Schlamp, A. P. Alivisatos, Nature **370**, 354(1994).

15 D. L. Klein, R. Roth. A. K. L. Lim, A. P. Alivisatos, P. L. McEucn. Nature **389**, 699(1997).

16 J. Tersoff, C. Teichert, M. G. Lagally, Phys. Rev. Lett. **76**, 1675(1996).

17 D. Bimberg, Semiconductors **33**, 951(1999).

18 L. Guo, E. Leobandung, S. Y. Chou, Appl. Phys. Lett. 70, 850(1997).

19 S. Coffa, E. Castagna, C. Bongiorno, D. Patti, Nucl. Instrum. Methods. L. A. Gea, J. D. Budai, L. A. Boatner, J. Matter. Res. 14, 2602(1999).

20 Y. Maeda, Phys. Rev. B 51, 1658 (1995).

21 S. Takeoka, M. Fujii, S. Hayashi, and K. Yamamoto, Phys. Rev. B 58, 7921(1998).

22 S. Banerjee, S. Nozaki, and H. Morisaki, Appl. Phys. Lett. 76. 445 (2000).

23 L. Pavesi, L. Dal Negro, C. Mazzoleni, G. Franzò, and F. Priolo, Nature (London) 408, 440 (2000).

24 G. Wedler, J. Walz, T. Hesjedal, E. Chilla, and R. Koch, Phys. Rev. Lett. 80, 2382 (1998).

25 D. Gammon, in *Raman scattering in Materials Science*, edited by W. H. Weber, and R. Merlin (Spinger, New York, 2000), p.109.

26 L. Qin, *RAMAN STUDY OF Ge/Si QDs NANO STRUCTURES UNDER HIGH HYDROSTATIC PRESSURE*, Thesis (Ph.D.)--Dept. of Physics, Faculty of Science, National University of Singapore, 2002.

27 A. Jayaraman, Rev. Mod. Phys., Vol. 55, 65 (1983).

28 G. J. Piermarini, S. Block, J. D. Barnett, J. Appl. Phys. 44, 5377 (1973).

29 C. Carlone, N. K. Hota, H. J. Stolz, M. Elbert and H. D. Hochheimer, J. Chem. Phys. 75, 3220 (1981).

30 R. A. Forman, G. J. Piermarini, J. D. Barnett, and S. Block, Science 176, 284 (1972).

31 J. D. Barnett, S. Block, and G. J. Piermarini, Rev. Sci. Instrum. 44, 1 (1973).

32 G. J. Piemarini, S. Block, J. D. Barnett, and R. A. Forman, J. Appl. Phys. 46, 2774(1975).

33 G. J. Piermarini, S. Block, and J. D. Barnett, Rev. Sci. Instrum. 46, 973 (1975)

34 R. A. Forman, G. J. Piermarini, J. D. Barnett, and S. Block, Science 176, 284 (1972).

35 Y. Maeda, Phys. Rev. B 51, 1658 (1995).

36 S. Takeoka, M. Fujii, S. Hayashi, and K. Yamamoto, Phys. Rev. B 58, 7921 (1998).

37 S. Banerjee, S. Nozaki, and H. Morisaki, Appl. Phys. Lett. 76. 445 (2000).

38 L. Pasvesi, L. Dal Negro, C. Mazzoleni, G. Frano, and F. Priolo, Nature (London) 408, 440 (2000).

39 V. Craciun, I. W. Boyd, A. H. Reader, and E. W. Vandenhoudt, Appl. Phys. Lett. 65, 3233 (1994).

40 K. L. Teo, S. H. Kwok, P. Y. Yu, and S. Guha, Phys. Rev. B 62, 1584 (2000).

41 J. K. Shen, X. L. Wu, C. Tan, R. K. Yuan, and X. M. Bao, Phys. Lett. A 300, 307 (2002).

42 K. L. Teo, L. Qin, Z. X. Shen and O. G. Shmidt, Appl. Phys. Lett. 80, 1 (2002).

43 L. Qin, K. L. Teo, Z. X. Shen, C. S. Peng, and J. M. Zhou, Phys. Rev. B 64, 075 312 (2001).

44 R. S. Williams, G. Medeiros-Ribeiro, T. I. Kamins, and D. A. A. Ohlbergy, Annu. Rev. Phys. Chem. 51, 527(2000).

45 S. A. Chaparro, J. Drucker, Y. Zhang, D. Chandrasekhar, M. R. McCartney, and D. J. Smith, Phys. Rev. Lett. 83, 1199 (1999).

46 C. P. Liu, J. M. Gibson, D. G. Cahill, T. I. Kamins, D. P. Basile, and R. S. Williams, Phys. Rev. Lett. 84, 1958 (2000).

47 E. Anastassakis and M. Cardona, in Semiconductor Physics and Semimetals, edited by T. Suski and W. Paul (Academic, New York, 1998), Vol. 55, p. 118; A. R. Goni and K. Syassen, ibid. vol. 54, p. 247.

48 Z. F. Sui, I. P. Herman and J. Bevk, Appl. Phys. Lett. 58, 2351 (1991); Z. F. Sui, H. H. Burke and P. Herman, Phys. Rev. B 48, 2162 (1993).

49 M. Seon, M. Holtz, Ta-Ryeong Park, O. Brafman, and J. C. Bean, Phys. Rev. B 58, 4779 (1998).

50 M. Haselhoff, K. Reimann, and H. -J. Weber, Eur. Phys. J. B 12, 147(1999).

51 L. D. Landau, E. M. Lifschitz, Theory of Elasticity, 2nd edn. (Pergamon Press Ltd., London, 1970).

52 H Ledbetter and S. Kim, in Handbook of elastic properties of solids, liquids, and gases, Volume II, edited by M. Levy, H. E. Bass, R. R. Stern, M. Levy, L. Furr, and V. Keppens (San Diego : Academic Press, 2001), p. 99 and p. 100.

53 L. Duffrène and J. Kieffer, in Properties, processing and applications of glass and rare earth-doped glasses for optical fibres, edited by D. Hewak (London: IEE : INSPEC, 1998), p. 29.

54 H. M Cheong, W. Paul, S. P. Withrow, J. G. Zhu, J. D. Budai, C. W. White, and D. M. Hembree, Jr., Appl. Phys. Lett. 68, 87 (1996).

55 L. Liu, Z. X. Shen, K. L. Teo, A. V. Kolobov, and Y. Maeda, J. Appl. Phys. 93, 9392 (2003).

56 S. H. Tolbert and A. P. Alivisatos, Annu. Rev. Phys. Chem. 46, 595 (1995).

57 A. V. Kolobov, S. Q. Wei, W. S. Yan, H. Oyanagi, Y. Maeda, and K. Tanaka, Phys. Rev. B 67, 195314 (2003).

58 A. Saxena, in *Nonlinear Fracture Mechanics for Engineers*, (CRC Press, Boca Raton, 1998), Chap. 2, p.27.

Chapter 4

First-Principles Calculation Methods

4.1 Introduction

In quantum mechanics, the properties of materials, such as the total energy and electron density, can be understood from first principles by solving the Schrödinger equation. First-principles calculations, also known as *ab initio* calculations, use fundamental physical laws and constants only, without empirical parameters. So far, first-principles calculations have been proven to be one of the most powerful tools for carrying out theoretical studies of the electronic and structural properties of materials.

Prediction of the electronic and geometric structure of a material requires calculation of the quantum-mechanical total energy of the system and subsequent minimization of that energy with respect to the electronic and nuclear coordinates. Because of the large difference in mass between the electrons and nuclei and the fact that the forces on the particles are the same, the electrons respond essentially instantaneously to the motion of the nuclei. Thus the nuclei can be treated adiabatically, leading to a separation of electronic and nuclear coordinates in the many-body wave function — the so-called Born-Oppenheimer approximation. This "adiabatic principle" reduces the many-body problem to the solution of the dynamics of the electrons in some frozen-in configuration of the nuclei. Even with this simplification, the many-body problem remains formidable. Further simplifications are necessary to allow total-energy calculations to be performed accurately and efficiently,

such as *density-functional* theory to model the electron-electron interactions, *pseudopotential* theory to model the electron-ion interactions, *supercells* to model systems with a periodic geometries, and *iterative minimization* techniques to relax the electronic coordinates.[1]

This Chapter introduces briefly the simplifications and approximations related to the first-principles *total-energy pseudopotential* calculations.

4.2 Adiabatic approximation

Since the nuclear mass M far exceeds electron mass m, we can naturally limit the analysis to a model for electron traveling in a fixed field of nuclei. In this approximation the electron wave function is determined by the instantaneous position of the nuclei, while the wave function of ions is determined by the averaged electron field.[2]

The stationary Schrödinger equation in a crystal can be written as:

$$\hat{H}\Psi = E\Psi \tag{4.1}$$

where $\hat{H}$ is the Hamiltonian operator (Hamiltonian) of the system, Ψ the wave function of the dynamic variables of all particles, and E the eigenstate energy of the system. To solve (4.1), we need to determine the Hamiltonian of the system. Assuming the crystal composed of N atomic nuclei or ion cores and n electrons of all the electrons or n itinerant electrons only, and using a nonrelativistic approximation that takes into account only the pairwise interparticle interactions, the Hamiltonian has the following coordinate representation:[2,3]

$$\hat{H} = -\sum_{i=1}^{N} \hbar^2 \Delta_i / 2M_i - \sum_{j=1}^{n} \hbar^2 \Delta_j / 2m_{el}$$

$$+\sum_{i,j=1}^{N,n} G\left(\vec{R}_i - \vec{r}_j\right) + \sum_{i<i'=1}^{N} V\left(\vec{R}_i - \vec{R}_{i'}\right) + \sum_{j,j'} W\left(\vec{r}_j - \vec{r}_{j'}\right) \tag{4.2}$$

i.e.

$$\hat{H} = -\sum_{\alpha} \frac{\hbar^2}{2M_\alpha} \nabla_\alpha^2 - \sum_i \frac{\hbar^2}{2m} \nabla_i^2 + \tfrac{1}{2} \sum_{i \neq j} \frac{e^2}{\left|\vec{r}_i - \vec{r}_j\right|} + \tfrac{1}{2} \sum_{\alpha \neq \beta} \frac{z_\alpha z_\beta e^2}{\left|\vec{R}_\alpha - \vec{R}_\beta\right|} - \sum_{i,\alpha} \frac{z_\alpha e^2}{\left|\vec{r}_i - \vec{R}_\alpha\right|} \tag{4.3}$$

Here M_α is nuclear mass, m is electron mass, $\vec{r}_i$ is the radius vector of the ith electron, $\vec{R}_\alpha$ is the radius vector of the αth nucleus, and z_α is the atomic number. Since we have separated nuclear and electron motion, we can write

$$\Psi_{cr}(\vec{r}, \vec{R}) = \Psi(\vec{r}, \vec{R}) \Phi(\vec{R}) \tag{4.4}$$

Substitution Eq. (4.4) into Eq. (4.1) we obtain two equations:

$$\hat{H}_e \Psi(\vec{r}, \vec{R}) = \varepsilon \Psi(\vec{r}, \vec{R}) \tag{4.5}$$

$$\hat{H}_{nu} \Phi(\vec{R}) = \varepsilon_{nu} \Phi(\vec{R}) \tag{4.6}$$

where

$$\hat{H}_e = -\sum_i \frac{\hbar^2}{2m} \nabla_i^2 + \tfrac{1}{2} \sum_{i \neq j} \frac{e^2}{\left|\vec{r}_i - \vec{r}_j\right|} - \sum_{i,\alpha} \frac{z_\alpha e^2}{\left|\vec{r}_i - \vec{R}_\alpha\right|} \tag{4.7}$$

$$\hat{H}_{nu} = -\sum_{\alpha} \frac{\hbar^2}{2M_\alpha} \nabla_\alpha^2 + \tfrac{1}{2} \sum_{\alpha \neq \beta} \frac{z_\alpha z_\beta e^2}{\left|\vec{R}_\alpha - \vec{R}_\beta\right|} \tag{4.8}$$

In Eq. (4.6), we neglect the term[2]

$$\sum_{\alpha} \frac{\hbar^2}{2M_\alpha} \left[\Phi \int d\bar{r} \Psi^* \nabla_\alpha^2 \Psi - 2\left(\nabla_\alpha \Phi \int d\bar{r} \Psi^* \nabla_\alpha \Psi \right) \right] \tag{4.9}$$

For this estimate, we premultiply by Φ^* and integrate with respect to the nuclear coordinates.[2] We obtain

$$\Delta\varepsilon = \sum_{\alpha} \frac{\hbar^2}{2M_\alpha} \int d\bar{r} \Psi^* \nabla_\alpha^2 \Psi + \sum_{\alpha} \frac{\hbar^2}{M_\alpha} \left(\int d\vec{R} \Phi^* \nabla_\alpha \Phi \int d\bar{r} \Psi^* \nabla_\alpha \Psi \right) \tag{4.10}$$

For the first term we have

$$\sum_{\alpha}\frac{\hbar^2}{2M_\alpha}\int d\bar{r}\Psi^*\nabla_\alpha^2\Psi=-\sum_{i,\alpha}\frac{m}{M_\alpha}\int d\bar{r}\Psi^*\left(-\frac{\hbar^2}{2m}\right)\Psi=-\sum_{i,\alpha}\frac{m}{M_\alpha}\langle T_i\rangle$$

where $\langle T_i\rangle$ is the average kinetic energy of a single electron. Thus

$$\sum_{\alpha}\frac{\hbar^2}{2M_\alpha}\int d\bar{r}\Psi^*\nabla_\alpha^2\Psi=-ZN\frac{m}{M}\langle T_i\rangle.$$

Since $m/M \sim 10^{-5}$, this term is neglected compared to ε.

The second term in Eq. (4.9) is estimated analogously:

$$\sum_{\alpha}\frac{\hbar^2}{M_\alpha}\left(\int d\bar{R}\Phi^*\nabla_\alpha\Phi\int d\bar{r}\Psi^*\nabla_\alpha\Psi\right)=-\frac{1}{M_\alpha}\left(\langle P_\alpha\rangle\langle P_i\rangle\right).$$

In thermodynamic equilibrium for the case of classical statistics we have

$$\left\langle\frac{P_i^2}{2m}\right\rangle=\left\langle\frac{P_\alpha^2}{2M_\alpha}\right\rangle$$

and

$$\langle P_e\rangle^2=\frac{8}{3\pi}\langle P_e^2\rangle.$$

Then

$$\langle P_e\rangle^2\sim\sqrt{\frac{m}{M}}\langle P_\alpha\rangle$$

and the second term in Eq. (4.9) is of the order of $\sqrt{m/M}$ of the total crystal energy.

Consequently, discarding both corrections in Eq. (4.6) induce an energy error of less than $\sqrt{m/M}$. The discarded terms characterize the internal nonadiabaticity of the system which is expressed as an effect of nuclear motion on their interaction with the electrons. Therefore, electron-phonon interactions are neglected in the electronic structure calculations of crystals from the very outset. Thermal motion can be accounted for only as a perturbation that sets up a specific electron state distribution.[2]

In this approximation, the Hamiltonian of the electronic subsystem is

$$\hat{H} = -\sum_{j=1}^{n} \hbar^2 \Delta_j / 2m_{el} + \sum_{i,j=1}^{N,n} G\left(\vec{R}_i - \vec{r}_j\right) + \sum_{j,j'} W\left(\vec{r}_j - \vec{r}_{j'}\right) \quad (4.11)$$

where $\vec{R}_i$ stands for the positions of fixed nuclei or cores, that is, the sources of the field action on the electrons. However, in this approximation the solution of the Schrödinger equation still meets with huge mathematical difficulties. The major difficulty lies in the third term in Eq. (4.11), which interrelates the electronic coordinates, does not allow a many-body problem to be reduced to a sum of one-particle problems.[3]

4.3 Hartree-Fock approximation

The most difficult problem in any electronic structure calculation is posed by the need to take account of the effects of the electron-electron interaction. Electrons repel each other due to the Coulomb interaction between their charges. The Coulomb energy of a system of electrons can be reduced by keeping the electrons spatially separated, but this has to balanced against the kinetic energy cost of deforming the electron wave functions in order to separate the electrons.[1]

The wave function of a many-electron system must be anti-symmetric under exchange of any two electrons because the electrons are fermions. The antisymmetry of the wave function produces a spatial separation between electrons that have the same spin and thus reduces the Coulomb energy of the electronic system. The reduction in the energy of the electronic system due to the anti-symmetry of the wave function is called the *exchange energy*. It is straightforward to include exchange in a total energy in a total energy calculation, and this is generally referred to as the *Hartree-Fock approximation*.[1-3]

The *Hartree-Fock approximation* is of variational nature. It consists in restricting the set $\{\Psi \in \mathcal{H},\ \|\Psi\| = 1\}$ on which the energy functional $\langle \Psi, \hat{H}\Psi \rangle$ is minimized to the set of Slater determinants, i.e. to the set of the wave functions Ψ of the form[4]

$$\Psi = \frac{1}{\sqrt{N!}} \det(\phi_i(x_i, \sigma_j)) \tag{4.12}$$

where the ϕ_i, which are called *molecular orbitals*, satisfy the orthonormality conditions

$$\sum_{\sigma} \int_{R^3} \phi_i(x,\sigma) \phi_j(x,\sigma)^* \, dx = \delta_{i.j} \tag{4.13}$$

For of the electronic subsystem of the Hamiltonian of Eq. 3.7, the functional $\langle \psi | \hat{H} | \psi \rangle$ is given:[5]

$$\langle \psi | \hat{H} | \psi \rangle = \sum_{v} \int dq \, \phi_v^*(q) \hat{H}_0 \phi_v(q)$$

$$+ \frac{e^2}{2} \sum_{vv'} dq dq' \, \phi_v^*(q) \phi_{v'}^* |\vec{r} - \vec{r}'|^{-1} [\phi_v(q)\phi_{v'}(q) - \phi_v(q')\phi_{v'}(q)] \tag{4.14}$$

where $q = (\vec{r}\sigma)$, $\hat{H}_0 = -\sum_i \frac{\hbar^2}{2m} \nabla_i^2 - \sum_{i,\alpha} \frac{z_\alpha e^2}{|\vec{r}_i - \vec{R}_\alpha|} = -\frac{\hbar^2}{2m} \Delta + V_n(\vec{r})$.

Taking into account Eq. (4.13), we solve the variational problem

$$\frac{\delta}{\delta \phi_v^*(q)} \left[\langle \psi | \hat{H} | \psi \rangle - \sum_{v'v} \lambda_{vv'} \int dq \, \phi_v^*(q) \phi_{v'}(q) \right] = 0 \tag{4.15}$$

With allowance for Eq. (4.14), and carrying our the variation, we obtain[5]

$$\left[-\frac{\hbar^2}{2m} \Delta + V_n(\vec{r}) + e^2 \int d\vec{r}' \frac{\rho(\vec{r}')}{|\vec{r} - \vec{r}'|} \right] \phi_{is}(\vec{r}\sigma) - e^2 \sum_{js'\sigma'} \int d\vec{r}' \, \phi_{js'}^*(\vec{r}'\sigma') \phi_{is}(\vec{r}'\sigma') |\vec{r} - \vec{r}'|^{-1} \phi_{is}(\vec{r}\sigma)$$

$$= \sum_{js'} \lambda_{is,js'} \phi_{js'}(\vec{r}\sigma) \tag{4.16}$$

Here $is = v, js' = v'$, where i, j are orbital quantum numbers, and s, s' spin quantum numbers, and

$$\rho(\vec{r}) = \sum_{js\sigma} \left|\phi_{js}(\vec{r}\sigma)\right|^2 \tag{4.17}$$

is the total electron density at point $\vec{r}$.

After the unitary transformation of the functions $\phi_{is}(\vec{r}\sigma)$, we have *Hartree-Fock* equation:

$$\left[-\frac{\hbar^2}{2m}\Delta + V_n(\vec{r}) + e^2\int d\vec{r}'\frac{\rho(\vec{r}')}{|\vec{r}-\vec{r}'|}\right]\phi_{is}(\vec{r}\sigma) - e^2\sum_{js'\sigma'}\int d\vec{r}'\phi^*_{js'}(\vec{r}'\sigma')\phi_{is}(\vec{r}'\sigma')|\vec{r}-\vec{r}'|^{-1}\phi_{is}(\vec{r}\sigma)$$

$$= \varepsilon_{is}\phi_{is}(\vec{r}\sigma) \tag{4.18}$$

The third term enclosed in square brackets is a Coulomb potential, which is produced by all the other electrons acting on a given electron. The last term on the left-hand side of Eq. (4.18), called the exchange interaction, is due to the Pauli exclusion principle and is of a purely quantum origin.[5]

The Coulomb energy of the electronic system can be reduced below its Hartree-Fock value if electrons that have opposite spins are also spatially separated. In this case the Coulomb energy of the electronic system is reduced at the cost of increasing the kinetic energy of the electrons. The difference between the many-body energy of an electronic system and the energy of the system calculated in the Hatree-Fock approximation is called the correlation energy. The Hartree-Fock method has found broad application in atomic theory, but has only limited suitability for the majority applications to condensed matter. For condensed matter theory the area of special interest concerns low density valence electrons for which correlations of electrons with antiparallel spins, neglected in Hartree-Fock method, yield effects of the same order as exchange.[1-5]

4.4 Density-Functional Theory

Density-functional theory (DFT), developed by Hohenberg and Kohn (1964) and Kohn and Sham (1965), provided some hope of a simple method for describing the effects of exchange and correlation in an electron gas. Hohenberg and Kohn proved that the total energy, including exchange and correlation, of an electron gas (even in the presence of a static external potential) is a unique functional of the electron density. The minimum value of the total-energy functional is the ground-state energy of the system, and the density that yields this minimum value is the exact single-particle ground-state density.[1]

E. Bright Wilson suggested (1965) that a knowledge of the density was all that was necessary for a complete determination of all molecular properties. If N is the number of electrons then $\rho(\vec{r})$ is defined by[6]

$$\rho(\vec{r}) = N\int\cdots\int|\Psi|^2 d\vec{x}_1 d\vec{x}_2 \ldots d\vec{x}_N \tag{4.19}$$

where $\Psi(\vec{x}_1\vec{x}_2\ldots\vec{x}_N)$ is the electronic wavefunction of the molecule. Wilson's observations were that

$$\int \rho(\vec{r})d\vec{r} = N \tag{4.20}$$

and the nuclear cusp condition

$$\frac{\partial}{\partial r_A}\overline{\rho}(r_A)\bigg|_{r_A=0} = -2Z_A\overline{\rho}(0) \tag{4.21}$$

where $\overline{\rho}(r_A)$ is the spherical average of $\rho(\vec{r})$. Hence the full Schrödinger Hamiltonian is known, because it is completely defined once the position and charge of the nuclei are given. Therefore, in principle, the wavefunction and energy are known, and thus everything is known.[6,7]

In 1964, Hohenberg and Kohn proposed two theorems for a system of N interacting electrons in a non-degenerate ground state associated with an external potential $v(\vec{r})$.[1,6,7]

Hohenberg-Kohn theorem 1. The ground state electron density $\rho(\vec{r})$ uniquely determines the external potential $v(\vec{r})$ due to the nuclei.

We may therefore represent the energy of the system as a functional of the density as follows[6]

$$E(\rho) = V_{ne}[\rho] + T[\rho] + V_{ee}[\rho] \tag{4.22}$$

$$= \int \rho(\vec{r}) v(\vec{r}) d\vec{r} + T[\rho] + V_{ee}[\rho] \tag{4.23}$$

where $T[\rho]$ is the kinetic energy and $V_{ee}[\rho]$ is the electron-electron interaction energy which contains the Coulomb interactions $J[\rho]$ which is given by:

$$J[\rho] = \frac{1}{2} \int\int \frac{1}{\vec{r}_{12}} \rho(\vec{r}_1) \rho(\vec{r}_2) d\vec{r}_1 d\vec{r}_2 \tag{4.24}$$

Hohenberg-Kohn theorem 2. For any approximation density $\tilde{\rho}$, $E[\tilde{\rho}] \geq E[\rho]$, where ρ is the exact density.

The second Hohenberg-Kohn theorem allows us to introduce the variational principle. This variational principle allows us to write down the condition that the energy, Eq. (4.22), is stationary with respect to changes in the density, subject to the constraint that Eq. (4.20) holds:[6]

$$\delta E[\rho] - \mu \delta \left| \int \rho(\vec{r}) d\vec{r} - N \right| = 0 \tag{4.25}$$

for which the Euler-Lagrange equation is, in terms of functional derivatives

$$\mu = v(r) + \frac{\delta T[\rho]}{\delta \rho(\vec{r})} + \frac{\delta V_{ee}[\rho]}{\delta [\vec{r}]} \tag{4.26}$$

This last equation is an exact equation for $\rho(\vec{r})$, if only we knew the functional forms of $T[\rho]$ and $V_{ee}[\rho]$. We now go on to convert this equation into a set of working equation. Kohn and Sham introduced the idea of considering the determinantal wavefunction for *N* noninteracting electrons in *N* orbitals ϕ_i. For such a system the kinetic energy and the electron density are exactly given by[6]

$$T_s[\rho] = \sum_i^N \left\langle \phi_i \left| -\frac{1}{2}\nabla^2 \right| \phi_i \right\rangle \tag{4.27}$$

$$\rho(\vec{r}) = \sum_i^N |\phi_i(\vec{r})|^2 \tag{4.28}$$

The orbitals obey an equation of the form

$$\left[-\frac{1}{2}\nabla^2 + v_s(\vec{r}) \right] \phi_i = \varepsilon_i \phi_i \tag{4.29}$$

and the energy of this system is given by

$$E[\rho] = T_s[\rho] + \int v_s(\vec{r})\rho(\vec{r})d\vec{r} \tag{4.30}$$

Equations (4.29) are the Euler equations obtained when $E[\rho]$ is minimized with respect to variations in the orbitals which constitute the density as given by Eq. (4.28) subject to the constraint that they remain normalized.[6]

Now we return to the problem with interacting electrons and we write the energy in different ways:[6]

$$\begin{aligned} E[\rho] &= \int v(\vec{r})\rho(\vec{r})d\vec{r} + T[\rho] + V_{ee}[\rho] \\ &= \int v(\vec{r})\rho(\vec{r})d\vec{r} + T_s[\rho] + J[\rho] + (T[\rho] - T_s[\rho] + V_{ee}[\rho] - J[\rho]) \\ &= \int v(\vec{r})\rho(\vec{r})d\vec{r} + T_s[\rho] + J[\rho] + E_{xc}[\rho] \end{aligned} \tag{4.31}$$

The first line is from Eq. (4.22), the second line inserts and removes the noninteracting kinetic energy and the Coulomb energy, the next line introduces the exchange-

correlation energy functional the functional derivative of which is the exchange-correlation potential v_{xc}:

$$E_{xc}[\rho] = T[\rho] - T_s[\rho] + V_{ee}[\rho] - J[\rho] \tag{4.32}$$

$$v_{xc}(\vec{r}) = \frac{\delta E_{xc}[\rho]}{\delta \rho(\vec{r})} \tag{4.33}$$

On comparing equations (4.29), (4.31), and (4.33) we deduce that the problem has been recast into one involving noninteracting electrons in N orbitals which obey the equation

$$\left[-\frac{1}{2}\nabla^2 + v_s(\vec{r}) + \int \frac{\rho(\vec{r}')}{\vec{r} - \vec{r}'} dr' + v_{xc}(\vec{r}) \right] \phi_i = \varepsilon_i \phi_i \tag{4.34}$$

These are the Kohn-Sham equations for the Kohn-Sham orbitals ϕ_i. Note that the key property of them is that they give the exact density through Eq. (4.28), once the exact exchange-correlation functional $E_{xc}[\rho]$ has been determined.[6]

The Kohn-Sham equations represent a mapping of the interacting many-electron system onto a system of noninteracting electrons moving in an effective potential due to all the other electrons. If the exchange-correlation energy functional were known exactly, then taking the functional derivative with respect to the density would produce an exchange-correlation potential that included the effects of exchange and correlation exactly. The Kohn-Sham equations must be solved self-consistently so that the occupied electronic states generate a charge density that produces the electronic potential that was used to construct the equations.[1,2,6,7]

4.5 Local-density approximation

The Kohn-Sham scheme does not lead to computational power as it stands, because the difficulty of the many-body problems is still present in the unknown

functional $E_{xc}[\rho]$. To overcome this, Kohn and Sham proposed a *local density approximation* (LDA)[8]

$$E_{xc}[\rho(\vec{r})] \approx E_{xc}^{LDA} = \int \rho(\vec{r}) \varepsilon_{xc}^{\text{hom}}(\rho(\vec{r})) d\vec{r} \tag{4.35}$$

in which $\varepsilon_{xc}^{\text{hom}}$ is the exchange-correlation energy per particle in the homogeneous (spatially uniform) electron gas. The functional derivative of E_{xc}^{LDA} is the local approximation to the Kohn-Sham exchange-correlation potential:

$$v_{xc}^{LDA}(\vec{r}) = \frac{\delta E_{xc}^{LDA}}{\delta \rho(\vec{r})} = \left. \frac{d[\rho \varepsilon_{xc}^{LDA}(\rho)]}{d\rho} \right|_{n=n(\vec{r})} \tag{4.36}$$

The *homogeneous electron gas* model is a fictitious system, used as a reference in DFT calculations.[2,5-8] It is defined as a large number N of electrons in a cube of volume $V = l^3$, throughout which there is uniformly spread of a positive charge sufficient to make the system neutral. The uniform electron gas corresponds to the limit $N \to \infty$, $V \to \infty$, with the density $\rho = N/V$ remaining finite. The ground state energy is

$$E[\rho] = \int v(\vec{r}) \rho(\vec{r}) d\vec{r} + T_s[\rho] + J[\rho] + E_{xc}[\rho] + E_b \tag{4.37}$$

with E_b being the electrostatic energy of the positive background, which is equal to the coulomb energy because the positive charge density $n(\vec{r})$ is simply the negative of $\rho(\vec{r})$. Because the external potential is defined by

$$v(\vec{r}) = -\int \frac{n(\vec{r}')}{|\vec{r} - \vec{r}'|} d\vec{r}' \tag{4.38}$$

it follows that the second, third and fifth terms of Eq. (4.37) add to zero, and therefore

$$E[\rho] = T_s[\rho] + E_{xc}[\rho] \tag{4.39}$$

$$= T_s[\rho] + E_x[\rho] + E_c[\rho] \tag{4.40}$$

where the exchange-correlation term is split into an exchange term plus a correlation term.[2,5-8]

The Kohn-Shams are satisfied by plane wave

$$\phi_k(\vec{r}) = \frac{1}{V^{1/2}} \exp(i\vec{k} \cdot \vec{r}) \tag{4.41}$$

where periodic boundary conditions require

$$k_x = \frac{2\pi}{l} n_x,\ k_y = \frac{2\pi}{l} n_y,\ k_z = \frac{2\pi}{l} n_z,\ n_x,\ n_y,\ n_z = 0,\pm 1,\pm 2,\ldots \tag{4.42}$$

In the Hartree-Fock approximation, the exchange energy is

$$K = -\frac{1}{4} \iint \frac{|\rho_1(\vec{r}_1, \vec{r}_2)|^2}{|\vec{r}_1 - \vec{r}_2|} d\vec{r}_1 d\vec{r}_2 \tag{4.43}$$

where $\rho_1(\vec{r}_1, \vec{r}_2) = 2\sum_i \phi_i(\vec{r}_1)\phi_i(\vec{r}_2)$ is the one particle density matrix. For the uniform electron gas, this can be exactly evaluated, and the result is that the exchange energy is

$$E_x[\rho] = -C_x \int \rho(\vec{r})^{4/3} d\vec{r} \tag{4.44}$$

where $C_x = \frac{3}{4}(3\pi^{-1})^{1/3} = 0.7386$. It is usual to introduce the exchange energy per particle ε_x as a function of r_s, the radius of a sphere whose volume is the effective volume of an electron

$$\frac{4}{3}\pi r_s^3 = \frac{1}{\rho} \tag{4.45}$$

$$E_x[\rho] = \int \rho(\vec{r}) \varepsilon_x(r_s) d\vec{r} \tag{4.46}$$

$$\varepsilon_x(r_s) = -\frac{0.4582}{r_s} \tag{4.47}$$

The correlation energy cannot be found exactly even for the homogeneous egas. Ceperley and Alder gave the near-exact numerical simulation result, using the quantum Monte-carlo method for several different values of r_s.[6] Also using analytic

information for the high and the low density limit, Vosko, Wilk and Nusair[6] gave the following accepted form for $\varepsilon_c(\vec{r}_s)$ which covers both the spin polarized and spin compensated cases

$$\varepsilon_c(\vec{r}_s) = \frac{A}{2}\left(\ln\frac{x^2}{X(x)} + \frac{b}{Q}\arctan\frac{Q}{2x+b}\right.$$

$$\left. - \frac{bx_0}{X(x_0)}\left[\ln\frac{(x-x_0)^2}{X(x)} + \frac{2(b+2x_0)}{Q}\arctan\frac{Q}{2x+b}\right]\right) \qquad (4.48)$$

where $x = r_x^{1/2}$, $X(x) = x^2 + bx + c$, $Q = \left(4c - b^2\right)^{1/2}$, and A, x_0, B and c are prescribed constants.[2,5-8]

LDA assumes that the exchange-correlation energy functional is purely local, and, in principle, ignores correlations to the exchange-correlation energy at a point ***r*** due to nearby inhomogeneities in the electron density. Considering the inexact nature of the approximation, it is remarkable that calculations performed using the LDA have been so successful that it is almost universally used in total-energy pseudopotential calculations. Some work has shown that this success can be partially attributed to the fact that LDA gives the correct sum rule for the exchange-correlation hole. The LDA appears to give a single well-defined global minimum for the energy of a non-spin-polarized system of electrons in a fixed ionic potential. Therefore any energy minimization scheme will locate the global energy minimum of the electronic system.[1,2,5-8]

4.6 Bloch's Theorem and Plane Wave Basis Sets

Although certain observables of the many-body problem can be mapped into equivalent observables in an effective single-particle problem as in DFT-LDA, there still remains the formidable task of handling an infinite number of noninteracting

electrons moving in the static potential of an infinite number of nuclei or ions. Two difficulties must be overcome: a wave function must be calculated for each of the infinite number of electrons in the system, and the basis set required to expand each wave function is infinite since each electronic wave function extends over the entire solid. Both problems can be surmounted by performing calculations on periodic systems and applying *Bloch's theorem* to the electronic wave functions.[1]

For an ideal crystal of some symmetry and a single electron moving in a effect potential denoted by $V(\vec{r})$, the Schrödinger equation can be written as:[9-11]

$$\hat{H}\psi_i(\vec{r}) = \left(-\frac{\hbar^2}{2m}\nabla^2 + V(\vec{r})\right)\psi_i(\vec{r}) = \varepsilon_i\psi_i(\vec{r}) \tag{4.49}$$

where $\psi_i(\vec{r})$ is the wave function, ε_i the energy eigenvalue, and i the label for quantum number. The symmetry of the potential is the same as that of the crystal lattice, the most prominent aspect of which is translational periodicity, i.e.

$$V(\vec{r} + \vec{R}_j) = V(\vec{r}). \tag{4.50}$$

Here $\vec{R}_j$ is a lattice translation vector, customarily expressed by the three lattice primitive translation vectors $\vec{a}$, $\vec{b}$, and $\vec{c}$,

$$\vec{R}_j = l_j\vec{a} + m_j\vec{b} + n_j\vec{c} \tag{4.51}$$

where l_j, m_j, and n_j are integers.

Let us define the translation operators $\hat{T}_j$ for each lattice vector $\vec{R}_j$ which act in the following manner on any function of position $f(\vec{r})$:[9]

$$\hat{T}_j f(\vec{r}) = f(\vec{r} + \vec{R}) \tag{4.52}$$

The operators $\hat{T}_j$ obviously form a group and commute with each other, and commute with Hamiltonian, because of Eq. (4.50), that

$$\left[\hat{T}_j, \hat{H}\right] = 0 . \tag{4.53}$$

Accordingly the wave function $\psi_i(\vec{r})$ satisfies

$$\psi_i(\vec{r} + \vec{R}) = \exp(i\vec{k} \cdot \vec{R}_j)\psi_i(\vec{r}) \tag{4.54}$$

which is one statement of Bloch's theorem.

Bloch's theorem suggests that each electronic wave function in a solid can be the product of a cell-periodic part and a wavelike part[1]

$$\psi_i(\vec{r}) = \exp(i\vec{k} \cdot \vec{r}_j) f_i(\vec{r}) . \tag{4.55}$$

The cell-periodic part of the wave function can be expanded using a basis set consisting of a discrete set of plane waves whose wave vectors are reciprocal lattice vectors of the crystal,

$$f_i(\vec{r}) = \sum_{\vec{G}} c_{i,\vec{G}} \exp\left[i\vec{G} \cdot \vec{r}\right], \tag{4.56}$$

where the reciprocal lattice vectors $\vec{G}$ are defined by $\vec{G} \cdot \vec{R} = 2\pi m$ for all $\vec{R}$ where $\vec{R}$ is a lattice vector of the crystal and m is an integer. Therefore each electronic wave function can be written as a sum of plane waves,

$$\psi_i(\vec{r}) = \sum_{\vec{G}} c_{i,\vec{k}+\vec{G}} \exp\left(i\left(\vec{k} + \vec{G}\right) \cdot \vec{r}\right). \tag{4.57}$$

Bloch's theorem changes the problem of calculating an infinite number of electronic wave functions to one of calculating a finite number of electronic wave functions at an infinite number of **k** points. However, the electronic wave functions at **k** points that are very close together will be almost identical. Hence it is possible to represent the electronic wave functions at single **k** point. In this case the electronic states at only a finite number of **k** points are required to calculate the electronic potential and hence determine the total energy of the solid.[1]

Bloch's theorem states that the electronic wave functions at each **k** point can be expanded in terms of a discrete plane-wave basis set. Since the coefficients $c_{i,\vec{k}+\vec{G}}$ for the plane-waves with small kinetic energy $\left(\hbar^2/2m\right)\left|\vec{k}+\vec{G}\right|^2$ are typically more important than those with large kinetic energy, the plane-wave basis can be truncated to introduce only plane waves that have kinetic energies less than some particular cutoff energy. This kinetic energy cut-off will lead to an error in the total energy of the system but in principle it is possible to make this error arbitrarily small by increasing the size of the basis set by allowing a larger energy cut-off.[1]

Another advantage of expanding the electronic wavefunctions in terms of a basis set of plane waves is that the Kohn-Sham equations take a particularly simple form. Substitution of Equation (4.57) in to the Kohn-Sham equations, (4.34), gives

$$\sum_{\vec{G}'}\left[\frac{\hbar^2}{2m}\left|\vec{k}+\vec{G}\right|^2\delta_{\vec{G}\vec{G}'}+V_{ion}\left(\vec{G}-\vec{G}'\right)+V_H\left(\vec{G}-\vec{G}'\right)+V_{xc}\left(\vec{G}-\vec{G}'\right)\right]$$

$$c_{i,\vec{k}+\vec{G}}=\varepsilon_i c_{i,\vec{k}+\vec{G}} \tag{4.58}$$

In this form, the kinetic energy is diagonal, and the various potentials are described in terms of their Fourier transforms. Solution of Eq. (4.58) proceeds by diagonalization of the Hamiltonian matrix elements $H_{\vec{k}+\vec{G},\vec{k}+\vec{G}'}$ given by the term in the brackets above. The size of the matrix is determined by the choice of cutoff energy $\left(\hbar^2/2m\right)\left|\vec{k}+\vec{G}_c\right|^2$, and will be intractably large for systems that contain both valence and core electrons. This is a severe problem, but can be overcome by use of the pseudopotential approximation.[1]

4.7 Pseudopotential method

Although with *Bloch's theorem* the electronic wave functions can be expanded using a discrete set of plane waves, a plane wave basis set is usually very poorly suited to expanding the electronic wavefunctions because a very large number of plane waves are required to accurately describe the rapidly oscillating wavefunctions of electrons in the core region. An extremely large plane-wave basis set would be required to perform an all-electron calculation, and a vast amount of computational time would be required to calculate the electronic wave functions. The *pseudopotential approximation* allows the electronic wave functions to be expanded using a much smaller number of plane-wave basis states.[1,2]

It is well known that most physical properties of solids are dependent on the valence electrons to a much greater extent than on the core electrons. Thus, the core electron states may be assumed to be fixed, and a "pseudopotential" may be constructed for each atomic species which takes into account the effects of the nucleus and core electrons in an effective manner. The *pseudopotential approximation* exploits this by removing the core electrons and by replacing them and the strong ionic potential by a weaker pseudopotential that acts on a set of pseudo wave functions rather than the true valence wave functions. The pseudopotential theory applied by *Phillips* and *Kleinman* (who used the Herring OPW method) can help explain the basic idea of this approximation.[12-14]

We may represent the basis wave function as the orthogonalized plane wave[12]

$$\Psi = \Phi - \sum_c \langle \chi_c | \Phi \rangle \chi_c \tag{4.59}$$

where χ_c is the core wave function, and Φ is a certain smooth function usually represented as a plane wave. To obtain Φ, we can substitute Eq. (4.59) to the Schrödinger equation (4.1), thus we have

$$\hat{H}\Phi - \sum_c \langle \chi_c | \Phi \rangle \hat{H}\chi_c = E\Phi - E\sum_c \langle \chi_c | \Phi \rangle \chi_c \tag{4.60}$$

Since the core function χ_c is the eigenfunction of the Hamiltonian $\hat{H}$ corresponding to the eigenvalue E_c, the Eq. (4.60) becomes[12]

$$\hat{H}\Phi + \hat{V}_R\Phi = E\Phi \tag{4.61}$$

where the operator V_R is formally defined by

$$\hat{V}_R\Phi \equiv \sum_c (E - E_c)\langle \chi_c | \Phi \rangle \chi_c \tag{4.62}$$

Thus, the smooth pseudowave function Φ satisfies the Schrödinger equation

$$\left(-\nabla^2 + \hat{V}_p\right)\Phi = E\Phi \tag{4.63}$$

and the pseudopotential is

$$\hat{V}_p = \hat{V}(\vec{r}) + \hat{V}_R \tag{4.64}$$

While the attractive crystal potential $\hat{V}(\vec{r})$ is negative, the potential $\hat{V}_R(\vec{r})$ containing the difference $(E - E_c)$ is positive. These two potentials partially compensate for one another and decrease the value of $\hat{V}_p$. Hence comes an important property of the pseudopotential: it is a smoother function of coordinates that $\hat{V}(\vec{r})$ is, therefore, for it to be approximated by a Fourier series a small number of terms is sufficient. Accordingly, because $\hat{V}_p$ is small, we have for all practical purposes returned to the model of nearly free electrons, in which the main approximation is a small value of the potential.[12]

References

1 M. C. Payne, M. P. Teter, D. C. Allan, T.A. Arias and J. D. Joannopoulos, Reviews of modern physics, 64, 1045(1992); and references therein.

2 A. A. Katsnelson, V. S. Stepanyuk, A. I. Szász, and O. V. Farberovich, *Computational methods in condensed matter: electronic structure* (translated by Kevin Hendzel, New York: American Institute of Physics, 1992), p3, p33.

3 S. V. Vonsovskii, M. I. Katsnelson, *Quantum solid-state physics* (Berlin; New York: Springer-Verlag, 1989), p86, p330.

4 E. Cancès, *Mathematical models and methods for ab initio quantum chemistry* (edited by M. Defranceschi and C. Le Bris, New York: Springer, 2000), p17.

5 Eschrig, H. (Helmut), *The fundamentals of density functional theory* (Stuttgart; Leipzig: Teubner, 1996), p24.

6 N. C. Handy, *Quantum mechanical simulation methods for studying biological systems: Les Houches Workshop, May 2-7, 1995* (editors, Dominique Bicout, Martin Field, Berlin: Springer-Verlag, 1996), p1; and references therein.

7 W. Kohn, *Density functional theory* (edited by Eberhard K.U. Gross and Reiner M. Dreizler, New York: Plenum Press, 1995), p3.

8 J. F. Dobson and M. P. Das, *Electronic density functional theory: recent progress and new directions* (edited by John F. Dobson, Giovanni Vignale and Mukunda P. Das, New York: Plenum Press, 1998), p3.

9 J. Kübler, *Theory of itinerant electron magnetism* (Oxford: Clarendon Press; Oxford; New York: Oxford University Press, 2000), p78.

10 C. Kittel, *Introduction to solid state physics* (Sixth Edition, John Wiley & Sons, Inc., Singapore, 1986), p4, p163.

11 C. Hamaguchi, *Basic semiconductor physics* (New York : Springer, 2001), p3.

12 V.V. Nemoshkalenko, V.N. Antonov, *Computational methods in solid state physics* (Gordon and Breach Science Publishers, Amsterdam: 1998), p113.

13 N.P. Kovalenko, Y. P. Krasny, U. Krey, *Physics of amorphous metals* (Berlin; New York: Wiley-VCH, 2001), p15.

14 M. Fuchs, M. Scheffler, Computer Physics Communications. **119**, 67 (1999).

Chapter 5

Structural and electronic properties of *h*-BN

5.1 Introduction

Being one of the most interesting solids among the III-V compounds, boron nitride (BN) has motivated tremendous amount of theoretical and experimental investigations on its fundamental properties for a long time.[1-15] BN is also the basis for many advanced technologies.[16] Four different polymorphic modifications *i.e.* cubic *c*-BN, wurzite *w*-BN, hexagonal *h*-BN, and rhombohedral *r*-BN, have been found for BN which are responsible for the wide spectrum of properties of BN.[16] The two high density diamond-like phases, *c*-BN and *w*-BN, have tetrahedral sp^3 hybridized B-N bonds, but different stacking sequences of the BN basal layers. The *c*-BN consists of the three-layer (ABCABC…) stacking of the *c*-BN (111) planes while *w*-BN follows the two-layer (AA'AA'…) stacking sequence of *w*-BN (0002) planes which is structurally identical to the *c*-BN (111) planes.[16-18] The two low density graphite-like phases, *h*-BN and *r*-BN, consist of two-dimensional layers of hexagonally-linked sp^2 hybridized B-N bonds, arranged in the (aa'aa'…) and (abcabc…) orders, respectively.[16-18] In addition to the above, BN has been found to exist in partial or completely disordered phases. The turbostratic (*t*-BN)[18-21] phase has random stacking of the hexagonal sp^2 bonded BN basal layers and is a partially disordered phase, while

amorphous BN (*a*-BN) is characterized by atomic-level structural disorders.[18] The most common phase of boron nitride, *h*-BN, is known as a very good electrical insulator with good thermal conductivity and stability. It has been widely used in vacuum technology and also been employed in electronics, nuclear energy, X-ray lithography, lubrication, etc.[22,23]

Despite of the fact that *h*-BN is the best studied polymorph of BN, there has been no agreement on the basic electronic properties of *h*-BN to date. For example there is a wide range of values for its band gap energy.[22] Electronic states of *h*-BN have been studied by luminescence,[1,2,6,9,22,24] electron energy loss spectroscopy (EELS),[25-27] X-ray photoemission spectroscopy (XPS),[28,29] X-ray emission,[30,31] X-ray absorption,[12,32] resonant inelastic X-ray scattering,[33,34] optical absorption,[13,35,36,37] and reflectivity spectra,[4,38,39] and other techniques.[40,41] However, widely dispersed band gap energy values ranging from 3.6 eV to 7.1 eV can be found in the literature and both direct and indirect band gaps have been reported for *h*-BN. These results suggested that the band gap nature of *h*-BN can not be described only by either direct or indirect gap with a single value, although different experimental techniques may have different system errors which could disperse more or less the experimental band gap values.

Extensive theoretical studies have been performed on the electronic and optical properties of *h*-BN. However, the calculated band structures are dependent on the calculation methods. Using the tight-binding method, Robertson investigated the electronic structure and core excitation of *h*-BN and found a direct gap at the *H* point, but a very small *K-H* dispersion.[42] Calculation based on the full-potential self-consistent linearized augmented-plane-wave method by Catellani *et al*. showed that *h*-BN has a minimal indirect band gap of 3.9 eV between the valence-band maximum at

H and the conduction-band minimum at *M*, and a lowest direct band gap of 3.9 eV at H.[43] However, Park *et al*. found that the lowest direct gap of *h*-BN is located at *M*, with a gap value of 4.5 eV using the same method.[44] Results of band structure calculation based on the orthogonal linear combination of atomic orbitals (OLCAO) method by Xu and Ching suggest an indirect band gap (*H-M*) of 4.07 eV and a lowest direct band gap (*H*) of 4.2 eV.[45] Using pseudopotential approach, Furthmüller *et al.* predicted a direct gap of 4.5 eV at the *M* point, which is 0.4 eV larger than the indirect gap between the *M* and *H* points.[46]

While these studies provided certain degree of understanding to the electronic properties of *h*-BN, few of them directly addressed the conflicting experimental and theoretical values of the fundamental band gap of *h*-BN. Sample quality was often cited as the reason for the great variation in the electronic properties from sample to sample. Although many investigations on the electronic properties of *h*-BN, such as defects,[8,10,47,48] core hole effect,[33,34,49] and luminescence,[1,2,6,9,22,24] were carried out, it is difficult to give an accurate description without fully understanding the band structure of *h*-BN.

Unfortunately nearly all experimental analysis or theoretical calculations on *h*-BN were based on the hexagonal crystal structure first proposed by Pease,[50,51] as shown in Fig. 5.1 (A). In this crystal structure which has space group $P6_3/mmc$ (194), the hexagonal BN layers align in the *c*-direction in such a way that the hexagons reside directly above one another and the B atoms immediately above the N atoms or vice versa. However, for real *h*-BN crystals (*Z*=2), XRD data indicate that the crystal may exist in structures with different symmetries. In particular, *h*-BN structures with space groups $P6_3/mmc(194)$,[52] $P\bar{6}m2(187)$,[53,54] $P\bar{3}m1(164)$[55-57] and $P\bar{6}(174)$[58] respectively have been found. In fact, Geick *et al.* discussed their optical investigation data in terms

of two *h*-BN structures with different stacking sequences of the hexagonal BN layers in 1960's.[4] However, few theorists have paid attention to the stacking effects to the structural and electronic properties of *h*-BN since then, except a recent work by Mosuang and Lowther which indicated that slightly different phases of this material could exist in three forms of the AaAa… stacking.[59] Moreover, stacking disorder was found in pyrolytic boron nitride (PBN) formed by chemical vapor deposition and in the semi-crystalline BN phase, *t*-BN, where larger interlayer spacing was observed.[16,20] However, there has been no theoretical study on the structural or electronic properties of PBN and *t*-BN. Therefore, it would be interesting to investigate the structural stability of *h*-BN related to the stacking behavior of hexagonal basal layers. It could elucidate the uncertainty of the band structure of *h*-BN observed experimentally, and provide further understanding on the electronic properties of PBN and *t*-BN.

This chapter aims to provide a clear understanding of the structural and electronic properties of *h*-BN, as well as those of PBN and *t*-BN. A systematic investigation on structural and electronic properties of *h*-BN related to stacking of the basal BN layers is carried out, using the density-functional theory (DFT)[60,61] and the local density approximation (LDA)[61].

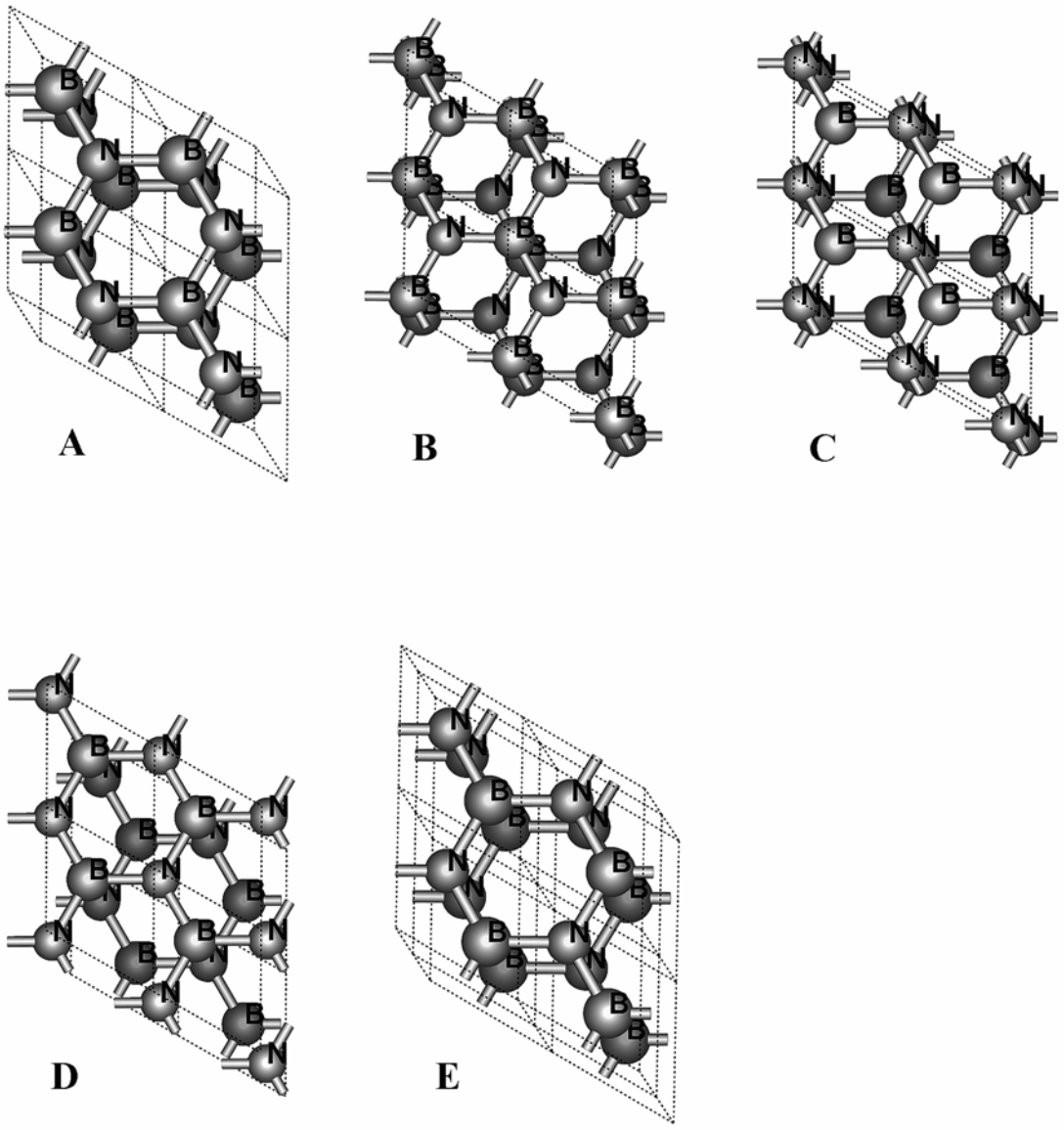

Figure 5.1 *h*-BN structures considered in this study.

5.2 Structural properties of *h*-BN with different stacking

XRD data show that a few different types of *h*-BN (*Z*=2) with space groups of $P6_3/mmc$ (194),[52] $P\bar{6}m2$ (187),[53,54] $P\bar{3}m1$ (164)[55-57] and $P\bar{6}$ (174),[58] as shown in Table 5.1, are possible. However, based on symmetry consideration, there can be only five hexagonal *h*-BN structures (*Z*=1 or 2). These five structures are shown in Fig. 5.1 and the corresponding space groups are $P6_3/mmc$ (194) for structures A, B and C, P3m1 (156) for structure D, and $P\bar{6}m2$ (187) for structure E. We suggest that the *h*-BN structures with the $P\bar{3}m1$ (164)[55-57] symmetry observed experimentally should be noted P3m1 (156), because it is impossible for *h*-BN (*Z*=2) to have the $P\bar{3}m1$ (164).

Table 5.1 *h*-BN crystal structures determined by XRD.

Space Group	*a* (Å)	*c* (Å)	Reference
$P6_3/mmc$ (194)	2.50441(7)	6.6522(4)	[52]
$P\bar{6}m2$ (187)	2.502(2)	6.66(1)	[53]
$P\bar{6}m2$ (187)	2.50399(5)	6.6612(5)	[54]
$P\bar{3}m1$ (164)	2.502(2)	6.66(1)	[55]
$P\bar{3}m1$ (164)	2.5000(1)	6.6609(5)	[56]
$P\bar{3}m1$ (164)	2.51	6.69	[57]
$P\bar{6}$ (174)	2.51	6.69	[58]

Among the five possible structures, structure A with the $P6_3/mmc$ is most commonly accepted. These five structures can be transformed into each other, by translational gliding moves of one BN basal layer relative to the other layer in the unit cell, or by rotational moves of one BN basal layer around the *c*-axis of the crystal. However, if only translational moves are permitted, then the five *h*-BN structures can

be divided into two groups. The first group (I) consists of structures A, B, and C with space group $P6_3/mmc$, and the second group (II) is composed of structures D and E with space group P3m1 and $P\bar{6}m2$ respectively. In each group, the *h*-BN structures can commute into each another by varying the relative stacking of the BN basal layers.

Theoretical investigations on the structural and electronic properties of *h*-BN were carried out using first-principles method based on the DFT and the LDA with Perdew-Zunger parametrization[62] for the exchange and correlation interaction. Each *h*-BN structure was optimized within the given space group using the CASTEP code.[63] The ultrasoft pseudopotential[64] was used in our calculation and the electron wave function was expanded using plane waves with a kinetic energy cutoff of 540 eV. K-points were generated using the Monkhorst-Pack scheme with parameters: 12, 12, and 4. The error of our calculations is less than 0.001 eV/atom. In addition to the five *h*-BN structures, two graphitic structures with hexagonal symmetry were also studied for comparison. These two graphitic structures, F with space group $P6_3/mmc$ (194) and G with space group P6/mmm (191), are shown in Fig. 5.2. The calculated total energies per atom and the lattice parameters of these structures are listed in Table 5.2. The optimized structures A, B and D have similar lattice parameters *a* and *c*, which are in good agreement with the experimental results given in Table 5.1. Their total energies per atom are also close. On the other hand, the optimized structures C and E have relatively larger lattice constant *c*, and relatively higher total energies per atom. Similarly, in the case of graphite, structure F, the common graphitic structure, has lower total energy and much shorter lattice constant c than structure G.

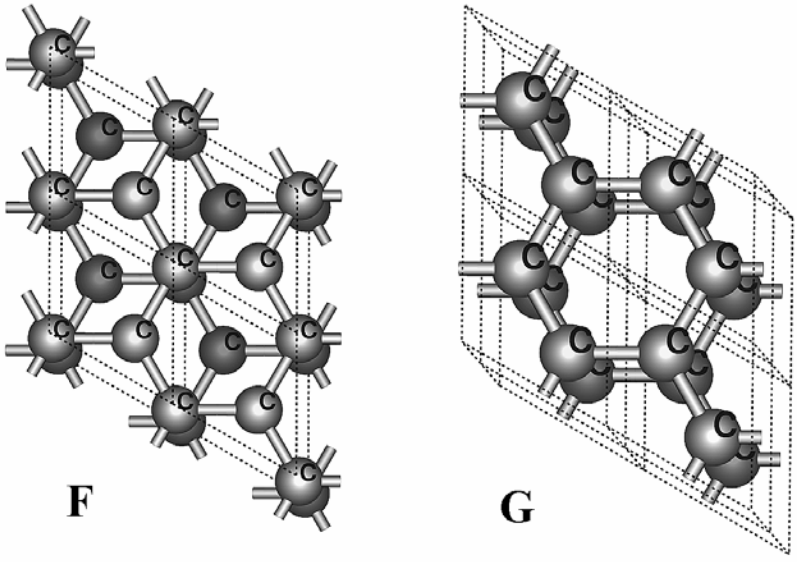

Figure 5.2 Graphitic structures for reference. The two structure F and G have the space groups $P6_3/mmc$ (194) and P6/mmm (191) respectively.

Table 5.2 Calculated structure and total energy of various *h*-BN structures.

Group	Structure	Space Group	a (Å)	c (Å)	Total Energy (eV/atom)	Stability	E_g (eV)
h-BN	A	$P6_3/mmc$ (194)	2.485	6.49	-175.849	Stable	4.027 (ind)
Group I	B	$P6_3/mmc$ (194)	2.484	6.487	-175.847	meta-stable	3.395 (dir)
	C	$P6_3/mmc$ (194)	2.484	7.048	-175.837	Unstable	3.433 (ind)
h-BN	D	P3m1 (156)	2.485	6.423	-175.849	Stable	4.208 (ind)
Group II	E	$P\bar{6}m2$ (187)	2.485	6.912 (×2)	-175.835	Unstable	3.226 (ind)
Graphite	F	$P6_3/mmc$ (194)	2.439	6.654	-155.560	Stable	
	G	P6/mmm (191)	2.439	7.234 (×2)	-155.548	Unstable	

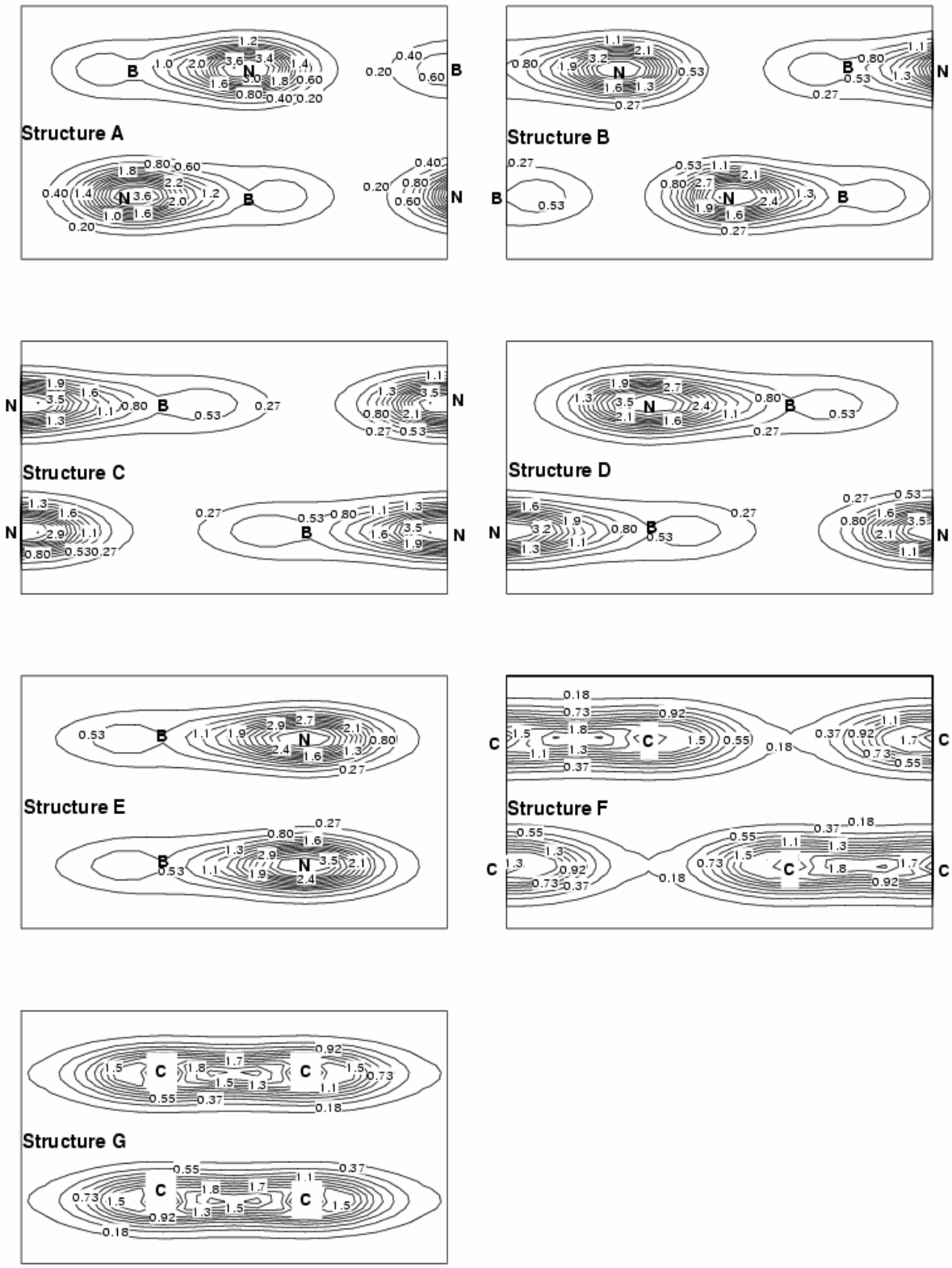

Figure 5.3 Contour plots of total charge densities in the (1100) plane for the five *h*-BN and two graphitic structures being studied.

Compared with hexagonal graphite that has only one stable structure, *i.e.* structure F, *h*-BN has three possible stable structures, *i.e.* structures A and B, both with $P6_3/mmc$ (194) symmetry, and D with P3m1. This could be due to the characteristics of the mixed covalent-ionic bonding of *h*-BN, in contrast to pure covalent bonding of graphite. As shown in Fig. 5.3, where the total valence charge-density of the five *h*-BN structures and the two graphitic structures are shown using contour plots in the (1100) plane containing both BN and CC bonds, all *h*-BN and graphitic structures have strong bonding in the *ab*-plane but weak bonding in the *c*-direction. This is a result of strong covalent intra-layer bonds and weak inter-layer Van der Waals bonding. In the case of graphitic structures which show pure covalent bonding characteristics, the charge density is distributed equally around the C atoms (Fig. 5.3(Structure F-G)) and the interlayer Van der Waals interaction favors a stacking sequence in which the hexagonal graphitic rings in adjacent layers are shifted, *i.e.* the ABAB stacking sequence. However, in the case of *h*-BN which shows mixed covalent-ionic bonding characteristics, the valence charges are concentrated around the N atoms (Fig. 5.3(Structure A-E)) and the layer stacking in the three *h*-BN structures A, B, and D yields local energy minima.

To further investigate the stability of these five *h*-BN structures, we calculated the variation of the total energy per atom of the structures in each group as a function of relative translational move of one basal BN layer with respect to the other in the unit cell. For the group I structures, as shown in Fig. 5.4, structure A was found to be a stable structure and its energy per atom is at the global minimum. Structure B is a meta-stable phase and its energy is at a local minimum which is only slightly higher than that of structure A. But structure C is unstable as its energy is at the maximum point the energy surface. The equilibrium structure of C has a relatively longer lattice

parameter *c*, as shown in Table 5.2. The group II structures, D and E, show similar behaviors. As shown in Fig. 5.5, structure D is a stable structure at the minimum point of total energy, but structure E is unstable at the maximum point of total energy. The equilibrium structure of E also has a longer lattice constant *c*, as indicated in Table 5.2. Recently, Mosuang and Lowther investigated, using density functional approach with LDA, three BN phases with different stacking sequences which correspond to structures A, C, and E here. However, they concluded that all three structures were stable. This could be due to that interlayer gliding effect was not considered in their study.

According to the results presented above, among the five structures of *h*-BN, structures A, B, and D are stable and the corresponding stacking of the BN layers can be regarded as energetically favorable or "good" stacking sequences. Structures C and D are unstable and their stacking sequences can be regarded as unfavorable or "bad". Structures with "bad" stacking sequences generally have larger *c* values compared to structures with "good" stacking sequences. The five structures A, B, C, D and E represent the extremes of stacking. Based on these, we can infer the structural or electronic properties of structures with disorder in stacking sequence such as PBN and *t-BN*. In PBN, stacking disorder typically occurs because PBN is often deposited with a preferred orientation and the *c*-axis is perpendicular to the surface, resulting in slightly higher (2-4 %) interlayer spacing.[16] Similarly, in *t-BN* which has random stacking of the BN basal layers, a larger than the ideal d_{002} value in XRD analysis is often used as an indicator for the turbostratic structure, and dropping of this quantity to a certain critical value during heat treatments was accepted as an indicator for ordering in the crystal structure.[20] Based on the results of the present study, we conclude that the

larger interlayer spacing of PBN and *t-BN* is due to their mixed stacking behaviors since our calculations suggest that "bad" stacking results in larger lattice constant *c*.

The existence of a meta-stable structure B is significant. The small difference in total energies of structure A and structure B implies that it is possible for *h*-BN crystals with the $P6_3/mmc$ symmetry to have mixed stacking behaviors of structures A and B, resulting in intrinsic stacking fault in real *h*-BN crystals. Furthermore, once *h*-BN with the $P6_3/mmc$ symmetry is formed, it is difficult to transform into structure D with the P3m1 symmetry, and vice versa, because a much larger energy barrier must be overcome by the rotational motion in order to transform the crystal structure from one symmetry to the other. Therefore, we conclude that whether *h*-BN crystals adopt the $P6_3/mmc$ or the P3m1 symmetry should be determined by its initial growth conditions.

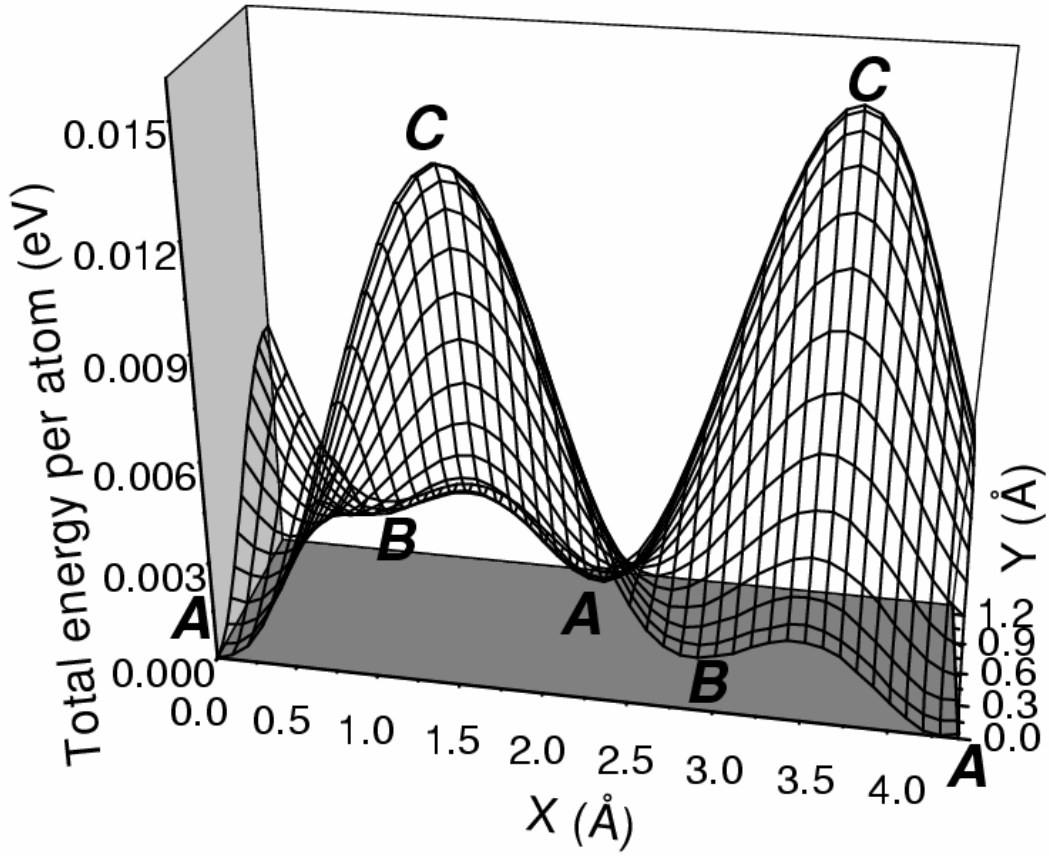

Figure 5.4 Variation of total energy per atom of group I structures as a function of translational gliding move of one BN hexagonal layer relative to the other in the unit cell.

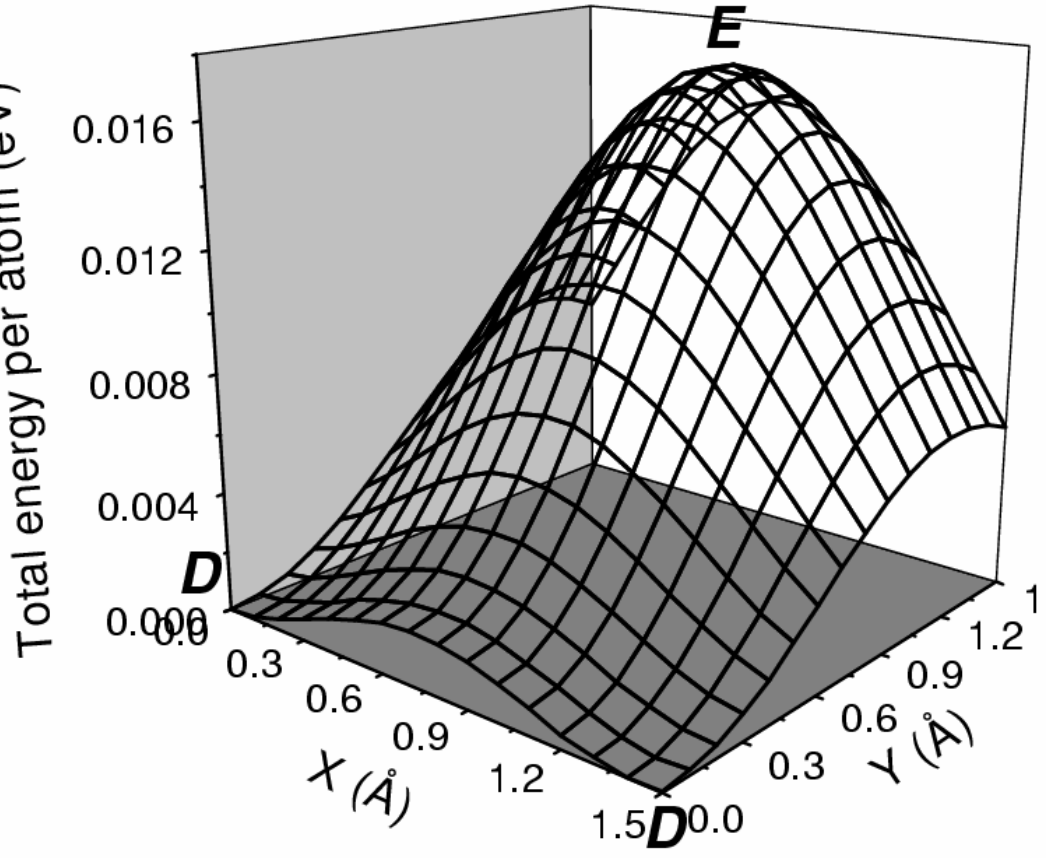

Figure 5.5 Variation of total energy per atom of group II structures as a function of translational gliding move of one BN hexagonal layer relative to the other in the unit cell.

Shown in Fig. 5.6 are the simulated XRD spectra based on the *h*-BN structures A, B and D, respectively. Since these three structures have roughly the same lattice parameters, their XRD spectra have almost the same peak positions, but different intensities which is due to the different stacking of the BN layers. The experimental XRD spectra on real *h*-BN samples[52-58] are some sort of average of the spectra of the three ideal *h*-BN structures which confirms the existence of mixed stacking in real *h*-BN crystals.

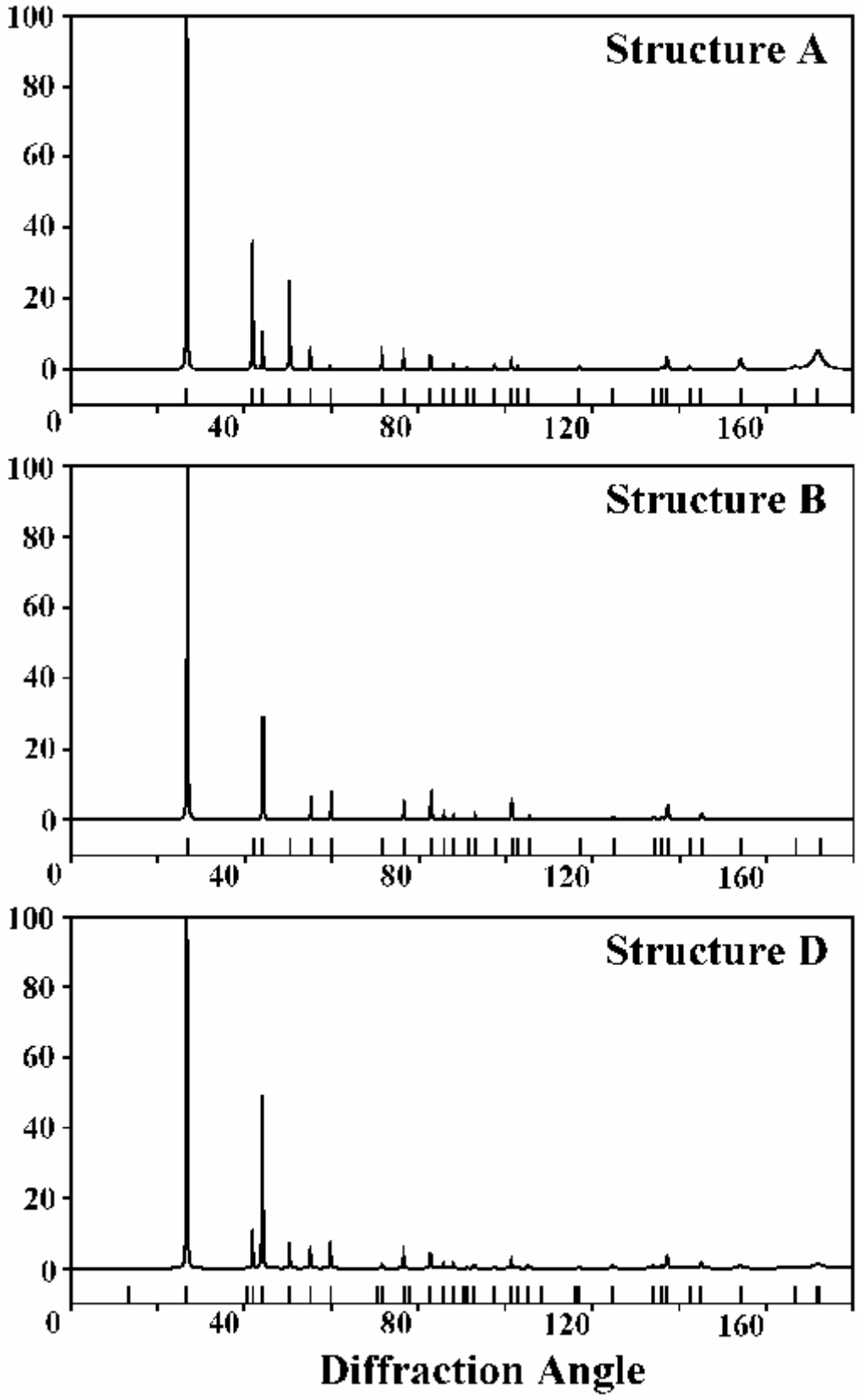

Figure 5.6 Simulated XRD spectra of the stable structures A, B and D respectively.

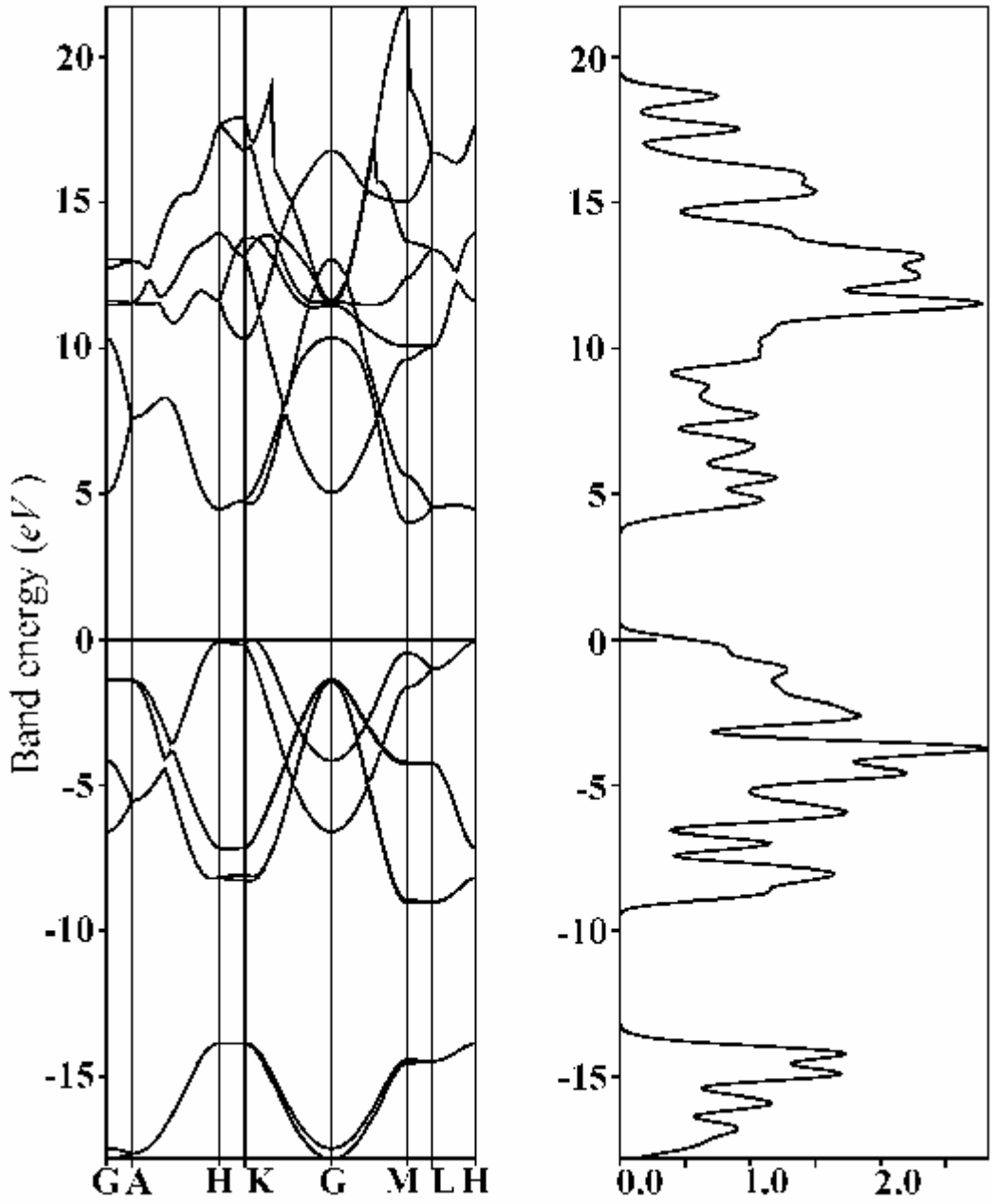

Figure 5.7 Band structure and total DOS of structure A.

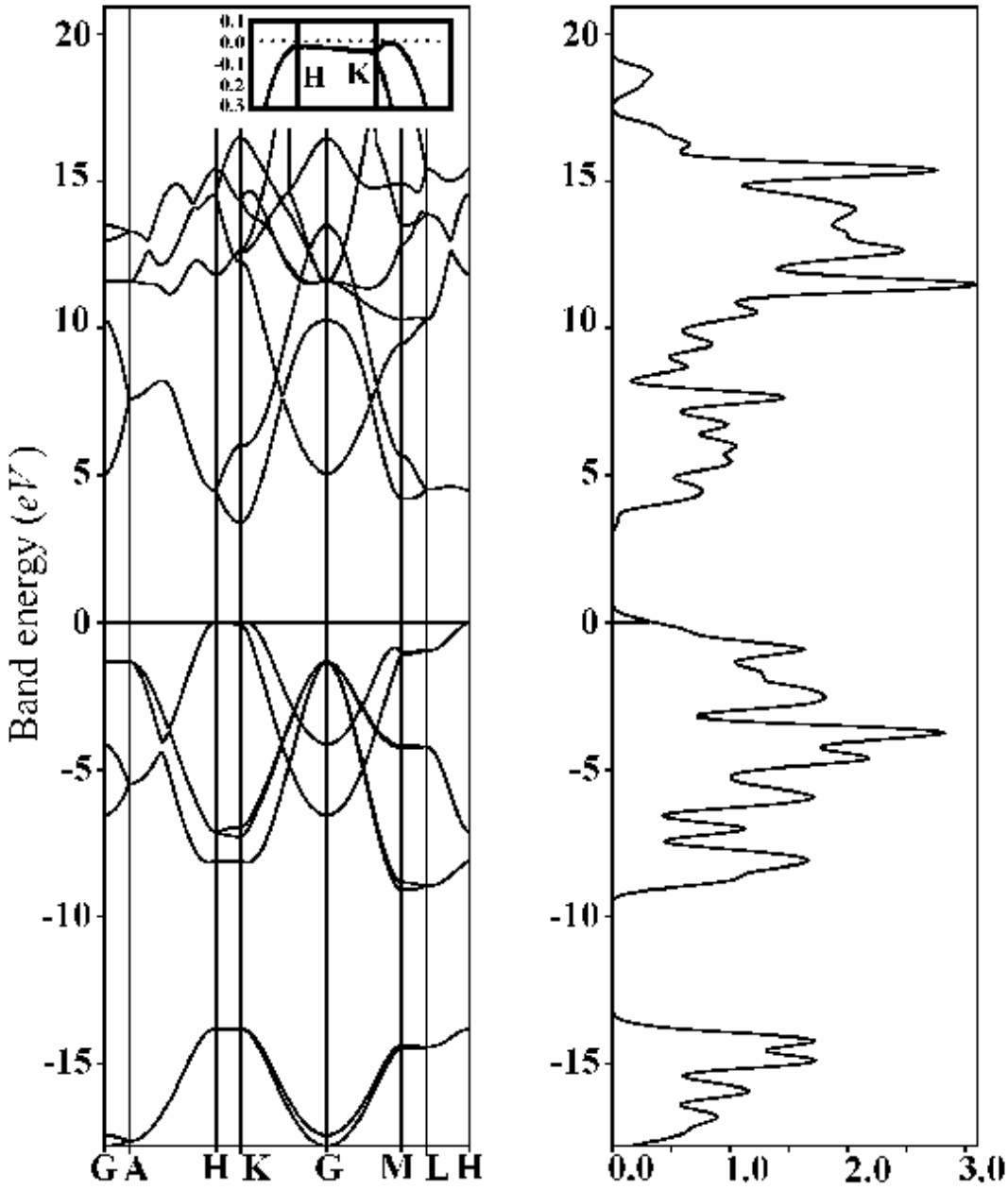

Figure 5.8 Band structure and total DOS of structure B, where K-H dispersion part enlarged.

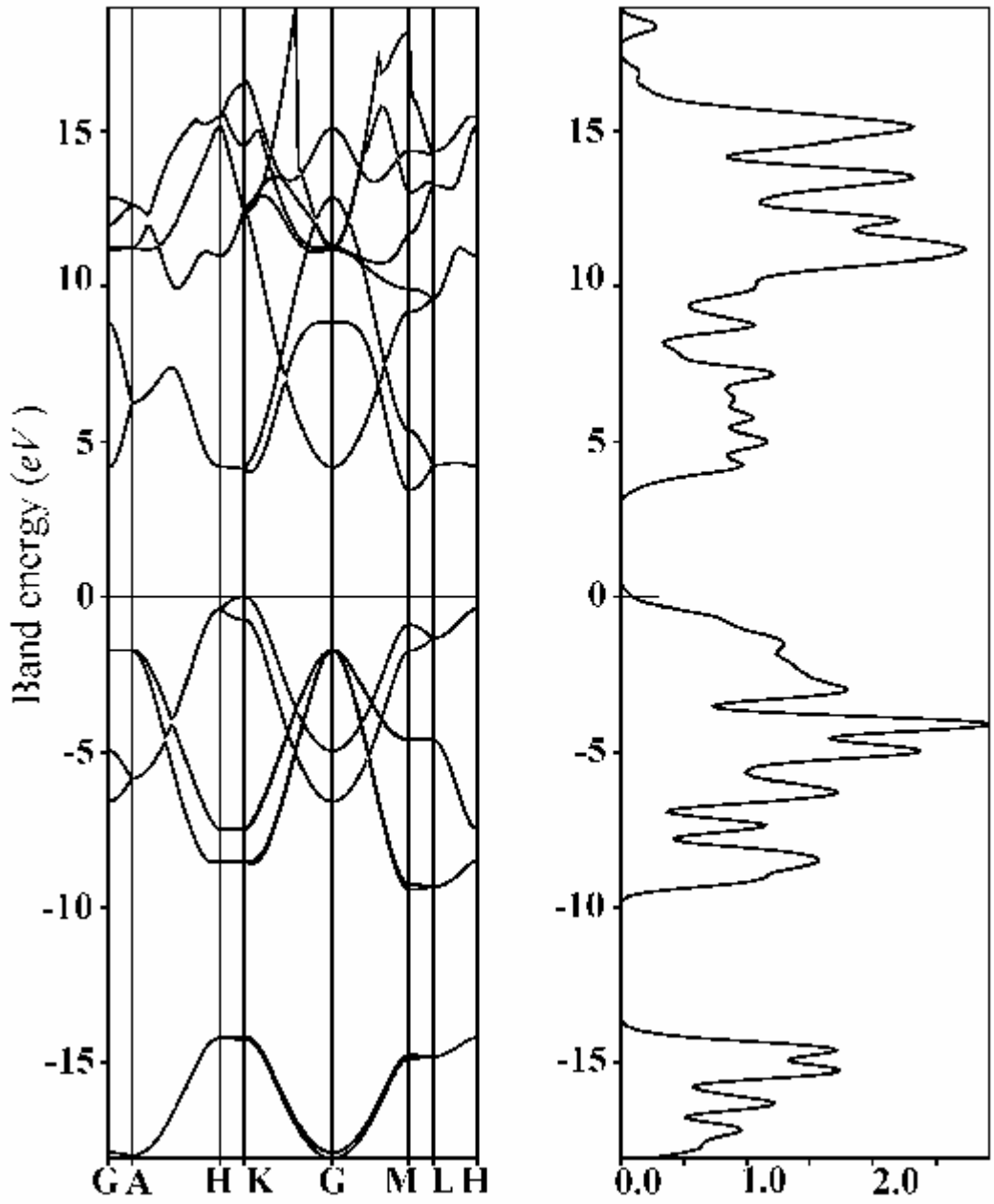

Figure 5.9 Band structure and total DOS of structure D.

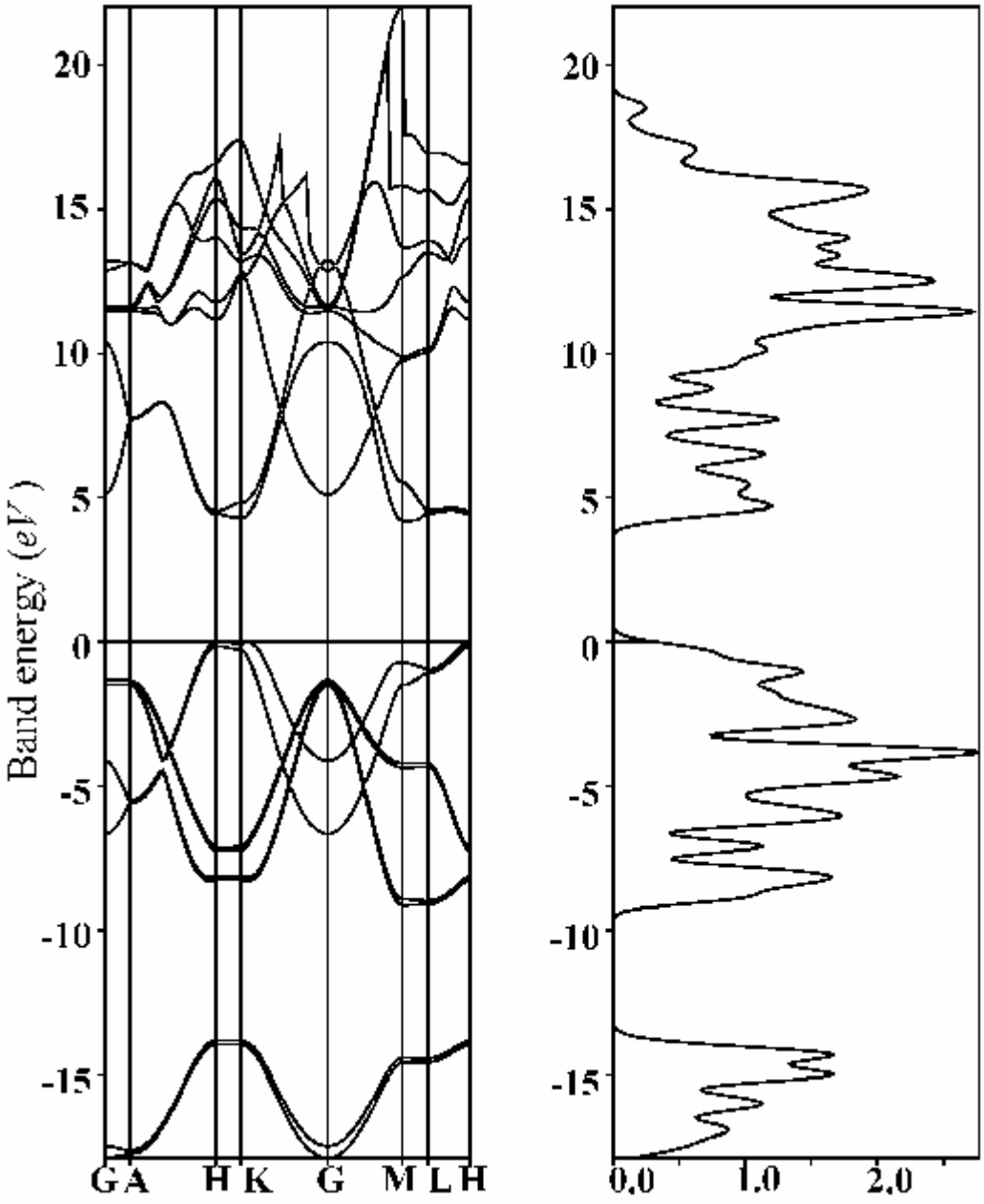

Figure 5.10 Band structure and total DOS of structure C.

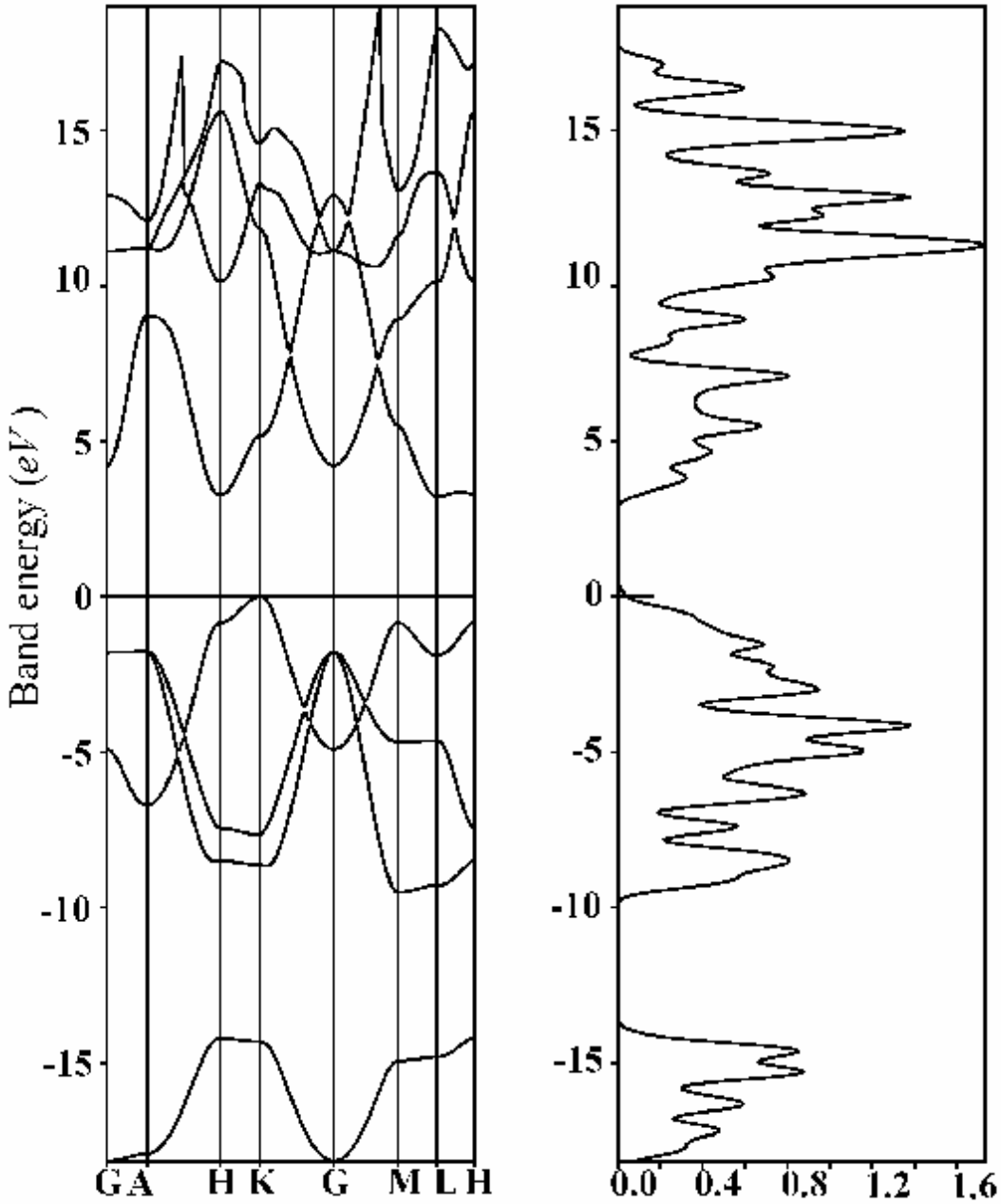

Figure 5.11 Band structure and total DOS of structure E.

5.3 Electrical properties of *h*-BN

The band structures and total density of states (DOS) of the five *h*-BN structures were calculated and are as shown in Figs. 5.7-5.11. It is known that even though the DFT-LDA method underestimates band gaps of semiconductors and insulators, it does give reliable band widths and shapes. In the present work, we focus on comparison of the band structures of the five *h*-BNs which may provide a hint to understand the and gap nature of *h*-BN.

Fig. 5.7 shows the calculated band structure and total DOS of structure A. The band structure is characterized by an indirect band gap of about 4.027 eV, between the valence band maximum near *H* and the conduction band minimum at *M*, and a very small *K*-*H* dispersion. Being the most common *h*-BN phase, the electronic structure of structure A has been extensively studied.[42-46] The band structure calculated in the present work and the prediction of an indirect band gap of 4.027 eV agree well with the results of recent OLCAO calculations of Xu and Ching[45] and the results of Furthmüller *et al.* using ultrasoft pseudopotentials.[46]

For the meta-stable structure B with the $P6_3/mmc$ symmetry, our calculations predict a band gap of about 3.395 eV of essentially direct nature, which has not been observed before. As shown in Fig. 5.8, corresponding to the conduction band minimum at *K* point, the valence band achieves the maximum around *K* points, with considerably small *HK* dispersion which is comparable with the thermal energy at room temperature. So the direct band gap characteristics of *h*-BN observed experimentally can be understood. The existence of structure B changes the nature of electronic structure of *h*-BN and brings about a critical change from indirect band gap to direct band gap, with a drop of the band gap energy by about 0.6 eV.

The band structure of structure D with the P3m1 symmetry was calculated and is shown in Fig. 5.9. The band structure is similar to that of structure A, with an indirect but a slightly large band gap of 4.208 eV, between the valence band maximum at *H* and the conduction band minimum at *M*, with very small *K*-*H* dispersion too.

For comparison, we also calculated the band structures of the unstable *h*-BN structures C and E and the results are shown in Fig. 5.10 and Fig. 5.11 respectively. Both of these two unstable structures with "bad" stacking sequences exhibit indirect band gaps. The band gap energy of structure C is 3.433 eV, between the valence band maximum at *K* and the conduction band minimum at *M*, while that of structure E is 3.226 eV, between the valence band maximum at *K* and the conduction band minimum at *L*. Consequently, any "bad" stacking of BN layers in real *h*-BN would reduce its band gap, and change the characteristics of band structure significantly.

Based on the calculated band structures of various phases of *h*-BN, it is obvious that the electronic structures of *h*-BN show strong dependence on the stacking manner of the BN layers. Structures with "good" stacking sequences already have quite dispersed band gap energies, *i.e.* 4.027, 3.395, and 4.208 eV for structures A, B and D, respectively. Existence of "bad" stacking of the BN layers such as that in structure C or E will further reduce its band gap energy, and change its band structure. It is worthwhile to point out that the meta-stable structure B possesses totally different electronic structure and it is the only *h*-BN structure with a direct band gap. As already indicated in Section II, intrinsic stacking fault should generally exist in real *h*-BN crystals. In other words, real *h*-BN crystals are likely to have mixed stacking sequences of structures A, B and D. Accordingly, the diverse band gap values (3.6 to 7.1 eV) observed experimentally[22] can be understood for the first time and it is a result of band structure variation due to stacking. It is noteworthy that the system errors of different

experimental techniques may induce dispersion of experimental results further. Moreover, the discrepancy over the nature of the band gap, whether it is direct band gap[38] or indirect band gap,[22] can be attributed to the existence of the meta-stable structure B. The relative dominance of stacking sequence A or stacking sequence B in a given *h*-BN will determine whether it is an indirect or a direct band gap material. The electronic property of *h*-BN can thus be fully understood.

Based on the calculated electronic structures, we can also speculate that a band gap much lower than that of normal *h*-BN should be observed for structures with disordered stacking sequences such as PBN and *t*-BN, due to existence of the "bad" stacking behaviors. Furthermore, stacking effects on the band structure of *h*-BN would provide further insight in understanding the electronic and optical properties of *h*-BN, such as energy levels induced by defects or impurities, characteristics of luminescence, etc. The fact that the stacking sequence can be altered by gliding moves of BN layers suggests that tunable band structure can be achieved simply by applying shearing stress on the BN crystals.

5.4 Conclusion

h-BN modifications due to stacking have been investigated thoroughly for the first time using the DFT-LDA method. Firstly, five possible *h*-BN structures, *i.e.* structures A, B, and C with symmetry $P6_3/mmc$ in one group (I) and structures D with P3m1 and E with $P\bar{6}m2$ in another (group II) were studied. Structures A and D are found stable, structure B meta-stable, all with "good" stacking of BN layers. Structures C and E are found unstable. These structures with "bad" stacking of BN layers have longer lattice constant *c* compared to structures with "good" stacking sequences. Real *h*-BN crystals may have mixed stacking and intrinsic stacking faults can be expected

which are the reasons for the large variations of electronic properties of *h*-BN. Stacking sequence disorder is also the origin for the observed larger interlayer spacings in PBN and *t*-BN.

Secondly the electronic properties of *h*-BN were found to be strongly dependent on the stacking of the hexagonal BN layers. Based on the calculated band structures for various phases, we presented a complete explanation on the inconsistency in experimental electronic and optical properties of *h*-BN. The diverse band gap values of *h*-BN observed experimentally now can be understood based on the variation of its band structure due to stacking. The discrepancy in the band gap characteristics of *h*-BN, of being direct or indirect, can be attributed to the existence of the meta-stable structure B. Finally, structures with disordered stacking such as PBN and *t*-BN were predicted to have much lower band gap than that of a normal *h*-BN.

References

1 S. Larach and R. E. Shrader, Phys. Rev. **102**, 582 (1956).

2 S. Larach and R. E. Shrader, Phys. Rev. **104**, 68 (1956).

3 L. Kleinman and J. C. Phillips, Phys. Rev. **117**, 460 (1960).

4 R. Geick, C. H. Perry and G. Rupprecht, Phys. Rev. **146**, 543 (1966).

5 P. J. Gielisse, S. S. Mitra, J. N. Plendl, R. D. Griffis, L. C. Mansur, R. Marshall and E. A. Pascoe, Phys. Rev. **155**, 1039 (1967).

6 D. N. Bose and H. K. Henisch, J. Am. Cer. Soc. **53**, 281 (1970).

7 Q. Johnson and A. C. Mitchell, Phys. Rev. Lett. **29**, 1369 (1972).

8 A. M. Dobrotvorskii and R. A. Evarestov, Phys. Stat. Sol. (**b**) **66**, 83 (1974).

9 A. Katzir, J. T. Suss, A. Zunger, and A. Halperin, Phys. Rev. B **11**, 2370 (1975).

10 A. Zunger, and A. Katzir, Phys. Rev. B **11**, 2378 (1975).

11 E. Y. Andrei, A. Katzir, and J. T. Suss, Phys. Rev. B **13**, 2831 (1976).

12 F. C. Brown, R. Z. Bachrach, and M. Skibowski, Phys. Rev. B **13**, 2633 (1976).

13 A. Zunger, A. Katzir, and A. Halperin, Phys. Rev. B **13**, 5560 (1976).

14 W. H. Gust and D. A. Young, Phys. Rev. B **15**, 5012 (1977).

15 Y. F. Tsay, A. Vaidyanathan, and S. S. Mitra, Phys. Rev. B **19**, 5422 (1979).

16 J. H. Edgar, V. L. Solozhenko, V. V. Lopatin, W. R. L. Lambrecht, B. Segall, and G. L. Doll in *Properties of Group III Nitrides*, edited by J. H. Edgar (London: INSPEC, 1994), p.7 and p.43.

17 C. K. Narula, *Ceramic Precursor Technology and Its Applications* (Marcel Dekker, Inc., New York, 1995).

18 J.Y. Huang, H. Yasuda, and H. Mori, J. Am. Ceram. Soc. **83**, 403 (2000).

19 J. Thomas, JR., N. E. Wetston, and T. E. O'Connor, J. Am. Chem. Soc. **84**, 4619 (1963).

20 S. Alkoy, C. Toy, T. Gönül, and A. Tekin, J. Eur. Ceram. Soc., **17**, 1415 (1997).

21 T. Kobayashi, S. Tashiro, T. Sekine, and T. Sato, Chem. Mater. **9**, 233 (1997).

22 V. L. Solozhenko, A. G. Lazarenko, J.-P. Petitet and A. V. Kanaev, J. Phys. Chem. Solids. **62**, 1331 (2001).

23 P. Widmayer, H. -G. Boyen, P. Ziemann, P. Reinke and P. Oelhafen, Phys. Rev. B **59**, 5233 (1999).

24 C. A. Taylor II, S. W. Brown, V. Subramaniam, S. Kidner, S. C. Rand, and R. Clarke, Appl. Phys. Lett. **65**, 1251 (1994).

25 R. D. Leapman and J. Silcox, Phys. Rev. Lett. **42**, 1361 (1979).

26 R. D. Leapman, P.L. Fejes, and J. Silcox, Phys. Rev. B **28**, 2361 (1983).

27 C. Tarrio and S. E. Schnatterly, Phys. Rev. B {\bf 40}, 7852 (1989).

28 J. Barth, C. Kunz, and T. M. Zimkina, Solid State commun. **36**, 453 (1980).

29 E. Tegeler, N. Kosuch, G. Wiech, and A. Faessler, Phys. Status Solidi B **91**, 223 (1979).

30 R. D. Carson and S. E. Schnatterly, Phys. Rev. Lett. **59**, 319 (1987).

31 A. Mansour and S. E. Schnatterly, Phys. Rev. B **36**, 9234 (1987).

32 B. M. Davies, F. Bassani, F. C. Brown, and C. G. Olson, Phys. Rev. B **24**, 3537 (1981).

33 J. J. Jia, T. A. Callcott, E. L. Shirley, J. A. Carlisle, L. J. Terminello, A. Asfaw, D. L. Ederer, F. J. Himpser, and R.C. C. Perera, Phys. Rev. Lett. **76**, 4054 (1996).

34 J. A. Carlisle, E. L. Shirley, L. J. Terminello, J. J. Jia, T. A. Callcott, D. L. Ederer, R. C. C. Perera, and F. J. Himpsel, Phys. Rev. B **59**, 7433 (1999).

35 M. J. Rand and J. F. Roberts, J. Electronchem. Soc. **115**, 423 (1968).

36 W. Baronian, Mater. Res. Bull. **7**, 119 (1972).

37 J. Zupan and D. Kolar, J. Phys. Chem. **5**, 3097 (1972).

38 D. M. Hoffman, G. L. Doll, and P. C. Eklund, Phys. Rev. B **30**, 6051 (1984).

39 R. Mamy, J. Thomas, G. Jezequel, and J. C. Lemonnier, J. Phys. (Paris) Lett. **42**, 473 (1981).

40 V. V. Lopatin and F. V. Konusov, J. Phys. Chem. Solids **53**, 847 (1992).

41 L. G. Carpenter, and P. Y. Kirby, J. Phys. D **15**, 1143 (1982).

42 J. Robertson, Phys. Rev. B **29**, 2131 (1984).

43 A. Catellani, M. Posternak, A. Baldereschi, and A. J. Freeman, Phys. Rev. B **36**, 6105 (1987).

44 K. T. Park, K. Terakura, and N. Hamada, J. Phys. C: Solid State Phys. **20**, 1241 (1987).

45 Y. N. Xu and W. Y. Ching, Phys. Rev. B **44**, 7787 (1991).

46 J. Furthmüller, J. Hafner, and G. Kresse, Phys. Rev. B **50**, 15606 (1994).

47 W. Orellana and H. Chacham, Phys. Rev. B **63**, 125205 (1994).

48 I. Jiménez, A. F. Jankowski, L. J. Terminello, D. G. J. Sutherland, J. A. Carlisle, G. L. Doll, W. M. Tong, D. K. Shuh, and F. J. Himpsel, Phys. Rev. B **55**, 12025 (1997).

49 I. Tanaka, H. Araki, M. Yoshiya, T. Mizoguchi, K. Ogasawara, and H. Adachi, Phys. Rev. B **60**, 4944 (1999).

50 R. S. Pease, Nature. **165**, 722 (1950).

51 R. S. Pease, Acta crystallogr. **5**, 356 (1952).

52 JCPDS, 34-0421

53 JCPDS, 45-0895

54 JCPDS, 73-2095

55 JCPDS, 45-0893

56 JCPDS, 45-0896

57 JCPDS, 74-1977; JCPDS, 74-1978

58 JCPDS, 85-1068

59 T. E. Mosuang and J. E. Lowther, J. Phys. Chem. Solids **63**, 363 (2002).

60 P. Hohenberg, and W. Kohn, Phys. Rev. **136**, 864 (1964).

61 W. Kohn and L. J. Sham, Phys. Rev. A, **140**, 1133 (1965).

62 J. P. Perdew and A. Zunger, Phys. Rev. B, **23**, 5048 (1981).

63 M. C. Payne, M. P. Teter, D. C. Allan, T. A. Arias, J. D. Joannopoulos, Rev. Mod. Phys. **64**, 1045 (1992).

64 D. Vanderbilt, Phys. Rev. B **41**, 7892 (1990); K. Laasonen, R. Car, C. Lee and D. Vanderbilt, Phys. Rev. B **43**, 6796 (1991).

Chapter 6

Phase Transition Mechanism in KIO_3 Single Crystals

6.1 Background of ferroelectric phase transitions

Electrical properties such as piezoelectricity, pyroelectricity and ferroelectricity are always associated with the chemical and crystalline structures of the materials.[1] A piezoelectric material exhibits polarization on application of mechanical stress, such as pressure, or conversely exhibits expansion or contraction in an electric field. There are 20 noncentrosymmetric crystal point groups exhibiting piezoelectricity, but only 10 of them permit the existence of pyroelectricity.[1,2] In a pyroelectric crystal, the dipole moment has a temperature coefficient that originates from anharmonicity of the lattice vibrations. When such a polar crystal is heated or cooled, the external or internal conduction often cannot yield enough current to compensate for the change of the dipole moment, and the crystal acts as an electric dipole.[3]

The ferroelectrics are a subgroup of the pyroelectrics. Their outstanding property is the reversibility of the permanent polarization by an electric field.[3] Many ferroelectrics possess a spontaneous dipole moment only in certain temperature ranges. At the boundaries of these ranges the crystal undergoes a phase transition to a non-

pyroelectric phase. The phases with and without a spontaneous dipole moment are referred to as ferroelectric and paraelectric respectively.[4]

The ferroelectric phase transition is a structural transition, as a result of which a spontaneous polarization occurs in the crystal, i.e., a component of the electric polarization vector, which is caused by relative displacements of atoms in each of the unit cells of the crystal and which results in the appearance of a pyroelectric effect in the crystal.[5] Phase transitions in ferroelectric crystals can be classified into two main categories, order-disorder and displacive. In the paraelectric phase, if the atomic displacements are oscillations about a single nonpolar site, then the paraelectric to ferroelectric transition (PE – FE) is displacive and the atomic displacements after the transition are about a polar site.[6] However, if in the paraelectric phase the displacements are about several sites characterized by a double-well or multi-well configuration, then the PE –FE transition is an order-disorder type and the displacements after the transition is about a single polar site (if they are about a double-well in the PE phase) or still about several (but reduced number of) sites (if they are about a multi-well in the PE phase).[6] The displasive transitions involve the special lattice vibrations i.e. soft modes, which freeze near T_c, as predicted by the Cochran theory.[7] On the other hand, the order-disorder transitions occur through collective tunneling or thermally assisted hopping, which give rise to central peaks whose widths yield the hopping rates.[8] It should be stressed that no sharp boundary line can be drawn between displacive and order-disorder phase transitions.[5] In real ferroelectric crystals, such as $BaTiO_3$, $KNbO_3$, and $PbTiO_3$, which had been considered as exemplary displacive ferroelectrics, have been found to be better described by the crossover mechanism from order-disorder to displacive, by XAFS measurements,[9] Raman and hyper-Raman scattering,[10-13] and theoretical simulations.[14-17] Generally in

such prototype ferroelectric systems, the order parameter is the spontaneous polarization or the sublattice polarization and where the anomalies in the dielectric properties are a direct consequence of the increased correlation in the order parameter fluctuations near T_c. In the ferroelectric case we call such systems proper ferroelectrics.[18]

While the phase transition is called ferroelectric if a spontaneous polarization occurs in the nonsymmetric phase, it does not mean that it is proportional to the order parameter – in a phase transition a number of "parameters" may appear, whose symmetry properties do not describe in full measure symmetry changes that occur at the transition point.[5] Naturally, a spontaneous polarization may also occur in a crystal as a second-order effect, accompanying a more complicated change of the crystal structure of a substrate. Ferroelectric phase transitions, for which the order parameter is proportional not to polarization but to another physical quantity having other transformation properties, are called improper ferroelectric phase transitions and substances with such transitions are referred to as improper ferroelectrics.[5] Such ferroelectrics differ in a number of physical properties from the ordinary proper ferroelectrics. The characteristic features of improper ferroelectrics are a very slight change of the dielectric constant near the transition point and its unusual temperature dependence and also a low spontaneous polarization. In all improper ferroelectrics known to date there is observed a multiple change of the unit cell volume upon transition into a nonsymmetric phase.[5]

6.2 Introduction

Being a ferroelectric material, KIO_3 single crystals have been studied extensively since 1960.[19, 20] It is an excellent nonlinear crystal, which has the largest

non-linear optical coefficient among all the iodate crystals,[21, 22] and after detwinning and domain removal, it can be used to fabricate nonlinear optical devices with good optical quality.[23]

However, up to date, there has no agreement on the phase transitions of KIO_3 single crystals. KIO_3 has been reported to undergo phase transitions at about 485K (phase I to phase II), 343K (II – III), 255K(on cooling)/263K(on heating) (III – IV), and 83K (IV – V) respectively. All the phases are ferroelectric, except the paraelectric phase I above 485K.[19,24] The first three phases were described as rhombohedral phase I (space group $R\bar{3}m$), monoclinic phase II (space group Pm), and triclinic phase III (space group P1).[24] Nevertheless, based on neutron diffraction data, P. G. Byrom and B. W. Lucas argued that phase I belongs to the non-centrosymmetric space group R3, and proposed that the only structural transition in the temperature range of 10K to 523K was the room temperature triclinic (pseudo-rhombohedral) phase III (P1, Z=4) to the rhombohedral (pseudo-cubic) phase I (R3, Z=1).[25-27] However, by the MEM/Rietveld analysis from high-energy X-ray powder-diffraction data, the crystal structure of phase I is identified as the rhombohedral structure (space group R3m, Z=1).[28] Moreover, the recent dielectric, elastic and piezoelectric measurements supported the existence of phase II, and suggested two orientational glass-transitions around 113K and 33K.[29]

Furthermore, the mechanism governing the phase transitions of KIO_3 single crystals has not been understood well either. E. Sajie indicated that the phase transitions I-II and II-III are accompanied by a "soft-mode" behavior of some transversal modes,[24] suggesting the displacive characters of these two phase transitions. Recently, M. Ahart *et al*. reexamined the low-frequency region of Raman spectra of KIO_3 single crystals. They observed one soft mode (63 cm^{-1} at 93K) and two

soft modes (32 cm^{-1} and 38 cm^{-1} at 93K) after the phase transitions I-II and II-III respectively, and suggested that these two phase transitions were displacive in nature.[30] But at the same time they pointed out that the Rayleigh wings related to the soft modes still remain above the I-II phase transition temperature, and speculated that this phase transition still has some features of the order-disorder nature.[30] Moreover, M. Ahart *et al*. pointed out that phase transition I-II would belong to improper ferroelectrics whose order parameters are some physical quantities at the Brillouin zone boundary, and phase transition II-III can be related to the coupling between the strain and the soft modes.[30] KIO_3 single crystals were observed by the dielectric constant investigations of M. Maeda *et al*.[29] In their experiments, the overall behavior of the dielectric constants $\varepsilon_{[100]}$ and $\varepsilon_{[111]}$ were almost the same including the effect of thermal annealing. For the real and imaginary parts of the dielectric constant $\varepsilon_{[100]}$ at 10 kHz, a tiny anomaly was observed at $T_1 = 486K$ (phase transition I-II) and a step-shape anomaly was observed at $T_1 = 345.5K$ (phase transition II-III) in the real part, but no obvious anomaly was detected in the imaginary part.[29]

From the above discussion, it is clear that although much work about the phase transitions of KIO_3 single crystals has been done, the nature of phase transitions of the crystal is still very much an issue for further research. Moreover, both the later neutron scattering observations[25-27] and the recent EXAFS study[31] have indicated that the iodine and oxygen atoms exist as IO_3 ions in the crystals rather than as IO_6 complex. However, the previous Raman spectra obtained by E. Sajie on KIO_3 single crystals in different phases were analyzed according to the IO_6 octahedron.[24] Thus it would be very meaningful to reconsider the origin of the Raman features of KIO_3, especially the origin of the soft modes and the central component of the spectra which could contribute to elucidate the phase transition mechanism in KIO_3. Furthermore, up

to date, few theoretical calculations on KIO_3 single crystals have been carried out to study its phase structural properties, although intensive theoretical investigations have contributed significantly to understand the structural properties of ferroelectric crystals, such as the crossover phase transition mechanism from order-disorder to displacive of ABO_3 perovskite.[14-17] Especially the first-principles calculations have been proven to be one of the most powerful tools for carrying out theoretical studies of the electronic and structural properties of materials.[32] In this chapter, we present our detailed polarized Raman study on KIO_3 at variable temperature, and report our first-principles analysis of the ground-state structural and dynamical properties of KIO_3 single crystals in rhombohedral (pseudo-cubic) phase I, using the utilizing density functional perturbation theory (DFPT) and local density approximation (LDA).[33,34] The aim of this study is to provide a clear understanding of the phase transition mechanism in KIO_3 single crystals.

6.3 Raman results of KIO_3 in different phases

The KIO_3 single crystals used in our experiment were grown from aqueous solution.[35] The crystal axes of the sample were identified by the XRD technique, and the experimental coordinates were chosen as follows: the [111] direction of the KIO_3 single crystal is along the coordinate basis vector $\hat{z}$, and the $[1\bar{1}0]$ direction is along the basis vector $\hat{x}$. The micro-Raman experiments were carried out in backscattering geometry using a JY T64000 triple-grating spectrometer, over the temperature range 78-600K. A Spectra Physics Ar^+ ion laser (λ= 514.532 *nm*, power = 15 *mW*) served as the excitation source, and the laser spot at the sample surface was about 3 μm in diameter.

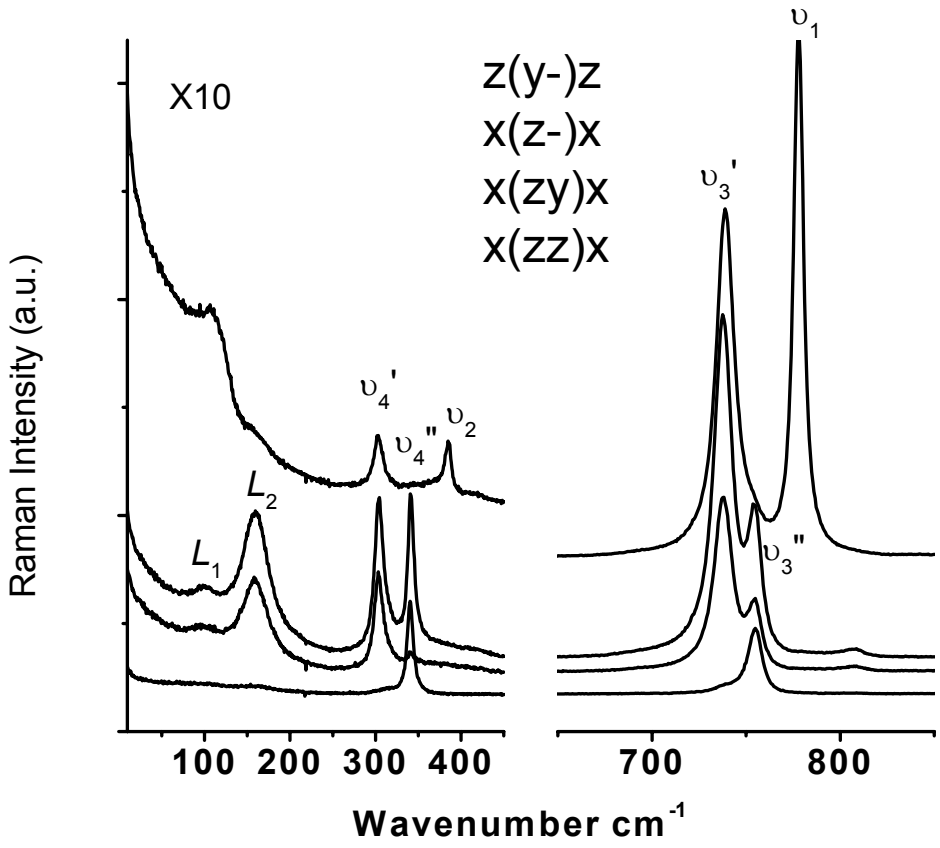

Figure 6.1 Polarized Raman spectra of KIO_3 single crystals at 573K.

Fig. 6.1 displays the polarized Raman spectra of KIO_3 single crystals in the rhombohedral phase I (at 573K). In the spectra, under different polarization configurations, six bands (ν_1, ν_2, ν'_3, ν''_3, ν'_4, and ν''_4) above 300 cm^{-1}, two bands (L_1 and L_2) below 200 cm^{-1}, and a central peak near the laser line can be observed. E. Sajie ascribed the six bands above 300 cm^{-1} to A_g^1 (ν_1), E_g^1 (ν'_3, ν''_3), E_g^2 (ν_2, ν''_4), and A_g^2 (ν'_4), based on the $R\bar{3}m$ crystal structure (Z=2) and the IO_6 complex.[24] However, according to the neutron data,[25-27] in the rhombohedral phase I (R3, Z=1) iodine and oxygen atoms exist as IO_3 ions positioned about the threefold symmetry axis, *i.e.* the [111] direction, with regular undistorted conformation.[27] The recent EXAFS study[31]

also suggested that iodine and oxygen atoms exist as IO_3 ions in the crystals, and by the MEM/Rietveld analysis from high-energy X-ray powder-diffraction data, the crystal structure of phase I is identified as the rhombohedral structure (space group R3m, Z=1).[28] Whatever, both the neutron[25-27] and X-ray[28,31] results agree the size (Z=1) of the unit cell in rhombohedral phase I. Consequently in phase I all together 12 optical modes (both infrared- and Raman-active) exist at the Brillouin zone center, including the six iodate-ion internal modes (2A+2E) and the six lattice external modes (2A+2E).

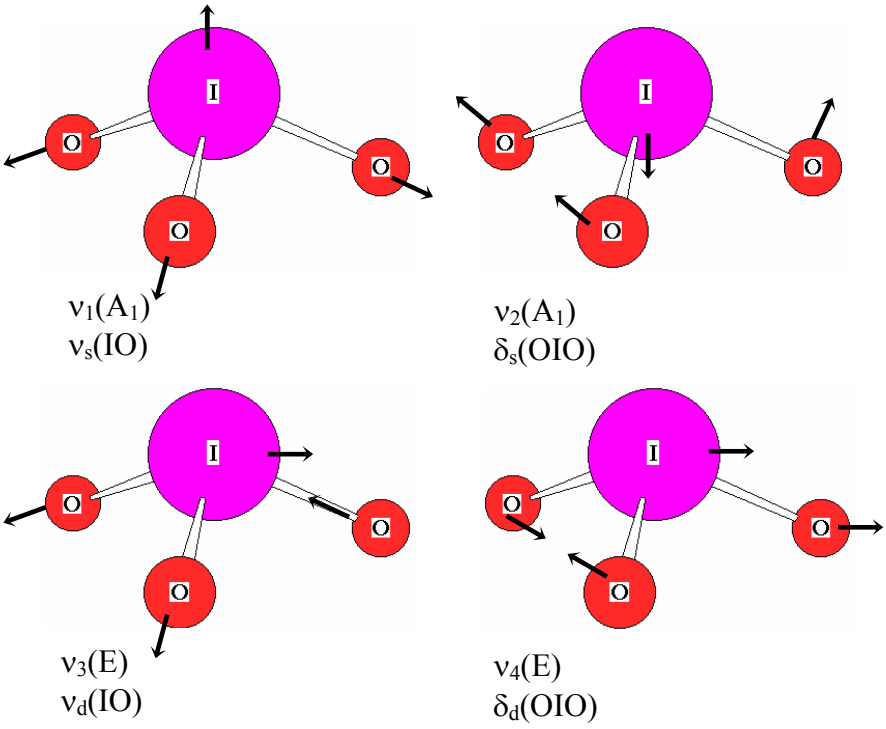

Figure 6.2 Internal vibrational modes of the IO_3 group.

Fig. 6.2 illustrates the six internal modes of the iodate ion, which are similar to those of the free IO_3^{-1} anion of C_{3v} symmetry in solution. In solution, the IO_3^{-1} anion has the following (both infrared- and Raman-active) vibrational modes: $\nu_1(A_1)$, $\nu_2(A_1)$, $\nu_3(E)$, and $\nu_4(E)$ with frequencies at 805, 358, 775, and 320 cm^{-1} respectively.[36] Accordingly we ascribed the two bands below 200 cm^{-1} to the lattice external modes,

and the six bands above 300 cm^{-1} to the six iodate-ion internal modes (2A+2E), i.e. marked as ν_4' and ν_4'' at about 305 and 341 cm^{-1} respectively in Fig. 6.1 to the $\nu_4(E)$ modes, ν_3' and ν_3'' at about 740, 754 cm^{-1} respectively to the $\nu_3(E)$, and the bands at about 385 and 778 cm^{-1} as $\nu_2(A_1)$ and $\nu_1(A_1)$ respectively. The splitting of the two two-fold degenerate $\nu_3(E)$ and $\nu_4(E)$ modes could be ascribed to the LO (longitudinal optical modes)-TO (transverse optical modes) splitting due to long-range electrostatic forces associated with lattice ionicity. A dominant Raman feature of KIO_3 in the rhombohedral phase I is the appearance of the rather broad central peak.

Figs. 6.3 and 6.4 show the temperature dependence of Raman spectra of KIO_3, with the $\hat{z}$ and $\hat{x}$ backscattering geometries respectively. Some Raman features related to the phase transitions of KIO_3 can be observed in these two figures. Firstly, the central peak of the spectra becomes narrower and weaker gradually as temperature decreases, and almost disappears at about 140K. However as temperature decreases near and below 83K, the central peak becomes strong again. Secondly, the soft modes S_1 and S_2 emerge from the wing of the central peak, as temperature decreases through the transitions I-II and II-III respectively. As temperature decreases, the soft modes vary from overdamped to underdamped and shift to higher wavenumber. Thirdly, after each phase transition, I-II and II-III, each of the six internal vibration modes and the two lattice modes in the rhombohedral phase I split into more bands. Although the transition from phase I to phase III was proposed to be the only structural transition in the temperature range of 10K to 523K according to the neutron scattering data,[25-27] our Raman results support strongly the existence of the II-III phase transition in KIO_3. Furthermore, after the phase transition III-IV, the hard modes split further, and the soft mode S_1 becomes unsymmetrical, and then splits into two modes, which can be observed clearly at about 62 and 68 cm^{-1} respectively at 90K. It is noteworthy that M.

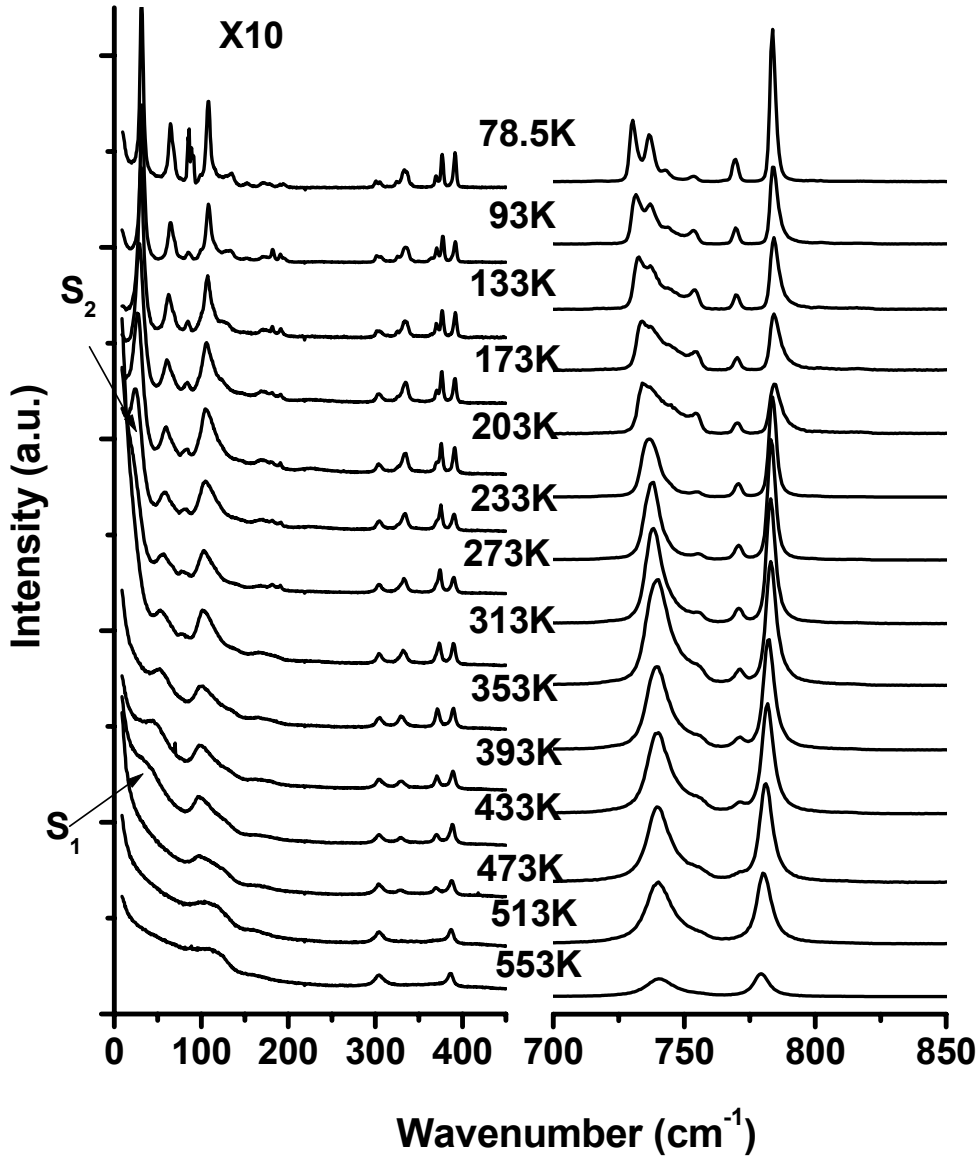

Figure 6.3 Variable-temperature $\hat{z}$ direction backscattering Raman spectra of KIO_3 single crystals.

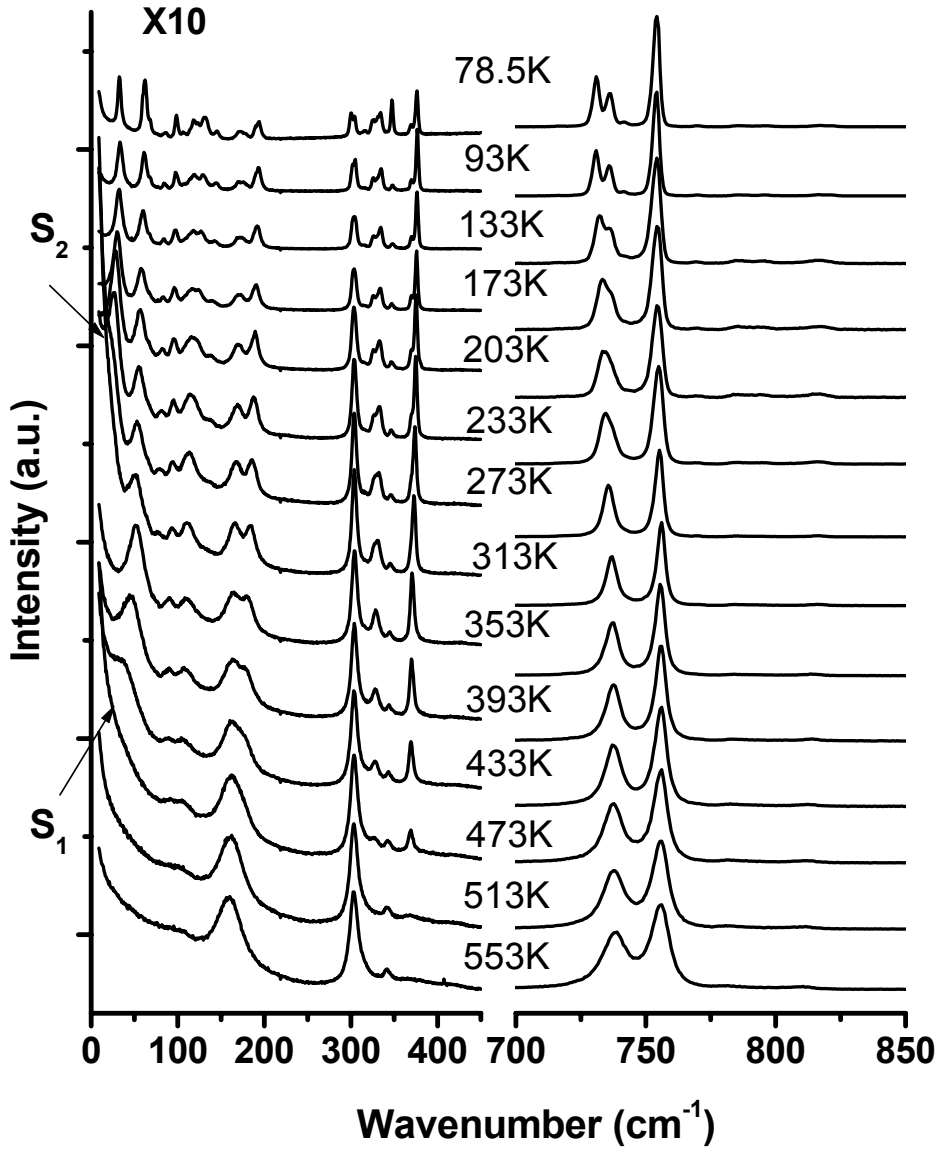

Figure 6.4 Variable-temperature $\hat{x}$ direction backscattering Raman spectra of KIO_3 single crystals.

Ahart *et al.* reported that at 93K the S_2 mode split into two bands at 32 and 38 cm^{-1}, under the scattering geometries of $c(a-b,a-b)\bar{c}$ and $c(a-b,a+b)\bar{c}$, where the pseudocubic axes a, b, c were chosen as the sample axes. Moreover, M. Ahart *et al.* suggested further that these two modes are two soft modes and responsible for phase

transition II-III. Our Raman results also suggest that soft modes S_1 and S_2 should be related to phase transitions I-II and II-III respectively, and each of them may be of two-fold degeneracy.

6.4 LDA calculation results and discussions

Unlike a typical perovskite structure of ABO_3 ferroelectrics, where six O atoms form O_6 octahedron surrounding a B atom, each I atom in KIO_3 has three nearest O atoms, forming an IO_3 pyramid, according to the neuron[25-27] and X-ray[28,31] scattering results. The X-ray results[28,31] reveal further that the shorter I-O bond in IO_3 pyramid exhibits a covalent bonding character while the others (I-K, K-O, and longer I-O bonds) an ionic. These results indicate that iodine and oxygen atoms exist as an IO_3^- molecular unit in a pseudo-perovskite-type structure.[31] The rotational motions of IO_3^- ions would be the most likely modes that are related to the structural instability (soft modes S_1 and S_2) of KIO_3 among all the twelve optical modes in the rhombohedral phase, which is consistent with the structural changes of from phase I to phase III of KIO_3 as discussed below.

The crystal structure of KIO_3 in phase I is shown in Fig. 6.5, according to the neutron powder diffraction result at 523K.[27] In this structure(R3, a=4.2973 Å, α =89.218^o, V=90.94 Å^3, Z=1), viewed along the [111] direction, the iodine atoms that overlap with the potassium atoms in the figure form an equilateral triangular network; and the I-O bonds rotate away from the reflection plane σ_v by a small angle θ (~ 3.1^o) along the three-fold rotation axis, thus the structure is with the symmetry of space group R3 rather than R3m (θ =0^o) . MEM/Rietveld analysis[28] from high-energy X-ray powder-diffraction data on KIO_3 at 530K indicates the similar crystal structure, but support the symmetry of R3m, *i.e.* θ =0^o.

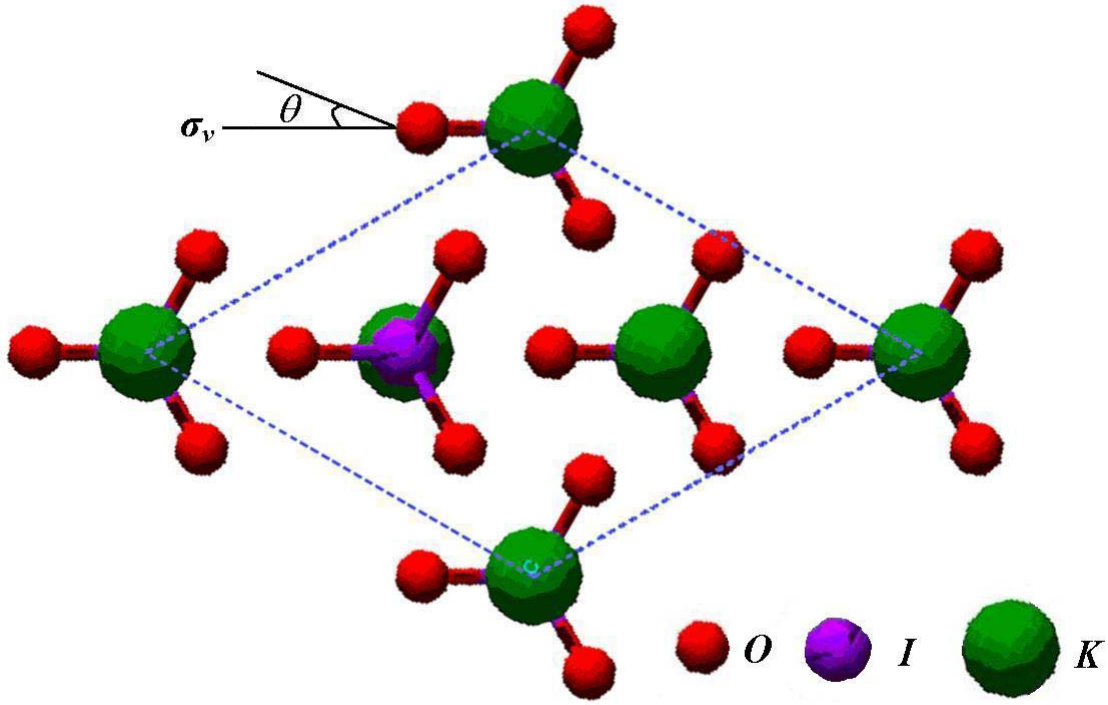

Figure 6.5 Schematic crystal structure of KIO_3 in phase I, viewed along the [111] direction.

To elucidate the inconsistent results between the neutron scattering[27] and the X-ray powder diffraction[28] on the symmetry of phase I, theoretical investigations on the phonon spectrum of KIO_3 were carried out using first principles method based on the DFPT and the LDA for the exchange and correlation interaction.[33,34] Optical phonon dispersion curves of KIO_3 at 530 K with the structural parameters provided by XRD[28] were calculated using the CASTEP code[34]. The norm-conserving pseudopotentials[37] was used in our calculation and the electron wave function was expanded using plane waves with a kinetic energy cutoff of 500 eV. In this calculation, the LO (longitudinal optical modes)-TO (transverse optical modes) phonon frequency splitting due to long-range electrostatic forces associated with lattice ionicity was included. Being infrared-active modes, the frequency of KIO_3 phonons

shift with the direction of the phonon wave vector *k* in the non-cubic crystal and lift the phonon branch degeneracy,[38] as shown in Fig.6.6, due to the accompanying long-range electric fields. To compare the calculated phonon frequencies of KIO_3 with experimental data, the Raman spectra of KIO_3 single crystals at 530K is shown in Fig.6.7.

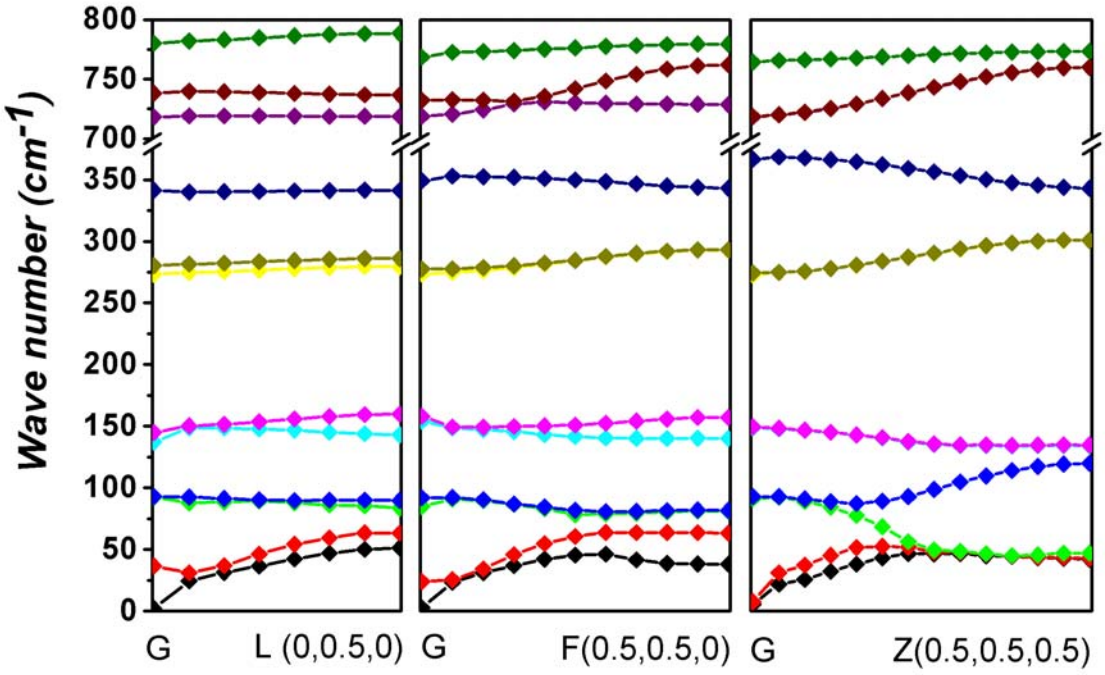

Figure 6.6 Calculated optical phonon dispersion curves of KIO_3 at 530 K with symmetry R3m (a=4.5137 Å, α =89.217°)[28]

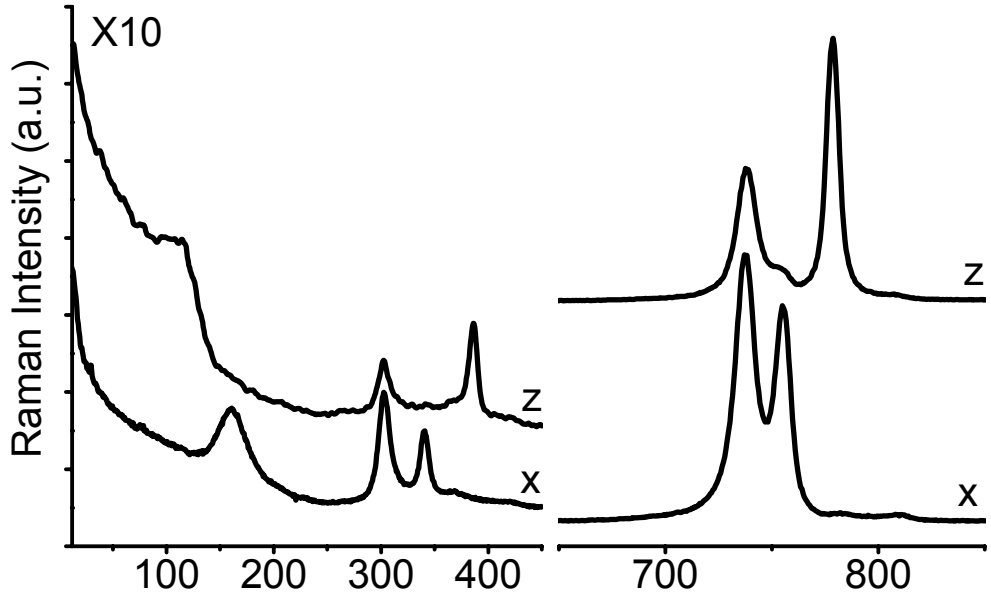

Figure 6.7 Raman spectra of KIO_3 single crystals at 530K.

The calculated phonon spectra are consistent with the R3m symmetry suggested by XRD[28], and the two lowest frequency phonons which approach zero at the gamma point could explain the appearance of a rather broad central Raman peak in phase I of KIO_3. However, as neutron scattering results[27] suggested the R3 symmetry for phase I, further simulations need to be carried out on this R3 structure. In fact, the R3 structure (a=4.4973 Å, α =89.218^o, I-O bond length= 1.775 Å) obtained by neutron scattering is quite similar to the R3m structure (a=4.5137 Å, α =89.217^o, I-$O_{\text{bond length}}$= 1.790 Å) determined by XRD, and the main difference is that in the former the I-O bonds rotate away from the reflection plane σ_v by ~ 3.1^o along the [111] direction. Considering the small difference between the two structures (Δa=0.0164 Å, $\Delta\alpha$ =0.001^o, I-$O_{\text{bond length}}$= 1.790 Å), it would be interesting to find out the physical origin of the two different structures. Therefore, using the LDA linear response approach again, we calculated further the phonon spectrum of KIO_3 in the rhombohedral phase I

using the structural parameters suggested by neutron scattering[27], but with symmetry R3m, that is we rotated the I-O bonds in the R3 structure back to the reflection plane σ_v. If R3 is indeed symmetry of the crystal structure, then we should expect at least one optical phonon mode with negative frequency at the gamma point. However, as shown in Fig.6.8, the low frequency optical phonons condense at the Brillouin zone normal point (near zone center), rather than zone center gamma point. That is the KIO_3 crystal structure in rhombohedral phase I observed by neutron scattering[27] should be an INC structure rather than a rhombohedral one with symmetry R3. Therefore the seemingly inconsistent descriptions of phase I of KIO_3 from neutron scattering[27] and XRD[28] can be understood easily, if we suggest a transient INC behavior appear near the phase transition I-II.

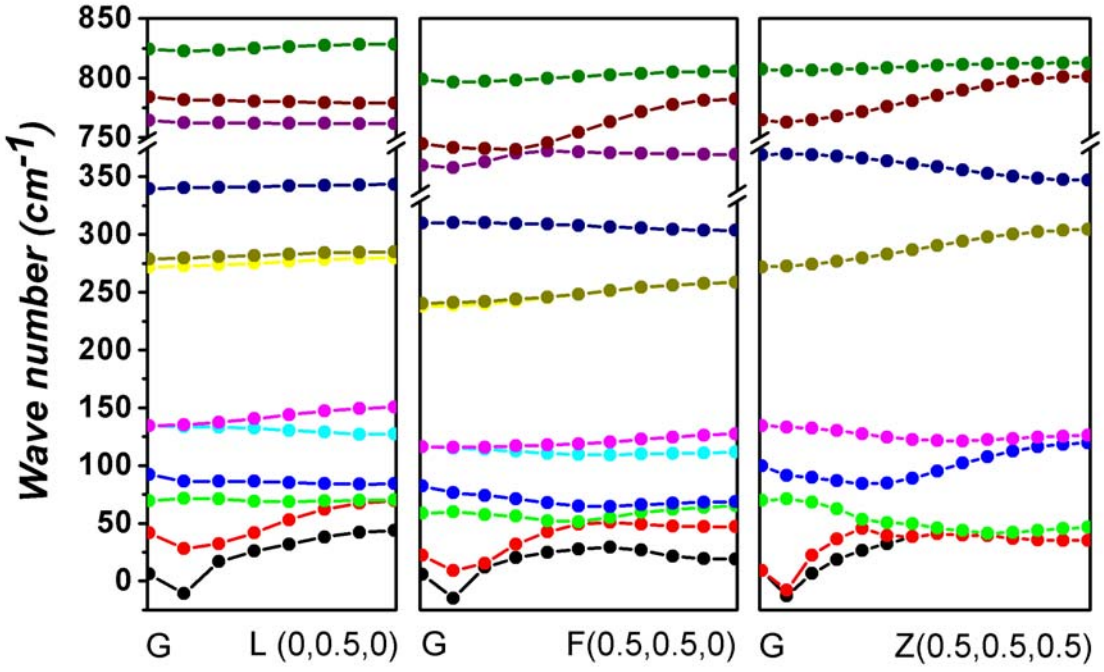

Figure 6.8 Calculated optical phonon dispersion curves of KIO_3 at at 523K with symmetry R3m (a=4.4973 Å, α =89.218°)[27]

Actually the existence of the INC structure is consistent with the neutron scattering observations of P. G. Byrom and B. W. Lucas[27]. In their work, using the profile-structure-refinement method, four structural modes (Z=1, with space groups $R\bar{3}m$, $R\bar{3}$, R3m, R3) were refined to the observed powder diffraction data. All the refinements in their analysis followed well behaved paths with the decreasing R-factor magnitudes to convergence, but the residual factors of R3m and R3 are quite similar (R_p = 15.91, 15.87; R_{wp} = 14.11, 13.96; R_I =7.82, 7.79; R_E =6.36, 6.36%), and considerably smaller than those based on $R\bar{3}m$ and $R\bar{3}$.[27] They indicated further that the distinction between the R3m and R3 models depended only on whether (for R3m) or not (for R3) $y(O) = x(O)$.[27] In fact the INC structure can induce $y(O) \neq x(O)$ too, while the symmetry is neither R3m nor R3. Moreover, with the existence of the transient INC phase behavior, the typical improper ferroelectrics feature of KIO_3, *i.e.* a very slight change of the dielectric constant near the transition point I-II observed by M. Maeda *et al*[29], can be understood too. M. Maeda *et al*[29] observed the real and imaginary parts of the dielectric constant $\varepsilon_{[100]}$ and $\varepsilon_{[111]}$ at 10 kHz, only a tiny anomaly was observed at $T_1 = 486K$ in the real part, but no obvious anomaly was detected in the imaginary part.[29] While in proper ferroelectric systems, the order parameter is the spontaneous polarization or the sublattice polarization and the dielectric anomalies are a direct consequence of the increased correlation in the order parameter fluctuations near T_c, in improper ferroelectric the order parameter is not proportional to polarization.[5,18] The characteristic features of improper ferroelectrics are a very slight change of the dielectric constant near the transition point and its unusual temperature dependence and also a low spontaneous polarization.[5,18] For the case of KIO_3 single crystals, the unstable phonons at the normal Brillouin zone point characterizing the transient INC phase will not induce the proper ferroelectric phase transitions whether

order-disorder or displacive categories, as both of which should be related phonon behaviors at Brillouin zone center. That could also explain why no soft mode has been observed by Raman techniques[24,30] in phase I of KIO_3.

Based on the discussion above, the phase transition I-II of KIO_3 should be of improper ferroelectric nature with the existence of a transient INC structure in phase I near the transition I-II. Actually, it is not unique for KIO_3 single crystals to have the INC phase near the phase transition point. The INC phase of quartz has been found near the α-β transition at T_c = 573 ^oC, which is also modulated by the soft mode condensation at the Brillouin zone normal point near center.[39]

6.5 Conclusions

The existence of the broad central peak which is dependent strongly on the polarization configuration in the rhombohedral phase I and the soft modes S_1 and S_2 with great damping near the phase transitions I-II and II-III of KIO_3 is observed by Raman technique. Furthermore, based on the calculated phonon dispersion curves, we suggested a transient INC phase which exists in phase I of KIO_3 near the phase transition. With the appearance of INC phase in phase I, the improper ferroelectric characteristics of phase transition I-II of KIO_3 observed by the dielectric constant investigations can be understood easily. Consequently the seemingly inconsistent descriptions by neutron scattering[27] and XRD[28] can be also understood based on the INC behavior in phase I.

References

1 F. Jona, in *Ferroelectric Crystals*, (Pergamon Press, Oxford, New York, 1962), p. 10.

2 V. Vargha, A. Gy. Pozsgay, and P. Valentini, Periodica Polytechnica Ser. Chem. Eng. **43**, 17(1999).

3 W. Kanzig, in *Ferroelectrics and antiferroelectrics*, (Academic Press, New York, 1957), p. 5.

4 J. Grindlay, in *An introduction to the phenomenological theory of ferroelectricity*, (Pergamon Press, Oxford, New York, 1970), p.1.

5 B. A. Strukov and A. P. Levanyuk, in *Ferroelectric Phenomena in Crystals*, (Springer: Berlin, 1998), p.9, p.17, p.74.

6 C. Kittel, *Introduction to Solid State Physics*. 374 (Sixth Edition, John Wiley & Sons, Inc., Singapore, 1986).

7 W. Cochran, Adv. Phys. **9**, 387(1960); **10**, 401 (1961); **18**, 157(1969); Phys. Rev. Lett. **3**, 412(1959).

8 T. P. Dougherty, G. P. Wiederrecht, K. A. Nelson, M. H. Garrett, H. P. Jensen, and C. Warde, Science **258**, 770(1992).

9 N. Sicron, B. Ravel, Y. Yacoby, E. A. Stern, F. Dogan, and J. J. Rehr, Phys. Rev. B **50**, 13 168(1994).

10 A. Scalabrin, S. P. S. Porto, H. Vargas, C. A. S. Lima and L. C. M. Miranda, Solid State Commun. **24**, 291 (1977).

11 J. P. Sokoloff, L. L. Chase, and D. Rytz, Phys. Rev. B **38**, 597(1988).

12 M. D. Fontana, A. Ridah, G. E. Kugel and C. Carabatos-Nedelec, J. Phys. C: Solid State Phys. **21**, 5853(1988).

13 M. D. Fontana. H. Idrissi, G.E. Kugel, and K.Wojcik, J. Phys.: Condens. Matter **3**, 8695(1991).

14 M. Stachiotti, A. Dobry, R. Migoni, and A. Bussmann-Holder, Phys. Rev. B **47**, 2473(1993).

15 W. Zhong, D. Vandebilt and K. M. Rabe, Phys. Rev. B **52**, 6301(1995).

16 M. Sepliarsky, M. G. Stachiotti, and R. L. Migoni, Phys. Rev. B **56**, 566(1997).

17 Y. Girshberg and Y. Yacoby, J. Phys: condens. Matter **11**, 9807(1999).

18 R. Blinc and B. ŽEKŽ, in *Soft Modes in Ferroelectrics and Antiferroelectrics*, (North-Holland Pub. Co., Amsterdam, 1974). p.15, p.45.

19 F. Herlach, Helv.Phys.Acta. **34**, 305(1961).

20 I. NÁRAY-SZABÓ, and A.KÁLMÁN, Acta Cryst. **14**, 791(1961).

21 A. A. Filimonov, L. G. Lomova, V. S. Suvorov, V. I. Pakhomov, and A. S. Sonin, Sov. Phys. Cryst. **10**, 202(1965).

22 J. G. Bergman, Jr., G. D. Boyd, A. Ashikin and S. K. Kurtz, J. Appl. Phys. 40, 2860(1969).

23 X. Yin and M. K. Lü, Appl. Phys. Lett. **60**, 2849(1992).

24 E.Sajie, Z. Kristallogr. **317**, 139(1974).

25 B. W. Lucas, Acta Cryst. **C40**, 1989(1984).

26 B. W. Lucas, Acta Cryst. **C41**, 1388(1985).

27 P. G. Byrom and B. W. Lucas, Acta Cryst. **C43**, 1649(1987).

28 H. Kasatani, S. Aoyagi, Y. Kuroiwa, K. Yagi, R. Katayama, H. Terauchi, Nucl Instrum Meth B **199**, 49(2003).

29 M. Maeda, M. Takagi, and I. Suzuki, J. Phys. Soc. Jpn. **69**, 267(2000).

30 M. Ahart, S. Kojima, M. Takagi, M. Maeda and I. Suzuki, Jpn. J. Appl. Phys. **37**, 5687(1998).

31 K. Yagi, S. Umezawa, H. Teraychi and H. Kasatani, J. Synchrotron Rad: **8**, 803(2001).

32 N. Sai, and D. Vanderbilt, Phys. Rev. B **62**, 13942(2000).

33 S. Baroni, S. de Gironcoli, A. dal Corso and P.Giannozzi, Rev. Mod. Phys. 73, 515(2001).

34 M. D. Segall, P. L. D. Lindan, M. J. Probert, C. J. Pickard, P. J. Hasnip, S. J. Clark, and M. C. Payne, J. Phys.: Condens. Matt. 14, 2717(2002).

35 M. K. Lü, and K. C. Zhang, Sci. Sinica, A 30, 45(1987).

36 K. Nakamoto, in *Infrared and Raman Spectra of Inorganic and Coordination Compounds*, (Fifth Edition, John Wiley & Sons, Inc., New York, 1997), p.173.

37 D. R. Hamann, M. Schluter, and C. Chiang, Phys. Rev. Lett. 43, 1494 (1979).

38 R. Loudon, Advances in Physics. **14**, 425(1964).

39 K. Abe, K. Kawasaki, T. Koikei and T. Shigenari, J. Phys.: Condens. Matt. 1, 8741(1989).